2015-04-30

X-ray Emission from the Local Hot Bubble and Solar Wind Charge Exchange

Youaraj Uprety
University of Miami, ubaraj@gmail.com

UNIVERSITY OF MIAMI

X-RAY EMISSION FROM THE LOCAL HOT BUBBLE AND SOLAR WIND CHARGE EXCHANGE

By

Youaraj Uprety

A DISSERTATION

Submitted to the Faculty
of the University of Miami
in partial fulfillment of the requirements for
the degree of Doctor of Philosophy

Coral Gables, Florida

May 2015

UNIVERSITY OF MIAMI

A dissertation submitted in partial fulfillment of
the requirements for the degree of
Doctor of Philosophy

X-RAY EMISSION FROM THE LOCAL HOT BUBBLE AND SOLAR WIND CHARGE EXCHANGE

Youaraj Uprety

Approved:

_____
Massimiliano Galeazzi, Ph.D.
Professor of Physics

_____
Joshua Gundersen, Ph.D.
Professor of Physics

_____
Manuel Huerta, Ph.D.
Professor of Physics

_____
M. Brian Blake, Ph.D.
Dean of the Graduate School

_____
Frederick S. Porter, Ph.D.
Scientist
NASA/GSFC
Greenbelt, Maryland

UPRETY, YOUARAJ (Ph.D., Physics)
X-ray Emission from the Local Hot Bubble and Solar Wind Charge Exchange (May 2015)

Abstract of a dissertation at the University of Miami.

Dissertation supervised by Professor Massimiliano Galeazzi
No. of pages in text. (148)

DXL (Diffuse X-rays from the Local galaxy) is a sounding rocket mission to quantify the Solar Wind Charge Exchange (SWCX) X-ray emission in the interplanetary medium, and separate its contribution from the Local Hot Bubble (LHB) emission. The first launch of DXL took place in December 2012. This thesis will describe the DXL instrumentation and calibrations, and discuss the results obtained. The mission uses two large area proportional counters to scan through the Helium Focusing Cone (HFC), a high helium density region in the solar system emitting excess X-rays due to SWCX. Using well determined models of the interplanetary neutral distribution and comparing the DXL results with data from the same region obtained by the ROSAT satellite away from the cone, we calculated that SWCX contributes at most 36% to the ¼ keV ROSAT band and 13% to the ¾ keV ROSAT band, in the galactic plane. This provides a firm proof for existence of a LHB which dominates the Diffuse X-ray Background (DXB) at ¼ keV, while raising new questions on the origin of the ¾ keV emission.

Dedicated to

My grandfather, Late Achutananda Thapaliya,

My father Bilashi Ram Upreti,

My mother Nilam Upreti,

My sister Reeta Upreti,

and

My wife Anija.

ACKNOWLEDGEMENTS

Dr. Massimilano Galeazzi, thank you for being the best advisor one can ask for. I will always be in your debt.

My committee members Dr. Scott Porter, Dr. Joshua Gunderson and Dr. Manuel Huerta, thank you.

Nick, we traveled over seven thousand miles hauling DXL/UXT around. We could have almost been to the other side of the Earth if we had taken our journey through the center of the Earth! Thanks for being a phenomenal friend, both during the road trips and other times.

Narayan, we were so unsure about the whole Ph.D. thing when we started. How does it feel now? Thanks for being a great colleague and a friend.

My parents, relatives and friends, you all made me who I am. Thank you for supporting me through all of these years!

Anija, you are my sunshine. I couldn't have done this without you.

Although this is not a complete list, here are few other people who helped me through this incredible journey: Dr. Dan McCammon, Dr. Dmitra Koutroumpa, Dr. Kip Kuntz, Dr. Steve Snowden, Dr. Eugenio Ursino, Dr. Wenhao Liu, Dr. Krishna Prasai, Judy Mallery, Anella Sebro, Juan Lopez, Manuel Collazo, Marco Monti and everyone at NASA/WFF.

TABLE OF CONTENTS

LIST OF FIGURES

LIST OF TABLES

CHAPTER 1 **INTRODUCTION**

1.1 Synopsis

X-ray radiation is produced in many astrophysical systems by a variety of physical processes, and arrives at our detectors with all or part of its original intensity. The astronomical X-ray radiation that comes from all directions is called the Diffuse X-ray Background (DXB). When the energy of the X-rays are below ~1 keV, we use the term Soft X-ray Background (SXRB). The study of the DXB began in 1962 when Riccardo Giacconi and his team at American Science and Engineering, Inc. (AS&E) observed it for the first time [1]. Decoding the nature and origins of the DXB has advanced considerably since its discovery [1]–[8]. Extensive observations of the DXB were carried out during targeted sounding rocket experiments [2], [9], [10], the Wisconsin All-Sky Survey (WASS) [11], Small Astronomy Satellite (SAS-3) observation program [12], High Energy Astronomy Observatory (HEAO-1 A2) program [13] and ROSAT All-Sky Survey (RASS) [7] satellite mission. These observations have provided us with a wealth of information on the nature of the diffuse X-ray radiation.

The advances in our knowledge of background radiation is closely associated with the development of X-ray detectors. While proportional counters were the work-horses of X-ray astronomy, the knowledge of the spectral information of the diffuse X-ray background was limited owing to their low resolution [14]. Since partially ionized metal lines dominate the soft X-ray radiation from hot gas (10^6-10^7 K), spectral resolution of the emission and

absorption lines can provide information about the physical state of the emission gas. High resolution spectroscopy development advanced significantly with the launch of XMM-Newton[1], Chandra[2] and Suzaku[3] X-ray observatories [15], [16]. Micro-calorimeters provide the highest resolution spectra and are being developed and tested for use in sounding rockets and satellites, with resolution of ~9 eV between 60-1000 eV already achieved [17]. Due to the fact that most historical X-ray observations were carried out using available low resolution proportional counter detectors, the diffuse emission is generally studied in energy bands. Notable among these energy bands are the B, C and M bands of WASS, and the R12 (also known as ¼ keV) and the R45 (also known as ¾ keV) bands of ROSAT mission [7]. We will mention the ¼ keV and ¾ keV bands throughout the text, so it must be noted that X-rays with approximate mean energies of 250 eV and 750 eV respectively are included in each band (see section 1.3 for precise definition of these bands).

A culmination of theoretical and experimental advances led to a general consensus by the early 1990s that the X-rays in the ¼ and ¾ keV bands originated in one or more of the following sources: i) a ~100 parsec (pc) scale million-degree interstellar plasma of the Local Hot Bubble (LHB), ii) 1.5-3$\times 10^6$ K plasma of the Galactic Halo (GH), and iii)

---

[1] http://xmm.esac.esa.int/
[2] http://chandra.harvard.edu/about/
[3] http://darts.jaxa.jp/astro/suzaku/

resolved and unresolved extragalactic sources [3], [4], [6], [9], [18]–[20]. Most of the emission above 1 keV was attributed to the resolved and unresolved extragalactic point sources fitting a power law model [21]. Most of the emission observed in the galactic plane in the ¼ keV band was considered to come from the LHB, with little contribution from the more distant sources at higher galactic latitudes. In the fairly isotropic ¾ keV band, most of the emission was attributed to the hot gas of the galactic disk and halo. However, none of these explanations were without caveats primarily because the emission a) changes with observational geometry, b) has little agreement with theoretical predictions, and c) has some incompatibilities with the observations in other wavelengths [6], [19], [22]–[24].

In the late 1990s, yet another source of the DXB was discovered. The ions of the solar wind interacted with the neutrals of the geocorona and the heliosphere to produce X-rays within our solar system in a process called Solar Wind Charge Exchange (SWCX) emission [8], [25], [26]. Discovery of SWCX as a significant contributor to the diffuse X-ray background was expected to resolve some of the discrepancies between the theoretical and the observational peculiarities of the diffuse emission [8], [25]–[30]. However an accurate estimation of SWCX has been hindered despite numerous efforts [27], [29]–[34] due to the variable nature of the SWCX emission due to solar activity, the poorly understood interaction cross sections of the charge exchange species, and the spectral similarity to thermal emission background. Calculations showed that the SWCX could generate anywhere from 25% to all of the ¼ keV and the ¾ keV band emission [27], [35]–[37]. An

accurate estimation of SWCX in both bands is required to improve our understanding of the interstellar medium and the X-ray emitting plasma of the LHB and the GH. Resolving the SWCX contributions to the DXB therefore became an important endeavor.

The DXL (Diffuse X-ray emission from the Local Galaxy) mission [38] was conceived at NASA/GSFC and the University of Miami to quantify the SWCX emission separately in the ¼ and ¾ keV bands. DXL is a sounding rocket mission to make empirical measurements of the SWCX [38], [39] in a high charge exchange region within the solar system. This thesis describes the instruments, the calibrations and the results of the DXL mission, which launched successfully in December 2012.

1.2 Soft X-Ray Background

Riccardo Giacconi and his team at AS&E wanted to check whether there was any fluorescent X-rays from the moon due to solar X-rays striking the lunar surface, and to see if there were any other X-ray sources out there in the sky. Three un-collimated Geiger counters were launched to an altitude of 225 km, but only two of them worked as expected.

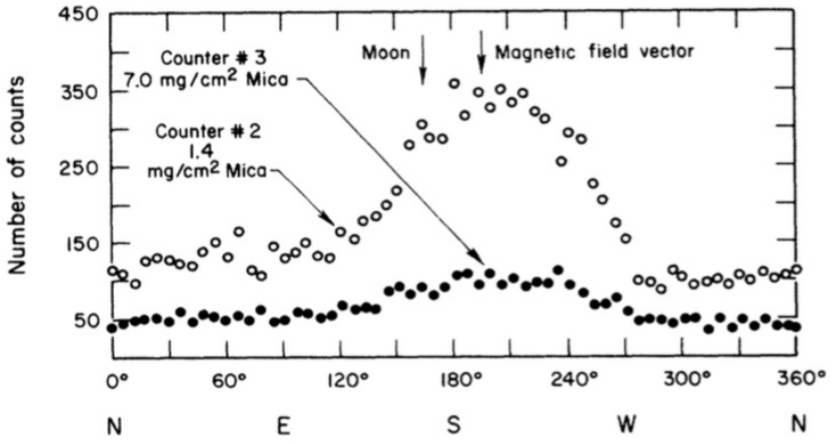

Figure 1.1: First detection of non-zero flux in all directions, suggesting the presence of a diffuse X-ray background [1]

The X-ray flux (~1.5-6 keV) measured by the two counters, plotted against the Galactic longitude is shown in Figure 1.1. There is a peak around 180^0, however the counts do not go to zero on either side of the peak, prompting the team to argue that the peak must be embedded in a "diffuse background radiation" [1]. Subsequent investigations noted that the substantial flux above 1 keV was in the form of a isotropic background, possibly from extragalactic sources [9], [40], [41]. After the development of detectors capable of studying X-rays below 1 keV, SXRB emission was first observed in 1966 [2]. The emission showed anisotropy, with a general galactic plane to pole variation, and an apparent anti-correlation with the X-ray absorbing neutral hydrogen [2], [42], [43]. The emission was attrubuted to absorbed extragalactic sources and partly to some anomalous origin located within the galaxy [2], [10], [44]. The observed soft X-ray flux below 1 keV exceeded the extrapolation from the higher energy emission, requiring a source much closer within the

galaxy [6], [10], [42], [43], [45], [46]. The use of C edge filters allowed a separation of X-ray background below 1 keV into two separate bands. I will divide further discussion of diffuse X-ray emission into ¼ keV and ¾ keV bands for convenience.

The observation of ¼ keV X-rays in the direction of the galactic plane, where they are easily absorbed by the thick neutral material in the galactic disk, indicated a local source of emission. The presence of a local source of thermal X-rays suggests the existence of a hot gas within 30 to 200 parsecs around the Sun that displaced the neutral material [4], [47]. It was predicted that most or all of the flux measured in the ¼ keV band was produced by a thermal emission from a million-degree plasma [4], [6], distributed within the local HI cavity surrounding the Sun [4], [48]–[50]. The eventual detection of thermal emission lines [51], [52] helped strengthen the idea of X-ray emission from thermal plasma [3]–[5], [11], [48], [53]–[55].

Initial observations concluded that the general anti-correlation with the neutral hydrogen column in the ¼ keV band was due to absorption of the flux by the neutral material between the source and the observer in the "absorption" model. However, the apparent absorption was much less than expected, with a weak energy dependence and a general lack of expected detailed negative correlation with the neutral material [56]. A "displacement" model was then proposed which claimed that an irregularly shaped hot plasma was responsible for all or most of the emission in the ¼ keV band [4], [47]. The model postulates that a bulk of the observed ¼ keV flux originates from a million degree

thermal plasma contained within the local HI cavity, but not completely filling it. Stellar winds and supernovae events can create cavities in the interstellar medium, typically ~100 pc across with low neutral gas densities (~0.01cm^{-3}), one of which encloses our Sun [24], [57]. The cavity is extended more towards the galactic pole (resulting in more emission) and less so towards the plane (resulting in less emission), thereby producing the negative correlation with the neutral material [56]. The displacement model also provided a more robust explanation for the weakness and energy independence of the apparent absorption [56]. Detection of the OVI absorption line towards OB stars within the solar neighborhood by *Copernicus* satellite [51] and the emission lines from OVII and OVIII [52] by a sounding rocket experiment provided strong experimental evidence for the existence of thermal plasma in the local cavity [6]. The million degree plasma which filled the local HI cavity [58], [59] partially and irregularly, was called the LHB.

LHB was found to have a temperature of $10^{6.1}$ K and intensity that varies by a factor of ~3.3 over large angles using a two component model (foreground plus absorbed halo emission) plus a fixed absorbed extragalactic contribution [56]. Snowden [56] calculated the distance scales of LHB, and found it to extend between ~40 pc to ~130 pc depending on the direction. The ROSAT map [23] of the LHB is shown in Figure 1.2. The bar indicates the intensity of X-rays in ROSAT Units (RU = 10^{-6} counts s^{-1} armin^{-2}).

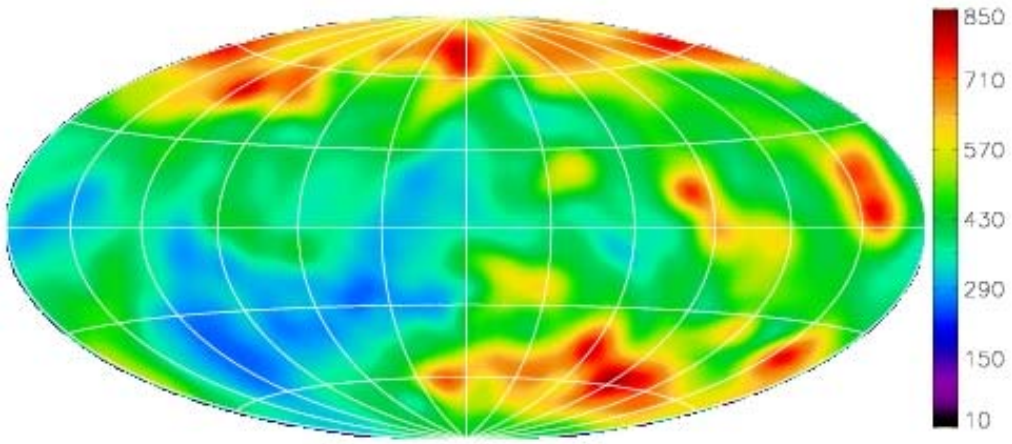

Figure 1.2: Local Hot Bubble map in Aitoff-Hammer projection showing X-ray intensity in RU, indicated by the colorscale on the right-hand side [60]

Despite some success, the idea of the LHB had some serious problems. The Diffuse X-ray Spectrometer (DXS) shuttle mission measured emission lines with Bragg-crystal spectrometers with a resolution of 4 eV at 148 eV and 14 eV at 284 eV and observed thermal emission lines, but no collisional ionization equilibrium model (with cosmic abundance or depleted) at any temperature in the 10^5-10^7 range could reproduce the spectra [14], [61]. The initial assumption that all of the soft X-ray came from this bubble had to be revised when it was observed that over 50% of the ¼ keV emission came from beyond the Draco cloud [19], requiring a source beyond the bubble. The size and shape of the LHB derived from the soft X-ray observations did not match the contours of the local cavity derived from the NaI mapping method [24], [62]. Also, the calculated plasma thermal pressure of the LHB was much larger than that of the Local Interstellar Clouds (LIC), creating a pressure imbalance problem [24], [63].

In the 0.5 - 2 keV energy band, the observed emission is a mixture of galactic and extragalactic emission [23]. Generally the isotropic background of this band also contains bright structures due to the emission from old Supernova Remnants (SNRs) and superbubbles [6]. The ¾ keV emission showed a lack of variation in the intensity going across the galactic plane despite the presence of neutral material thick enough to absorb the extragalactic or halo source in the plane, suggesting a galactic emission to compensate for the absorption [6], [23]. Shadow observations and analyses of ROSAT data suggested the origin of the X-ray background from local and non-local plasma components [64]–[66]. The non-local plasma of the halo is considered hotter and more extended than the LHB, with a temperature of 2.22×10^6 K [34], [67]. Most of the emission in this band comes from the 1.5 to 3×10^6 K gas in the disk and halo, with a significant stellar emission towards the galactic center and the plane [33].

Shadow observations are crucial in the ¾ keV band to decipher the origins of the emission. Multiple pointed observations using *XMM-Newton*, *Chandra* and *Suzaku* observatories have added a wealth of information [32], [34], [65], [66], [68], [69], particularly to resolve the emission lines of OVII (0.56 keV) and OVIII (0.65 keV) that are the most important lines in the ¾ keV band [17], [36]. These lines are used to diagnose temperature and density of the thermal plasma. The presence of OVII and other emission lines provided evidence for $1 - 4\times10^6$ K thermal gas [6]. Smith et al. [65] calculate the halo contribution with an upper limit of OVII and OVIII intensities at 2.34±0.33 photons $cm^{-2}s^{-}$

$^{1}sr^{-1}$ (or line units, LU) and 0.77±0.16 LU. They also find 3.5 LU and <0.34 LU of OVII and OVIII in front of the shadows, attributable to the LHB (and SWCX). Galeazzi et al. [66] find 2.63±0.78 LU and 0.03±0.43 LU of OVII and OVIII in front of the shadows respectively, again attributable to the LHB and the SWCX. X-ray Quantum Calorimeter (XQC) group showed that the oxygen lines account for the majority of the diffuse background in the ROSAT R4 band [17]. The contribution from the SWCX emission (see section 1.4) added another level of complexity to the ¾ keV emission.

1.3 ROSAT All-Sky Survey (RASS)

A joint effort of Germany, the US and the UK to map the entire sky in X-rays resulted in the Roentgen Satellite (ROSAT) mission. Launched via a Delta II rocket in 1990, ROSAT was placed in a low Earth orbit at 580 km altitude. By 1999, ROSAT had collected a significant amount of data identifying over 100,000 X-ray sources, discovering un-expected sources of X-rays, detecting isolated neutron stars and resulting in over 8,500 publications. The primary objective of the mission was to perform the first all sky survey with an imaging X-ray telescope with a sensitivity several orders of magnitude higher than previous surveys [70]. ROSAT carried an X-ray Telescope (XRT) with two position sensitive proportional counters (PSPC), one High Resolution Imager (HRI) detector, and a Wide Field Camera (WFC) Extreme Ultra-Violet (EUV) telescope as the focal plane instruments [71].

The ROSAT survey was designed to observe discrete sources in the 0.1 - 2.4 keV range, however the relatively large effective area and short focal length of the XRT coupled with low-background PSPC detector resulted in an instrument ideal for studies of diffuse X-ray background. Since proportional counters have poor energy resolution, elemental K-edge filters are incorporated into the detector windows to increase the energy discrimination [7]. For example, the University of Wisconsin-Madison (UW) group mapped the X-ray sky in 130 eV to 6300 eV interval with proportional counters in a series of sounding rocket flights. The UW group divided the lowest energies into B and C bands, for Boron and Carbon filters [11]. To take full advantage of ROSAT PSPC energy resolution, and to approximately match band selections with previous sky surveys, ROSAT PSPC pulse height was divided into various bands for analysis, as defined in Table 1.1. Note that R1 and R2 bands have the same upper limits due to the carbon K_α absorption edge of the window material [7].

ROSAT Energy Band Definitions

Band Name	PI Channels	Energy (keV)
R1	8-19	0.11-0.284
R1L	11-19	0.11-0.284
R2	20-41	0.14-0.284
R3	42-51	0.20-0.83
R4	52-69	0.44-1.01
R5	70-90	0.56-1.21
R6	91-131	0.73-1.56
R7	132-201	1.05-2.02

Table 1.1: ROSAT band definitions [72]

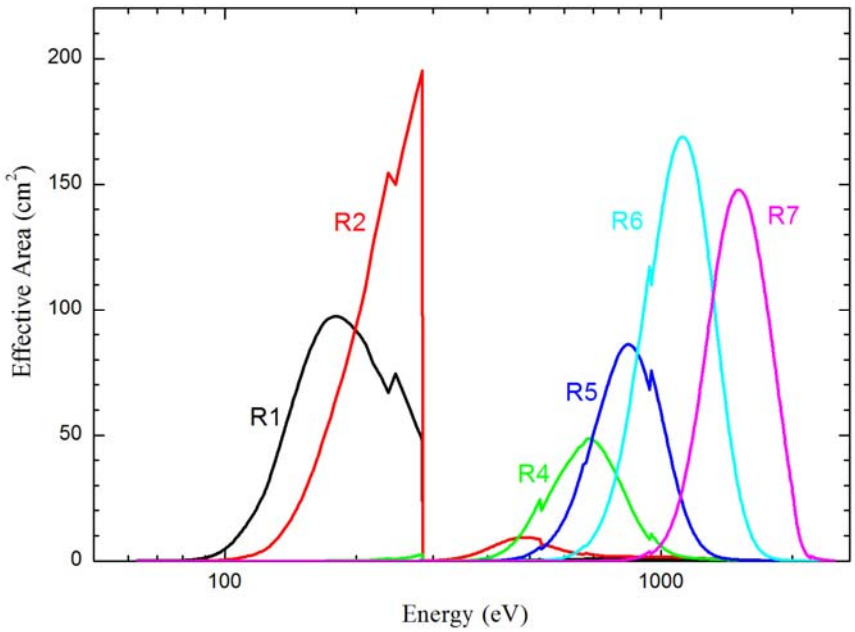

Figure 1.3: ROSAT effective area for the bands R1 through R7. R3 has little useful information, so it is ignored.

The response curves for the bands defined in Table 1.1 are shown in Figure 1.3. Note that the combined R1 and R2 band is the "1/4 keV (R12) Band," R4+R5 is the "3/4 keV (R45) band," and R6+R7 is the "1.5 keV (R67) band." Three extraordinary maps of the diffuse X-ray sky were generated in these bands that showed us in great detail the nature of the diffuse X-ray emission [23]. ROSAT ¼ keV band (also known as R12) includes X-rays in the 0.1 keV to 0.3 keV interval (see Table 1.1). The X-ray map from the R12 band shows higher flux towards the galactic poles and a relatively smooth galactic plane emission (Figure 1.4). The colorscale on the right indicates the intensity of X-rays in RU [23].

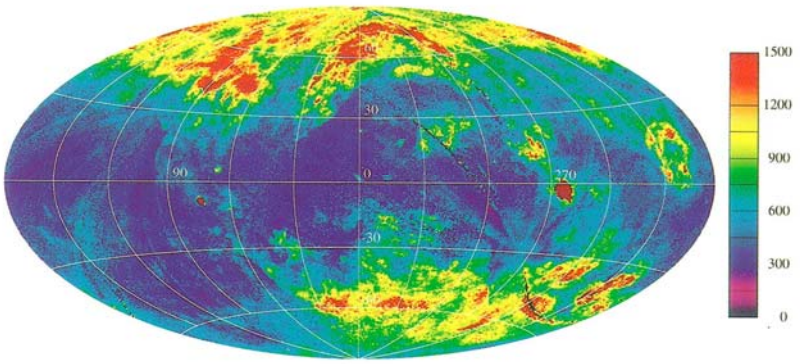

Figure 1.4: ROSAT R12 map on the Aitoff-Hammer projection with colorscale on the right side indicating the intensity in RU [23]

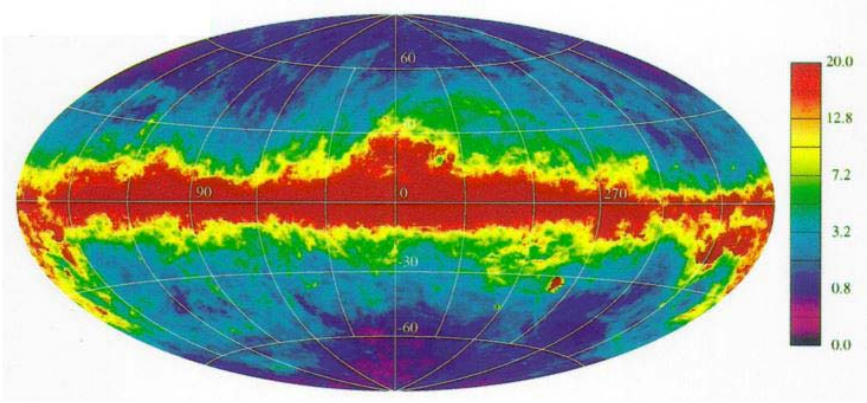

Figure 1.5: Map of the column density of neutral Hydrogen in units of MJy sr^{-1} [23]

The most obvious feature of the map is a general anti-correlation with the neutral hydrogen density map (Figure 1.5). The anti-correlation is largely explained by the "displacement" model [4] and the LHB discussed earlier. The plane of the galaxy is mostly dominated by unabsorbed LHB emission. At higher latitudes however, observation of GH and extragalactic emissions is permitted by the low HI column density [7]. Before the

discovery of the SWCX, the general agreement was that majority of the flux in ¼ keV came from LHB, and the rest from the highly variable GH [23].

On the other hand, the map of R45 Band (3/4 keV) is generally isotropic with a few distinct features (Figure 1.6). The sidebar in the figure indicates the intensity of X-rays in ROSAT Unit (RU) [23]. The map shows the Galactic bulge with a temperature of log T = 6.6 K dominating the galactic center and the Loop I region [23], [64]. Bright galactic features are apparent, for example Loop I, Cygnus Loop and Vela/Puppis NR towards the center, extending above and below. The diffuse emission in this band is from the GH, stellar emission and the extragalactic components [23], [33], with contamination from the SWCX emission.

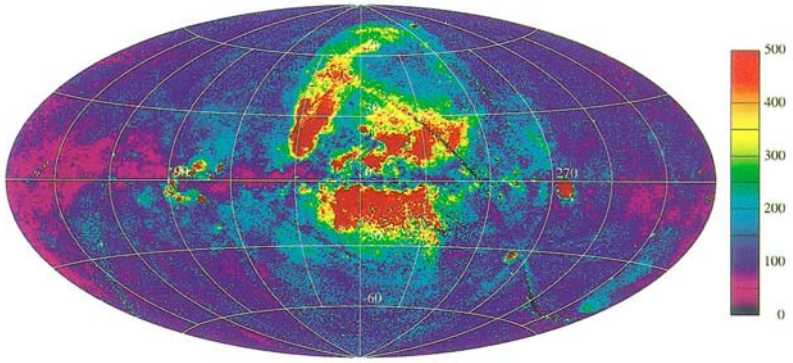

Figure 1.6: ROSAT R45 map on the Aitoff-Hammer projection, with colorscale on the right side indicating the intensity in RU [23]

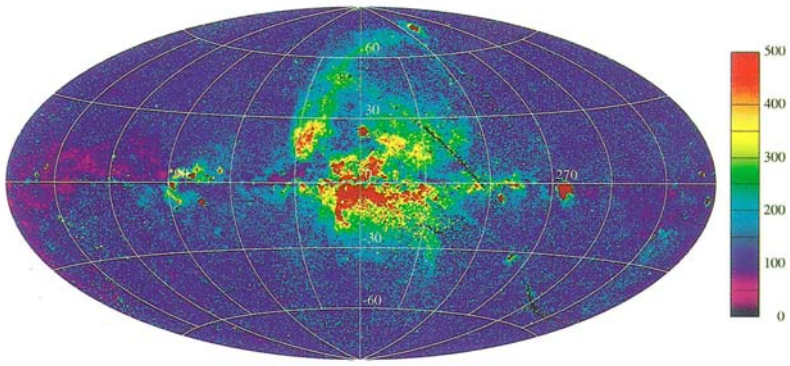

Figure 1.7: ROSAT R67 map on the Aitoff-Hammer projection, with color bar on the right side indicating the intensity in RU [23]

The R67 band (1 keV to 2 keV energy interval) map shows similar isotropic emission with superimposed structures (Figure 1.7). Some of the discrete features in the R45 and R67 maps are shown in Figure 1.8. Few Active Galactic Nuclei (AGN) and galaxy cluster distributions can be seen in the high galactic latitudes, with a scatter of discrete sources towards the plane. The Cygnus Super-bubble, the North Polar Spur, the Loop I, and the Eridanus enhancements are visible in the maps.

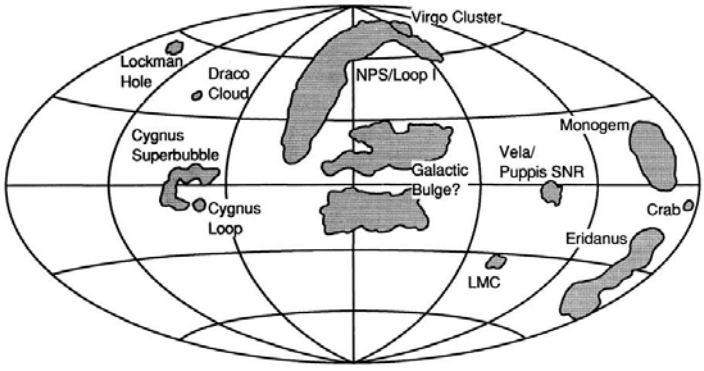

Figure 1.8: Discrete sources identified in the R45 and R67 maps [7]

ROSAT added a wealth of information to the understanding of the SXRB. However, the view of the SXRB was further complicated by discovery of a new source of diffuse X-rays in 1996. Using ROSAT data, comets were discovered to emit X-rays via charge exchange process with the solar wind [25], [26], in a process called the Solar Wind Charge Exchange (SWCX). It was also suggested that the solar wind interacted with the neutrals of the interplanetary medium and the geocorona to produce X-rays [8]. The discovery of SWCX as yet another component of the SXRB required a re-evaluation on the origins of the diffuse X-ray background.

1.4 Solar Wind Charge Exchange (SWCX)

The Sun's corona is an active million-degree plasma that streams charged particles into the interstellar medium (ISM) as "solar wind". Ions like $O^{7+,}$ O^{6+}, C^{6+}, N^{6+}, Ne^{8+}, Si^{9+}, and Fe^{12+} exist in the solar wind. The ISM, mostly neutral hydrogen and helium, flows at about $25 kms^{-1}$ through our solar system due to the motion of the Sun through a small interstellar cloud [39]. The solar wind ions readily interact with neutrals of the ISM in a charge exchange process emitting low energy X-rays and EUV radiation [73], [74].

In the charge exchange (CX) process, ions temporarily gain an excited state as they take away one or more electrons from neutral atoms or molecules, but relax subsequently by emitting photons. When a fast moving "projectile" ion approaches a neutral "target" (or donor), an electron from the neutral atom or molecule may be transferred to the ion. The electron is captured into an excited state of the ion in a high energy level *n*. In a subsequent

relaxation of the ion, a photon is emitted [73]. The energy of the emitted photon depends on the initial charge state of the ion. The net reaction of SWCX is a two-step process:

$$A^{q+} + B \rightarrow A^{(q-1)+^*} + B^{+} \quad 1.1$$

$$A^{(q-1)+^*} \rightarrow A^{(q-1)+} + h\nu \quad 1.2$$

where A is an ion with charge q, that captures an electron from an initially neutral target B. The excited state (denoted by a *) ion subsequently decays to the ground state by the emission of one or more photons [75]. For a review of charge exchange physics and its prevalence in the astrophysical context, and the laboratory studies of the process, please refer to [76]–[79] and references therein.

The intensity of SWCX photons depends on a variety of factors such as relative velocities and densities of the target and the projectiles, and the interaction cross-sections [74], [76], [79]. To calculate the count rate due to SWCX, the line of sight integral of the product of ion flux, the neutral densities, the summed product of partial cross sections for producing charge exchange, and the efficiency are taken for neutral H and He:

$$Rate = \int \sum_i \sum_j n_i n_{He} v_{rel} \sigma_i b_{ij} g_j \, ds + \int \sum_i \sum_j n_i n_H v_{rel} \sigma_i b_{ij} g_j \, ds \quad 1.3$$

where *i* and j are the solar wind species and the emission lines for the species respectively, σ_i are the speed-dependent interaction cross sections for individual species, b_{ij} is the line branching ratio, g_j is the instrument's response to line *j*, and v_{rel} is the relative speed between solar wind and neutral flow [39].

After the discovery of SWCX process in comets [25], [26] , it was suggested that the solar wind could charge exchange with interplanetary medium or the geocorona to produce soft X-rays right here in the solar system [8]. Observation of the Hubble Deep Field-North using XMM-Newton data clearly demonstrated the SWCX emission and its time variable contribution superimposed on the diffuse X-ray background [80]. Excess OVII and OVIII emission detected by *Chandra* in front of the dark moon clearly demonstrates geocoronal SWCX emission [80], [81]. Long Term Enhancements [72] observed with ROSAT were also found to correlate with the SWCX emission [28], [82]. Observation of SWCX emission from the Earth's magnetosheath [83] and in the spectra of the XMM-Newton [32] reinforced the significance of charge exchange emission in the geocorona and the heliosphere. Evidence of SWCX emission led to the next natural question regarding the amount of SWCX contribution to the diffuse X-ray background maintained up to the time.

1.5 Motivation

The diffuse X-ray background, a superposition of LHB, GH and the extragalactic emission, had to be reviewed in the new light after the identification of SWCX emission. LHB came about to make the best sense out of what was observed in the UW B and C

bands, and the ROSAT ¼ keV band. Plagued by a lack of proper models to fit the spectra observed by DXS [61] and the pressure imbalance problems with LICs [63], LHB needed a re-evaluation. The identification of SWCX was expected to resolve some of these inconsistencies [84]. However, the characteristic line emission of the SWCX is not easily distinguishable from the plasma emission of the background [38] and the time variation of the SWCX emission is difficult to tackle [33]. The complexity of charge exchange physics, poorly understood interaction cross-sections of the charge exchange species, and a lack of accurate solar wind compositions have hindered an accurate estimation and modeling of the SWCX despite numerous efforts [27], [29]–[34].

An early estimate from a simple model puts the SWCX contribution at 25% - 50% in the soft emission regime [27], [85]. An improved model credits SWCX with roughly 50% of the emission in the galactic plane and 25% of the emission from higher latitudes [35]. In the ¼ keV band, the SWCX emission was shown bright enough to account for most of the emission in the plane of the galaxy where the LHB is least extended [37]. Similarly, there were various estimates of SWCX contribution to the ¾ keV band emission. Koutroumpa et al. [36] calculate the OVII intensity of 0.3-4.6 LU and the OVIII intensity of 0.02-2.1 LU in front of several clouds observed by the *XMM-Newton*, *Suzaku* and *Chandra*, and used a time-dependent model of the SWCX to show that the charge exchange emission was bright enough to account for the observed intensity. Smith et al. [65] find 3.5 LU and less than 0.34 LU of OVII and OVIII respectively in front of a dense molecular

cloud, possibly from LHB and/or SWCX. Henley and Shelton [32] estimate 3.8±0.5 LU (OVII) and 1.4±0.3 LU (OVIII) from SWCX emission. Gupta et al. [68] find that during multiple observations of the same shadowing target, OVII flux vary between 1.5±0.61 LU and 4.14±0.90 LU, most likely due to SWCX. Snowden et al. [31] observe 2.1±1.1 LU (OVII) and 1.9±0.5 LU (OVIII) at 2σ and 4σ confidence level respectively from the helium focusing cone in the heliosphere. Yoshino et al. [34] estimate 2 LU intensity of OVII due to SWCX. Koutroumpa et al. [69] find that SWCX can account for ~46% of OVII emission (0.82 LU) using XMM-Newton observation of MBM 12 molecular cloud and SWCX models. Crowder et al. [33] set an upper limit of 1.2 LU OVII intensity from heliospheric SWCX. Most of the estimates have relied heavily on models of the SWCX that are suffering from uncertainties associated with the lack of accurate input parameters, such as the estimation of solar composition and the interaction cross-sections.

Separating the SWCX from the background is possible by looking at its spatial signature. The slowest time-varying component of the SWCX emission originates in the interplanetary medium, and should show a significant geometric variation due to the focusing of the neutral helium into a Helium Focusing Cone (HFC) [66]. The flow of interstellar neutrals through the Solar System is due to the motion of the Sun through the ISM at ~26 kms^{-1} [86]. The ISM contains mostly hydrogen atoms with about 15% helium. Interstellar hydrogen experiences gravitational force, but the repulsive force due to radiation pressure balances the gravity, and significant ionization due to charge exchange

with high-speed solar protons creates a hydrogen cavity around the sun. Hence, X-ray emission due to SWCX with interstellar hydrogen shows little geometric variation [38].

On the other hand, the radiation pressure force for helium atoms is small compared to the Sun's gravitational force [87]. The gravity significantly affects helium trajectories which execute Keplerian orbits and form a focusing cone downstream of the Sun (Figure 1.9) centered at ~6^0 below the ecliptic plane. This focusing effect results in a significant increase of helium density, which has the direct effect of increasing the SWCX X-ray emission. Since the gas flows from the direction of l~3^0, b~16^0, the Earth is upstream of the flow in early June and downstream of the flow in early December every year [39]. Since helium has a smaller ionization probability, it is not significantly depleted even at 1 AU (Astronomical Unit).

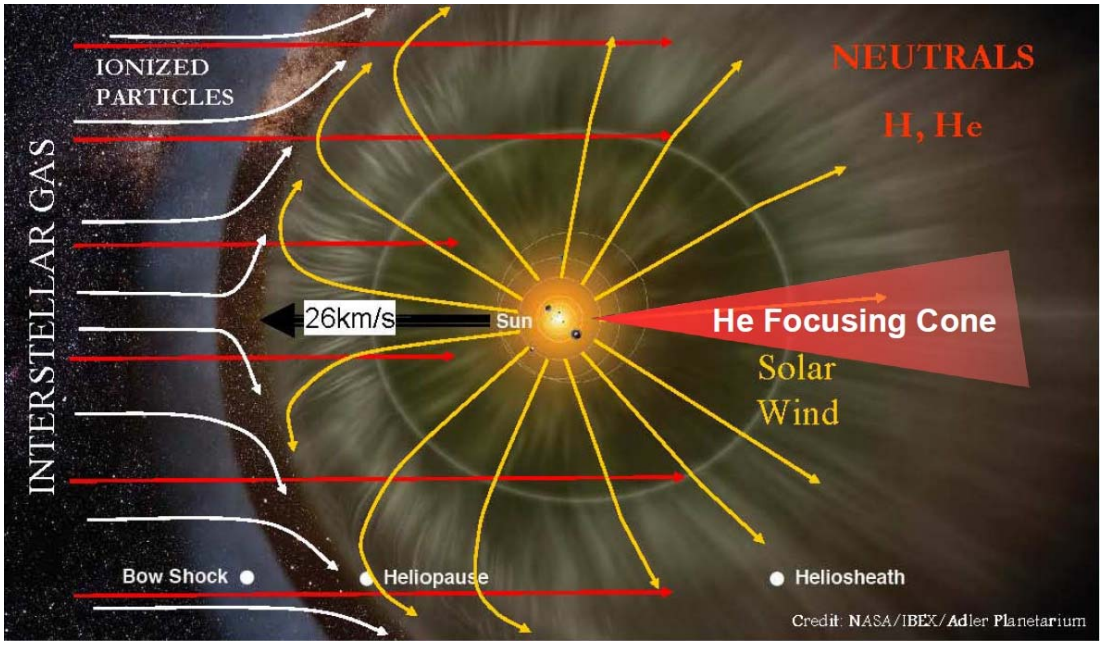

Figure 1.9: Helium Focusing Cone

The HFC has a FWHM opening angle of about 25 degrees, and at 1 AU its density peaks at ~0.075 cm^{-3} compared to a more typical density of ~0.015cm^{-3} of the ISM. The peak density drops with distance from the sun with a value of ~0.05cm^{-3} at 5 AU [38]. The cone is a suitable environment to quantify the SWCX and separate its contribution from the emission of the LHB. The best data on LHB we have so far comes from ROSAT's PSPCs in the ¼ keV and ¾ keV bands. SWCX contamination is calculated by choosing a sky direction of relatively uniform emission close to the plane of the galaxy and away from any bright sources to scan through the HFC, and comparing with ROSAT data taken while away from the HFC.

1.6 Expected Results

DXL planned to start scanning at l=185^0, b=-17.5^0, move to l=140^0, b=0^0 and turn back to scan through the predicted location of the HFC to help determine the fraction of the total diffuse emission produced by charge exchange in the Solar system. Figure 1.10 shows the planned DXL scan path (red band, slow scan of 0.7 deg/s) plotted on top of the ROSAT ¼ keV map centered at l=180^0, b=0^0 [39]. The white band (fast scan, 10 deg/s) represents the 360^0 scan through DXL FOV.

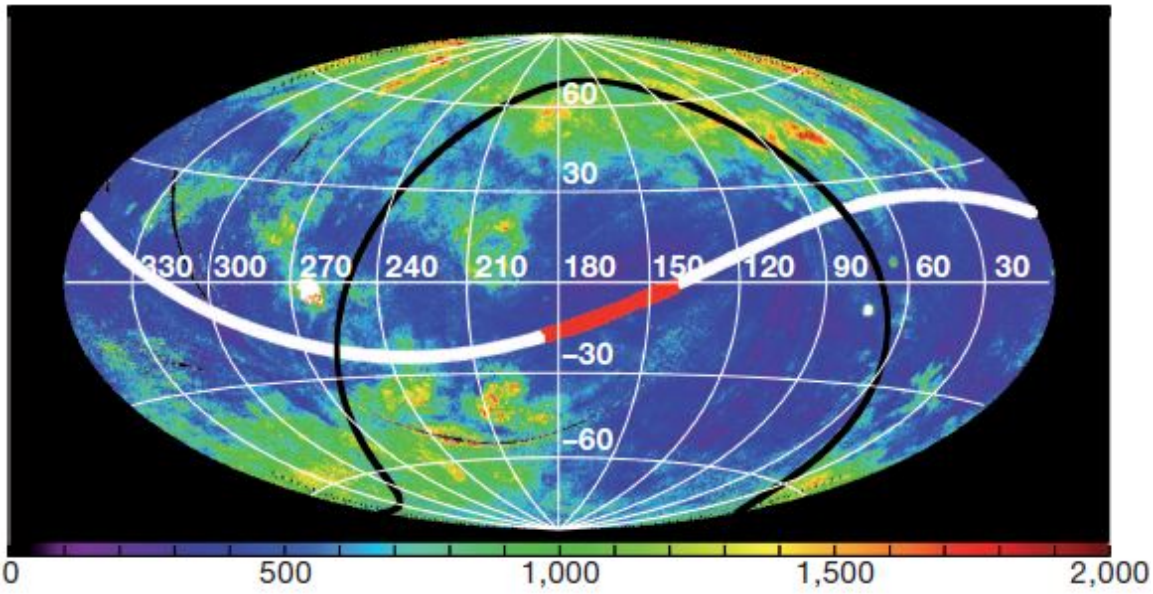

Figure 1.10: The DXL scan path (white band) shown plotted on top of the ROSAT ¼ keV map in Galactic coordinates. Red represents the slow scan portion of the scan-path. The black line is the 900 horizon. (Galeazzi et al. 2014)

The width of the band represents the half-power diameters of the instrument beam. In Figure 1.10, the black line is the 90^0 horizon for the DXL flight. Since the launch was in December when the Earth is inside the HFC, DXL scanned the chosen field through HFC. The same region of the sky was observed by ROSAT while approximately 1AU away from and parallel to the HFC in September 1990, so that its charge exchange contribution was not strongly affected by the cone enhancement. The DXL and ROSAT scan geometry is shown in Figure 1.11.

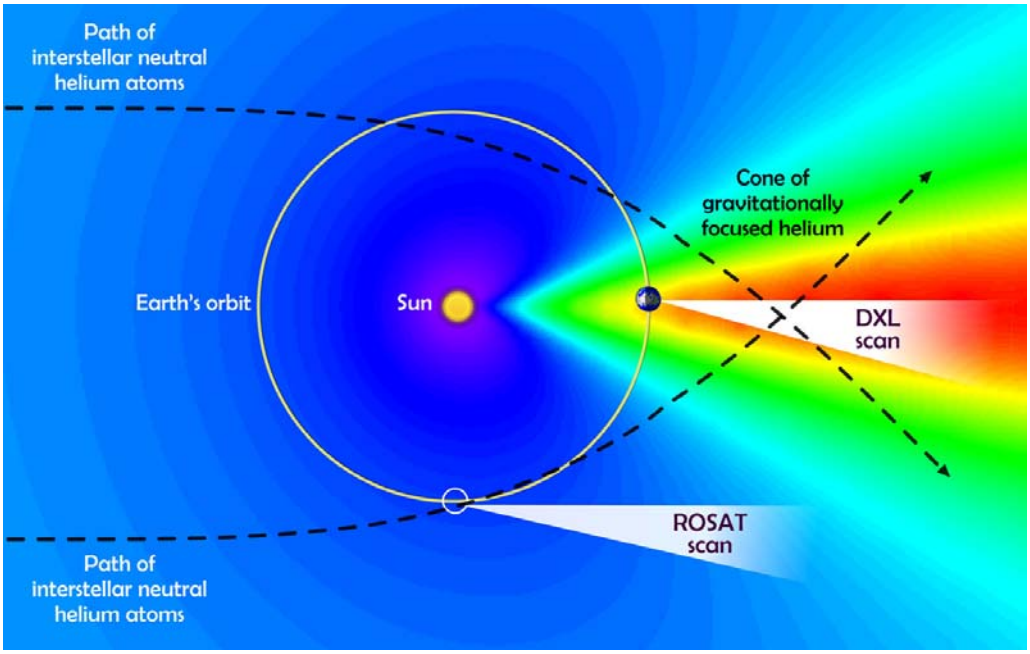

Figure 1.11: Interstellar helium density model showing the cone in red (red represents high He density while blue is lower density). DXL and ROSAT scan geometry are also highlighted, where DXL is inside the HFC during observation. The effect of HFC on ROSAT is small due to its observation geometry. (D. Koutroumpa)

We expected to determine the excess emission due to the charge exchange of the solar wind with the enhanced helium of the HFC by comparing our data with ROSAT. The expected count rates due to LHB and SWCX are shown in Figure 1.12, the right side of which shows the expected count rates as a function of galactic longitude across the scan path. We expected SWCX emission to vary from 300 RU to more than 500 RU in the ¼ keV, while expecting about 10 RU variation in the ¾ keV band. We expected the LHB emission to remain constant at about 100 RU (personal communication, D. Koutroumpa and collaborators). The spatial variation of the HFC is particularly evident in the R12 band.

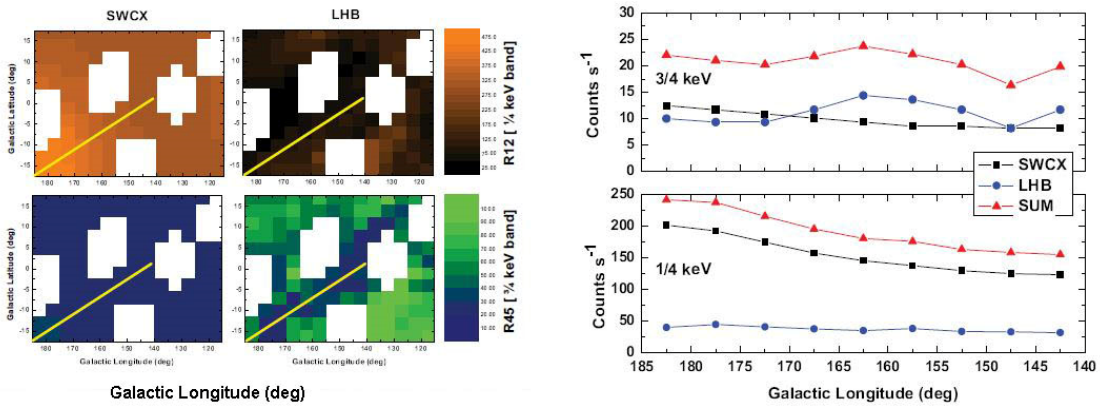

Figure 1.12: Expected contributions of SWCX and LHB in RU in the ¼ keV (R12) and ¾ keV (R45) energy bands. The figure on the left shows expected SWCX rates within selected co-ordinates. The plot on the right shows expected DXL count rates along the chosen path (shown as yellow line in the left figure) [88]

CHAPTER 2 **THE MISSION**

2.1 DXL Mission

The Diffuse X-ray emission from the Local Galaxy (DXL) is a sounding rocket mission to study the spatial variation of Solar Wind Charge Exchange (SWCX) emission to identify and separate the contribution of SWCX emission from the Local Hot Bubble (LHB) emission to the Soft X-Ray Background (SXRB). The project is led by Dr. Massimiliano Galeazzi of University of Miami, Coral Gables, FL. The other collaborating institutions are: NASA's Goddard Space Flight Center, Greenbelt, MD, 20771, U.S.A., Department of Physics and Astronomy, University of Kansas, Lawrence, KS 66045, U.S.A., Université Versailles St-Quentin; Sorbonne Universités, UPMC Univ. Paris 06 & CNRS/INSU, LATMOS-IPSL, 78280, France, The Henry A. Rowland Department of Physics and Astronomy, Johns Hopkins University, Baltimore, MD 21218, U.S.A., GEPI Observatoire de Paris, CNRS, Université Paris Diderot, 92190, Meudon, France, Department of Atmospheric, Oceanic, and Space Sciences, University of Michigan, Ann Arbor, MI 48109, U.S.A. and Department of Physics, University of Wisconsin, Madison, WI 53706, U.S.A. NASA's Wallops flight Facility and White Sands Missile Range are heavily involved in the launch operations.

2.2 Objectives

The main objective of the DXL mission is to quantify SWCX contribution to the ROSAT ¼ keV and ¾ keV bands. Temperatures, pressures and distributions of the plasma of the LHB and the Galactic Halo (GH) can be calculated with higher accuracy if we could isolate SWCX contribution in both the ¼ and the ¾ keV bands. Knowing the physical conditions of the plasma will lead to more accurate pictures of the solar neighborhood, the bubbles of hot gas produced by supernova or stellar wind when they are near the end of their existence [38], and the GH. DXL will provide an estimate of the heliospheric SWCX correction to University of Wisconsin-Madison and ROSAT data, and to any other current and future investigations of extended sources. Furthermore, the observation of low surface brightness objects such as the hot plasmas in nearby superbubbles, the interstellar medium in our galaxy, the Magellanic Clouds, and nearby galaxy and galaxy clusters are affected by SWCX contamination. It is essential to construct effective models of the foreground SWCX emission to be able to interpret and model the observations of such objects accurately.

2.3 Strategy

DXL was launched in December, when the Earth is directly behind the Sun and inside the Helium Focusing Cone (HFC). By scanning a selected region of the sky through the HFC, and comparing with the observation of the same region obtained by ROSAT when the line of sight does not intersect with the HFC, we could provide an estimate of the

SWCX emission. We were particularly interested in making the observation during the solar maximum in December of 2012/2013. The last solar maximum occurred in 2001, and given the cycle of ~11 years, we launched close to the solar maximum period. The solar maximum corresponds to lower heliospheric SWCX emission and was expected to be sufficiently bright, but not dominating the LHB emission during this time [38]. We also accounted for the possibility of Thomson scattering occurring when X-rays from the Sun's corona scatter elastically with the electrons, and fluorescent scattering of the upper atmosphere. So we chose to observe at an angle greater than 120^0 from the Sun making the contamination negligible[89].

There were several strategic requirements to satisfy for successful science (Figure 2.1). They are listed below [88]:

a. Launch in early December when the HFC is aligned with the Sun-Earth line, directly opposite the Sun to maximize scan through HFC
b. Limit scan to $\pm 20^0$ from the Galactic plane to assure that only "local" emission is detected
c. Avoid significant bright point sources
d. Scan a region of the sky where the LHB emission is expected to be relatively uniform
e. Moon must be $>45^0$ from the target area (Figure 2.2)
f. Solar zenith angle $>120^0$ to avoid scattered X-rays (Figure 2.2)

g. The launch must be done at night to avoid the X-rays from the Sun (Figure 2.2)

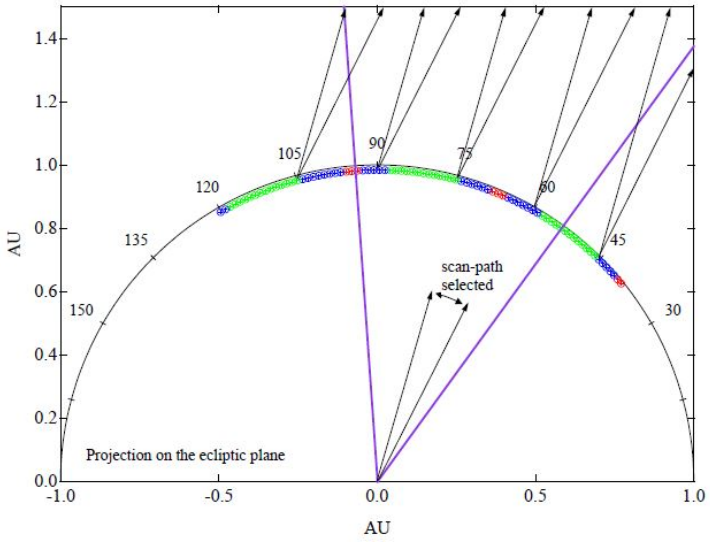

Figure 2.1: Projected DXL scan path (black lines) on the ecliptic plane for few selected dates of December 2012. Small colored circles represent the Earth's position between Novembers 1st, 2012 and January 20th, 2013, color coded for moon interference (green representing the least interference from the moon). The orientation of HFC (purple lines) is shown extending out from the Sun at 0 AU (credit: D. Koutroumpa)

Figure 2.1 shows the projected DXL scan path on the ecliptic plane. The orientation and size of the HFC is also shown in purple lines. The central arc is the Earth's orbit, and the Earth's positions from November 2012 through January 2013 are shown in small colored circles. Green denotes the absence of the moon from the midnight sky.

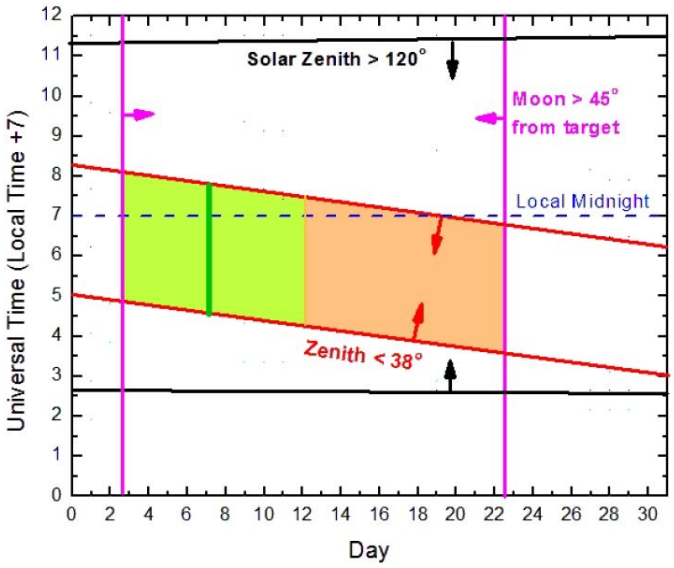

Figure 2.2: DXL launch window showing the ideal dates and times for days of December 2012. The best dates have the minimal effect of the Sun and the Moon (green shaded region) (M. Galeazzi)

2.4 Payload and Launch

Current and near-term satellite missions have only a very limited grasp (a product of effective area and solid angle). They are limited in their ability to study low-brightness, diffuse emission, especially in the ¼ keV band, where the bulk of the LHB and SWCX emission is. High energy resolution instruments, such as the X-ray Quantum Calorimeter (XQC) sounding rocket experiment [17] and the Astro-H, have the resolution in the soft band (<10 eV at 1 keV) to observe individual lines in the ¼ keV and ¾ keV bands. These instruments lack the collecting area, angular resolution, and temporal scale to constrain global SWCX foreground models. At the same time, current X-ray observatories generally

use CCD detectors that have relatively high backgrounds, low grasp, significant pointing constraints, and often negligible effective area at ¼ keV. However, what is not possible with much longer satellite observations can be accomplished with a dedicated sounding rocket mission. DXL employs two large-area proportional counters with high grasp (10 cm^2 sr both in the ¼ and ¾ keV bands), making them an ideal choice for detectors to study the diffuse emission due to charge exchange. Since the DXL mission uses large area proportional counters with mechanical collimators, its grasp is much larger than any other current or near future mission at ¼ keV [38]. The counters used by the DXL mission were made in the 1970s at the UW, and they were operated for almost a decade during the Wisconsin All-Sky Survey [11]. They were preserved in a storage room at the UW campus in close to mint condition. We refurbished them to meet our requirements, especially upgrading some of the electrical components to meet the requirements for Wallops telemetry, and used them for our experiment. The counters were originally mounted on a Magnesium frame designed to fit into a 15" diameter Aerobee 170 launch vehicle. NASA/Wallops built a new aluminum frame for DXL to fit with Black Brant IX's 17.25" diameter skin.

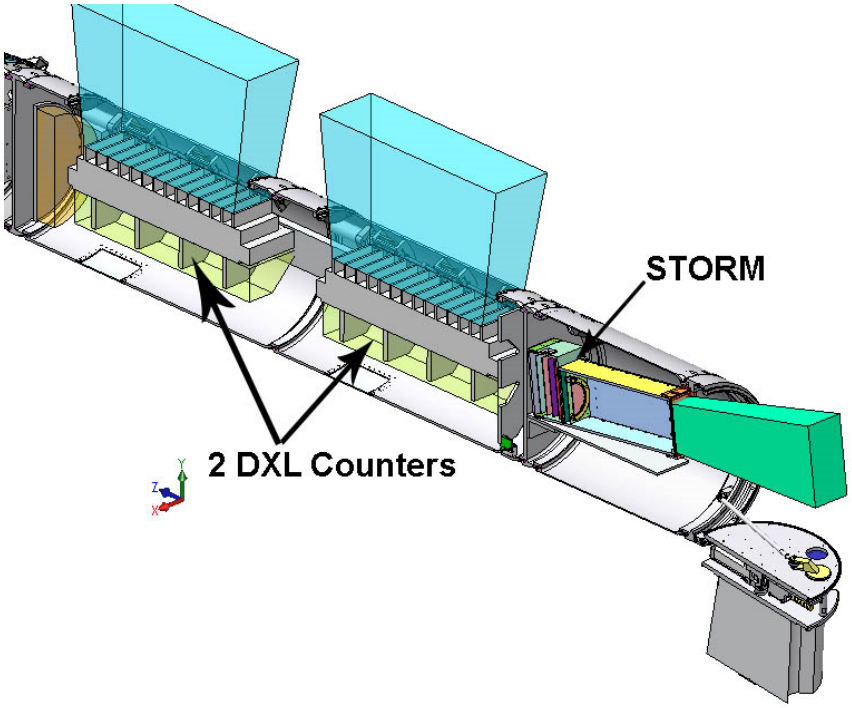

Figure 2.3: Cross section of the DXL payload with STORM section. The two DXL detectors are installed at the front end of the payload while the STORM is at the aft end [88]

Figure 2.3 shows a cross section of the science payload with two detectors. At the aft end of the payload was another secondary prototype experiment, the Sheath Transport Observer for the Redistribution of Mass (STORM). STORM is a prototype wide field-of-view soft X-ray camera using newly developed slumped micropore ("lobster eye") optics and microchannel plate detector [89]. STORM was a technology demonstration. This was a first time such technology was flown in space to provide a proof-of-concept for future flight instruments employing the tested technology (Collier et al., in preparation).

The payload was assembled and tested at the Wallops Flight Facility. The electrical and mechanical integrity of the payload was carried out at the facility two months prior to the scheduled launch. While everything went smoothly, the thin film windows were damaged during random vibrations in the thrust direction. Adding vibration dampers and updating window installation procedures successfully remedied the issue. The payload was transported to the White Sands Military Range in New Mexico for launch. The launch was scheduled for December 9th, 2012. However, a scheduling conflict with Collisional Avoidance System (COLA) pushed the launch to December 12th. The launch took place at 22:20 local time. There were some issues with the rocket motor that increased the vibrations, but no damage was done to the experiment. The telemetry system successfully sent the data in real time to the ground station. The payload was recovered in the morning.

CHAPTER 3 **THE INSTRUMENT AND CALIBRATIONS**

3.1 Proportional Counter

Two mechanically collimated proportional counters are the main DXL detectors. Proportional counters were first developed to improve on the capabilities of Geiger counters. The first X-rays were detected using Geiger counters, which were just cylindrical ionization chambers with fine co-axial anode wire. As a particle enters the chamber through a window in the cylinder, it interacts with an atom or a molecule of the gas inside, liberating one or more electrons in the process (Figure 3.1). A large voltage applied across the anode wire causes complete ionization of the gas, with ionization current making a "spark" noise indicating arrival and detection of a particle. The energy information of incoming particle is lost in the process.

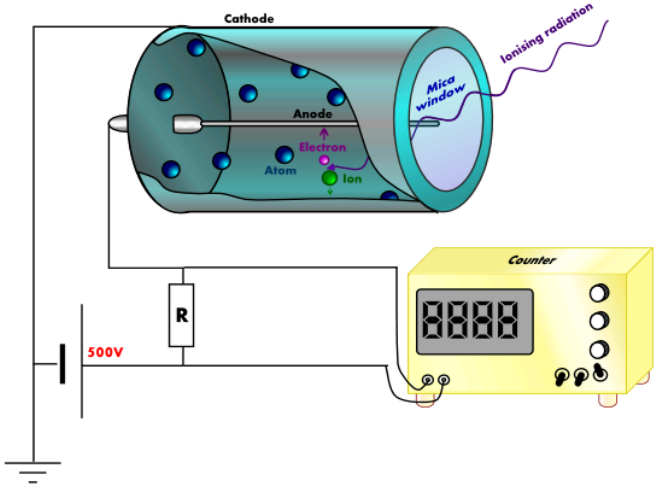

Figure 3.1: An ionization chamber (credit: www.wikipedia.org)

To retain the energy information of the incoming X-ray photon however, the anode voltage has to be regulated [90]. Figure 3.2 shows how the charge collected at the anode wire of an ionization chamber relates to the operating voltage. If the anode wire voltage is kept within the "proportional counting region", the final number of electrons is proportional to the initial number of electrons that participated in the avalanche. Hence such ionization chambers are called "proportional counters". Proportional counters work in the "proportional counting" region of the curve [91]–[93].

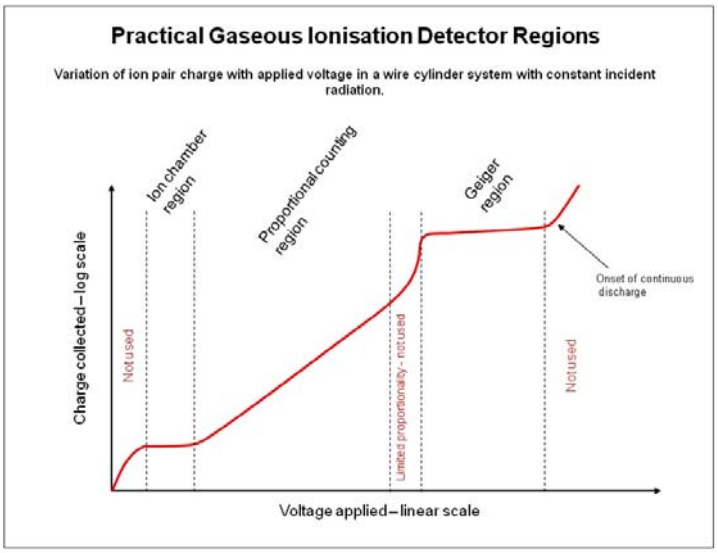

Figure 3.2: Charge collected vs anode voltage curve (credit: www.wikipedia.org)

The charge collected is proportional to the applied voltage in the linear region of the curve. Since the photon energy information is preserved in the avalanche process, the collected charge can be read to determine the energy of the incoming photon. Each cascade

of electrons creates a pulse of electronic charge that is then carried by the wire into the electronic chain of the detector for output. The height of the pulse directly relates to the energy of the incoming photons.

Proportional counters have been used extensively in X-ray astronomy. They can be designed to have high efficiency and wide bandwidth with low background. They can be constructed arbitrarily large to allow for increased statistics. However, they have poor energy resolution, especially below the carbon edge where $\frac{E}{\Delta E} \sim 1$. The X-rays are detected by the voltage pulses they produce in the detector. The mean voltage of the pulse height distribution is proportional to the energy of the photons. However, the relationship is not truly linear. Besides, proportional counters have limited resolution, requiring indirect method of analysis of almost any spectrum. Generally, a trial input spectrum is folded through a detector response, and the predicted pulse height spectrum is compared with observed data. The input spectrum is modified iteratively until a good match is obtained. It is therefore imperative to obtain an accurate response model of a proportional counter. The response of proportional counters can be modeled successfully from a limited set of calibration data following techniques developed and published by Jahoda and McCammon [94].

Jahoda and McCammon [94] state that the distribution of collected charge q from an avalanche of one electron is given by the Polya function $P(q, \mu, h)$;

$$P(q,\mu,h) = \frac{1}{\mu}\frac{h^{\mu}}{\Gamma(h)}\exp\left(\frac{-hq}{\mu}\right)\left(\frac{q}{\mu}\right)^{(h-1)} \quad 3.1$$

where μ is the mean effective charge produced ("gas gain"), and h is a width parameter. The net pulse height distribution produced by monoenergetic photons is given by the weighted sum:

$$R(q) = \sum\nolimits_i \left(Q(i)P(q,i\mu,ih)\right) \quad 3.2$$

where *Q(i)* is the probability that exactly *i* electrons reach the avalanche region. *Q(i)* is calculated as:

$$Q(i) = Q'(i) - \sum_{m=0}^{i-1}\left(Q'(i)\kappa\left(1-\frac{m}{i}\right)^{(\kappa-1)}\frac{1}{i}\right) + \sum_{n>i}\left(Q'(n)\kappa\left(1-\frac{i}{n}\right)^{(\kappa-1)}\frac{1}{n}\right) \quad 3.3$$

where, $\kappa = D/w\lambda$, *D* being the diffusion coefficient, *w* the drift velocity and λ the mean absorption depth. The three terms in equation 3.3 represent the probability of creating exactly *i* electrons, the probability of losing one or more electrons given an initial production of *i* electrons, and the probability of initially producing more than *i* electrons and losing all but *i* of them, respectively. Jahoda and McCammon conclude in [94] that for any photon with energy E_γ, $Q(i)$ can be derived with given values of *a)* average amount

of energy required for each additional ionization (*W*), *b)* the effective Fano factor (*f'*), *c)* the ratio of diffusion coefficient to drift velocity (*D/w*), *d)* the mean free path in P-10 (λ) and *e)* the energy offset between adjacent atomic absorption edges (ΔE_k). The final step then remaining is just convolving $Q(i)$ with equation 3.1 to determine the output pulse height distribution (Equation 3.2). Based on calibration data, we calculated the DXL response using the theory described above quite successfully (see section 3.11 for details).

3.2 DXL Proportional Counters

Two refurbished proportional counters from Aerobee payload (University of Wisconsin-Madison) are the main DXL instruments. The two proportional counters are made of magnesium. The detectors are wire-walled with a 3-sided anti-coincidence system. The operating gas is P-10 (see section 3.9), which is a generic name for 90% argon, 10% methane mixture. Each counter is equipped with magnets, collimator, nickel mesh and filter window assembly in the front. Cathode and anode wire grids, and veto wires are inside the chamber. On the back of each counter are gas maintenance system and electronics. Radioactive Fe-55 X-ray source is also installed behind a solenoid shutter to expose the detectors to X-rays during flight to track gain changes. All of these components that comprise a DXL detector are described in details in the next few sections that follow and in references [11] and [38]. Figure 3.3 shows the various parts of each DXL detector. The right side of the figure shows two detectors mounted on a frame and assembled inside a rocket skin. The magnets of the detectors can be seen from the open doors. Both detectors

are mounted on an aluminum frame and installed in the rocket skin prior to launch. The side-looking rocket doors open after reaching prescribed altitude and expose the detectors for observations.

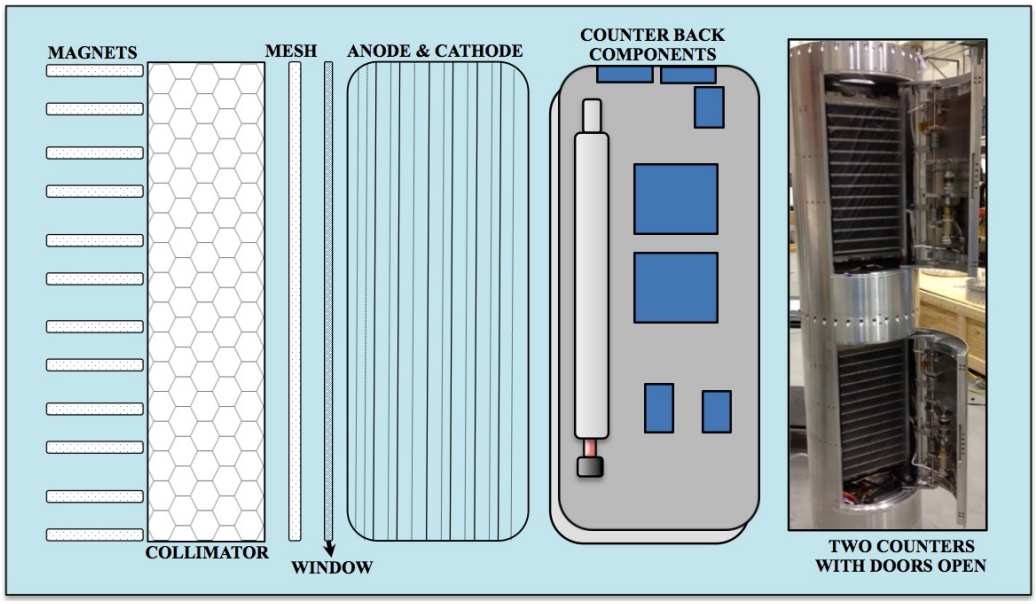

Figure 3.3: Schematic of DXL proportional counter. From left to right, magnets, collimator, mesh, window, chamber with anode and cathode wires, the back of each counter, and a photo of the two counters inside rocket skin with doors open are shown

3.3 Magnets

There are 14 ceramic magnetic bars installed forward of the collimator of each DXL counter providing a minimum field of 150 gauss throughout the honeycomb and extending 4 cm above it [11]. The primary purpose of the magnets is to sweep away the electrons that may contaminate the pure X-ray events. The magnets can reduce the electron particle flux

incident on the counter face by over 90%. See [11], [95] for details on the effects of electron contamination.

3.4 Collimator

The collimators are made of 6.35×10^{-5} m thick aluminum into a honeycomb mesh with 0.312 cm cells and 2.54 cm depth and 6.5^0 FWHM. After precision machining, they are sprayed with black paint to reduce X-ray reflections. Finally, an ultra-smooth coating is performed to assure that no harm is done to the mesh or the window. Extensive tests were performed at UW, especially for X-ray reflections at low energies, using boron, carbon, fluorine, aluminum and titanium K_α energies. The details of the calibrations and modeling procedure is outlined in [95]**.** The results were slightly improved by David Burrows in 1982 [96], and we used his numbers to calculate the response. Table 3.1 shows the functions governing the response of the two collimators. The functions are plotted in Figure 3.4.

Energy Range (eV)	CI- Solid Angle (sr)	CII- Solid Angle (sr)
E>650	0.0132	0.0132
650>E>277	$0.0132*1.136*(E/277)^{-0.1499}$	$0.0132*1.114*(E/277)^{-0.1262}$
E<277	$0.0132*1.212E/183)^{-0.1557}$	$0.0132*1.818*(E/277)^{-1.1826}$

Table 3.1: DXL collimator response

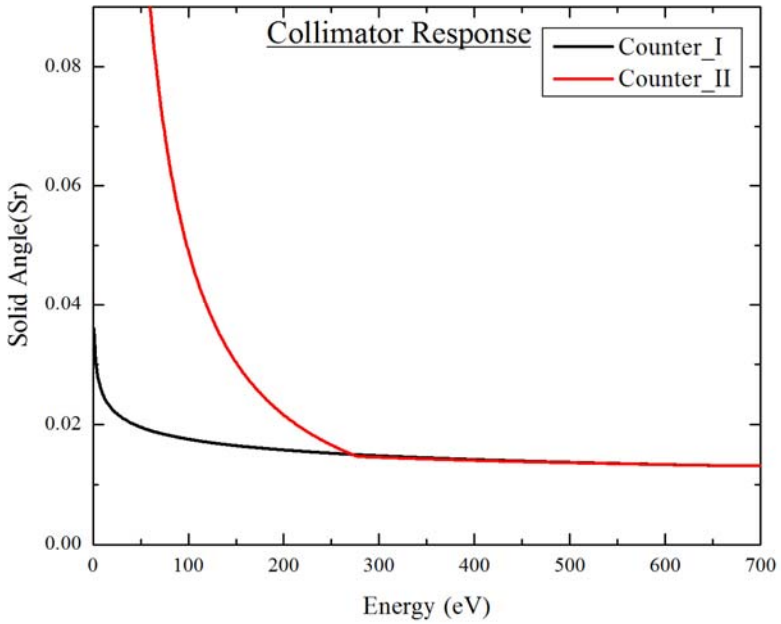

Figure 3.4: Solid angle vs energy curve for DXL collimators

3.5 Mesh

DXL windows are extremely delicate and are unable to support the internal pressure of the chamber without any support. A nickel mesh of 30.48 cm × 60.96 cm in area is used to support the film. The mesh is made of 0.0254 mm thick nickel wire interweaved at 100 lines per inch spacing. Each counter uses 1 mesh. We obtained the DXL meshes from the UW. The meshes were in good condition. Visual inspection showed no signs of appreciable deformity and we verified their integrity during vibration tests at Wallops.

Transmission tests were performed in a dark room using laser. Since each side of a single mesh cell at about 25.4×10^{-5} m, almost 1000 times larger than the wavelength of the

laser used, our transmission results would be accurate enough for X-rays. We used Thor Labs' laser (model # HRP020), in combination with photodiode (model # S120VC), to calculate the transmission of the mesh. The 632.8 nm red Helium-Neon laser with $1/e^2$ beam diameter of 0.81mm had an output of ~1.70±.01 mW during testing. The beam diameter roughly covered 200 cells at one time. We made a Styrofoam template with 17 holes spread over most of the mesh's active area to support the mesh, and checked for transmission at 5 regions in each of the 17 selected areas as shown in Figure 3.5.

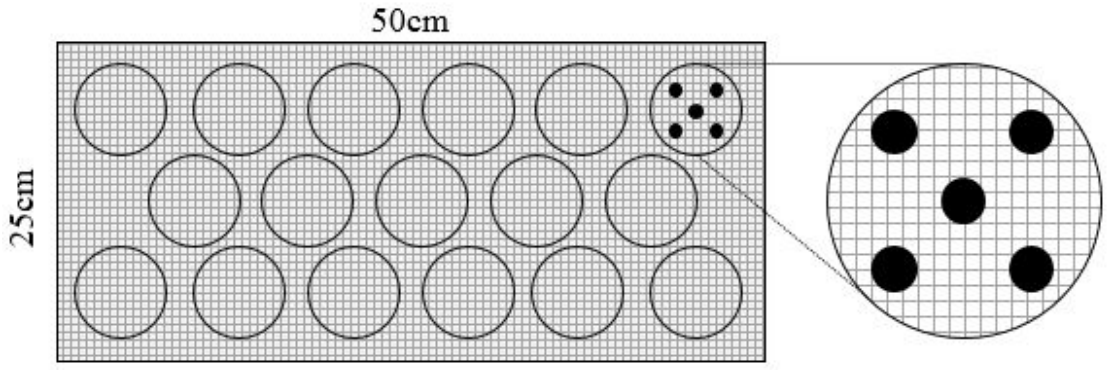

Figure 3.5: Mesh transmission measurement schematic

We checked transmission at 85 different evenly spread positions on the mesh. Laser power was recorded using the photodiode without any interference, and then immediately checked for transmission through the mesh to avoid any significant changes in the laser power. The flight meshes for both counters were tested in such set-up. We calculated that the transmission of CI mesh was 62±1%, while CII mesh was 60±1%.

3.6 Anode and Cathode Wires

There are 6 main anode wires made of 0.0762 mm thick Kovar to detect events. They are surrounded by 10 veto anodes (8 underneath, 2 on sides of main anodes) made of the same material and with the same thickness. The coincident events in the bottom and side veto anodes eliminate almost all of the detected cosmic events and Compton electrons from gamma rays that may contaminate the pure X-ray events [11]. Kovar ground wires (0.127 mm) surround each main anode in a "wire-walled" design. A high voltage supply provides ~2200 V on the anodes. The layout is shown in the Figure 3.6. The arrows indicate the positions of ceramic posts used to stretch the anodes across the counter body. Six main anodes are indicated by yellow arrows. Eight out of the ten veto anodes are directly underneath the main anodes, while 2 (# 2 and #10 in figure, blue text) are parallel to the main anodes at two sides of the detector body (blue arrows).

Figure 3.6: DXL anode and cathode wire arrangements

3.7 Window

Thin film windows are required for three main purposes. The first purpose is to seal the chamber of the detector body to hold the gas inside. Second, when the film is coated with special compound, it blocks UV from contaminating the detectors. Most importantly, the lack of resolution of a proportional counter is complimented by the use of absorption edge of coating material to separate the event into "bands". DXL windows were predominantly carbon, with K_α absorption edge at 284 eV, and so the X-rays below 1 keV are separated into two bands similar to ROSAT R12 (1/4 keV) and R45 (3/4 keV) bands shown in Figure 1.3. The windows are made of Formvar ($C_5H_7O_2$), a plastic that can be cast as films when mixed with ethylene dichloride. Another compound, UV-24 ($C_{14}H_{12}O_4$), is mixed in appropriate proportions to block UV rays effectively [97], [98]. The films are ~90 $\mu g/cm^2$

in thickness which makes them extremely delicate to handle, store and install. The windows are so thin that the P-10 gas can diffuse, albeit very slowly, requiring a set-up to maintain P-10 gas levels inside the detector during the experiment.

DXL used windows made by the UW group during the DXS Shuttle mission. The two windows mounted during the flight were numbered 92-126 and 92-136. The first DXL counter (CI) was mounted with window number 92-136 while the second DXL counter (CII) was mounted with window number 92-126. The transmission and composition study were conducted during a trip to UW after the flight. The calibrations were performed in a vacuum tank with a set-up for XY motion of the window. A small proportional counter was also mounted facing some variable fluorescent sources and an alpha-target.

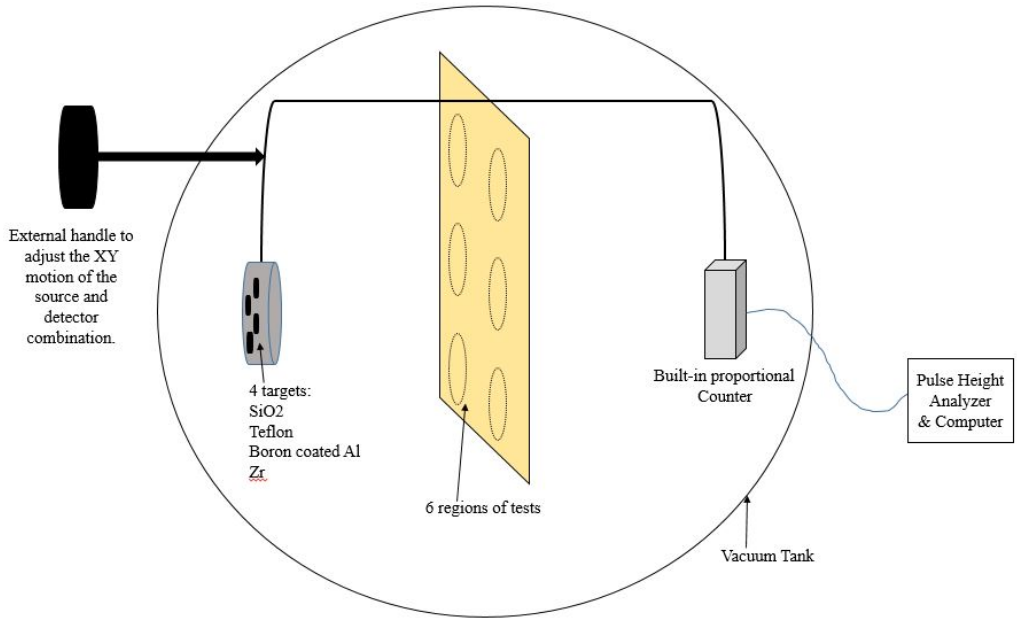

Figure 3.7: Window calibration set-up representing X-ray source, window and detector inside a vacuum chamber

The XY movable stage is adjusted externally to align the X-ray source and detector combination to any of the selected test region as shown in Figure 3.7. The proportional counter is connected to an external Pulse Height Analyzer (PHA) to observe and transfer the data to a computer. First, the X-ray emission for each target is observed without any window interference. Observation of the same source through the window will reduce the counts observed by the PHA, which is again recorded. The process is repeated for multiple sources. We used SiO_2, Teflon, boron coated aluminum, and zirconium targets for the calibration of DXL windows. Radioactive iron was also mounted during all testing to

observe the gain changes. The measured composition of each window is listed in Table 3.2. The calculated transmission as a function of energy is shown in Figure 3.8.

Window	92-136 (CI)	92-126 (CII)
Formvar	65.09 μg/cm^2 ± 4.69 μg/cm^2	70.41 μg/cm^2 ± 4.15 μg/cm^2
UV-24	18.41 μg/cm^2 ± 3.55 μg/cm^2	15.52 μg/cm^2 ± 3.78 μg/cm^2

Table 3.2: DXL window thickness

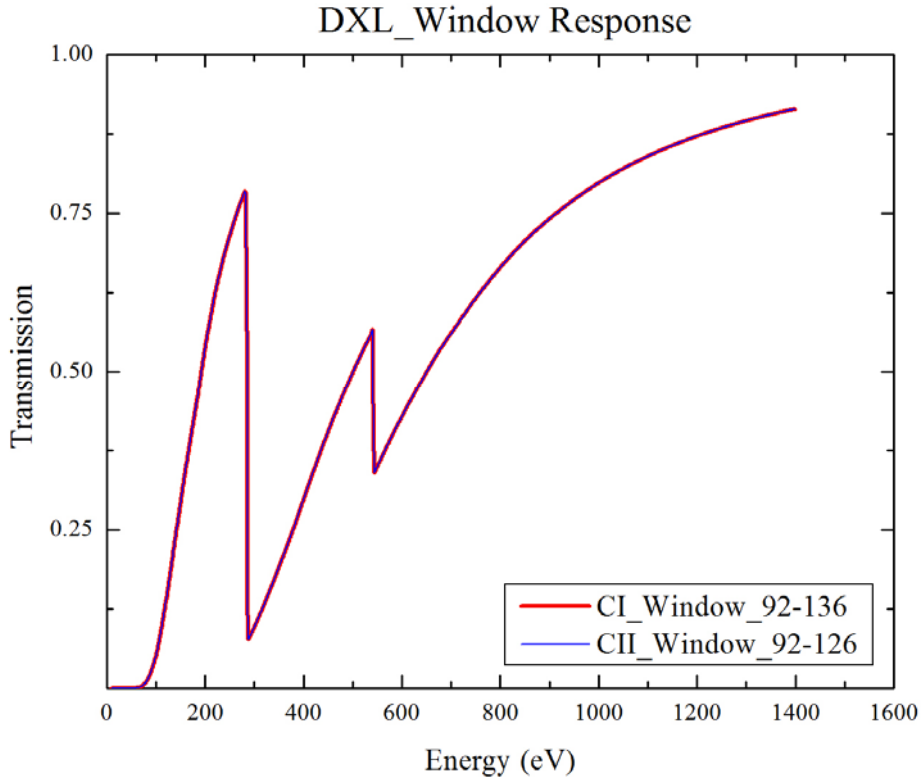

Figure 3.8: DXL windows transmission vs energy plot for both counters. The curves overlap due to similarity of transmission

3.8 Pressure Regulation System

DXL counters have elaborate gas storage and maintenance system to assure optimal p-10 gas density during flight. There are various components working in concert to keep the gas maintained in the counters during testing, calibration and flight. Figure 3.9 shows a schematic of the backside of DXL counter where all the gas related parts are installed.

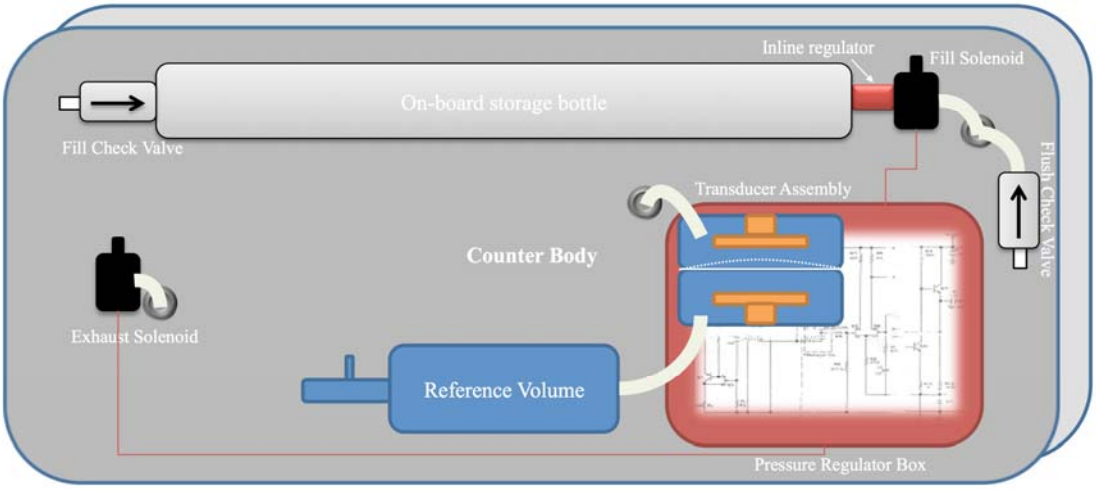

Figure 3.9: DXL counter back on-board gas storage and maintenance schematic

The main components are the on-board storage bottle, two solenoids, reference volume, pressure transducer assembly and the pressure regulator box. The pop-off valves and gauges are also mounted on each detector as necessary. The on-board bottle is filled to 1800 psi using a high-pressure hose through an external cylinder. The counter can be flushed clean with nitrogen or P-10 gas (see section 3.9) through check valve, while opening the exhaust solenoid at the same time. Pressure transducer assembly is opened to

the inside of the counter on one side and to the reference volume on the other side. When the pressure regulator is operational, the transducer compares the pressures inside the detector chamber with the reference volume, and triggers the fill solenoid to open to let gas flow from the bottle to the counter volume. The reference volume on CI was filled with P-10 gas at 772.7 Torr at 25^0C in Miami, while CII reference volume was set at 773.08 Torr. Normal atmospheric pressure at White Sands Missile Range in New Mexico is ~660 Torr compared to ~770 Torr in Miami. It is important that the gas density in the reference volume is constant since gas gain depends on density. Hence the reference volume is thermally connected to the counter body to assure it is in same temperature with the detector.

3.9 P-10 Gas

DXL proportional counters operate in P-10 gas. It is a generic name for a mixture of 90% Argon (Ar) and 10% Methane (CH_4) gas. The advantages in the use of P-10 are the gas stopping efficiency in the entire energy range of 0.1 to 10 keV. The methane acts as a "quench" gas. The quencher component in the counter gas is essential for stable avalanche operation at useful gas gains [99], [100]. Methane quenches the excited states of argon and governs the drift velocity, both essential for controlled avalanches [101].

The mean absorption depth λ of P-10 gas was calculated from [102]. A FORTRAN routine was composed to automatically generate λ values for the energy range of interest to input into the main program to generate a DXL response. Our routine quite successfully

replicated the values obtained from the reference in the wide range of energies shown in Figure 3.10. The value of λ is a critical parameter in modeling the response of a proportional counter as described in section 3.1.

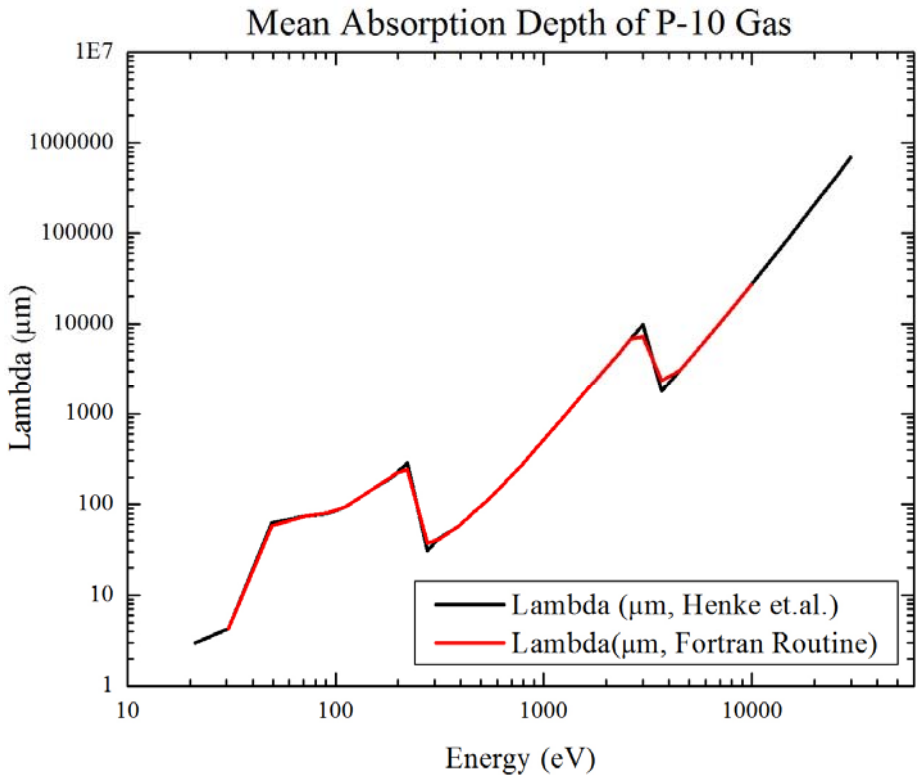

Figure 3.10: Mean absorption depth of P-10 gas vs energy

3.10 Electronics

A complex assortment of electrical components work in tandem to output the X-ray signal as a pulse height and transmit via telemetry to the ground station during flight. Some of the electronics are mounted on the back of each counter, while others reside on the "top-

plate", a plate mounted on the the front end of the payload. The backside of each proportional counter contains two stacks of electronic components, and they communicate with the top-plate electronics for data in and out of the telemetry. The "digitizing", multiplexing and timing circuits are installed on a top plate and they directly hook up to the telemetry (TM). The main amplifiers are mounted towards the front end of each detector. The pulse stretchers, pulse stretcher logics, discriminators, veto gates, secondary amplifiers and pulse buffers are stacked into two boxes. The layout of the electronics are shown in Figure 3.11.

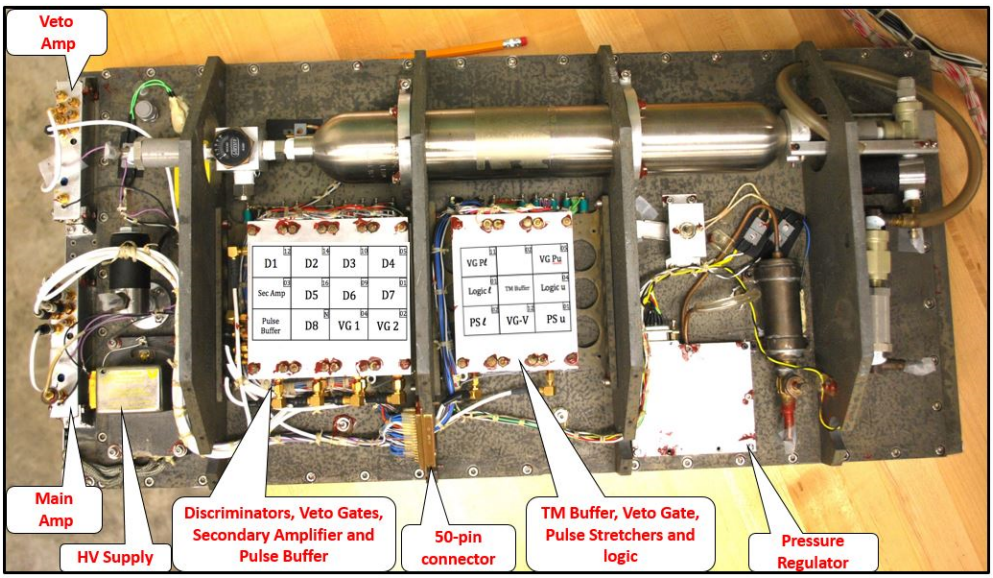

Figure 3.11: Electronics stacks on the back side of each DXL detector

The set of electronics are prescribed with specific tasks to identify, sort and transfer X-ray signals, and reject any events that are not valid X-rays. A simplified version of the electronics interconnectedness is depicted in Figure 3.12.

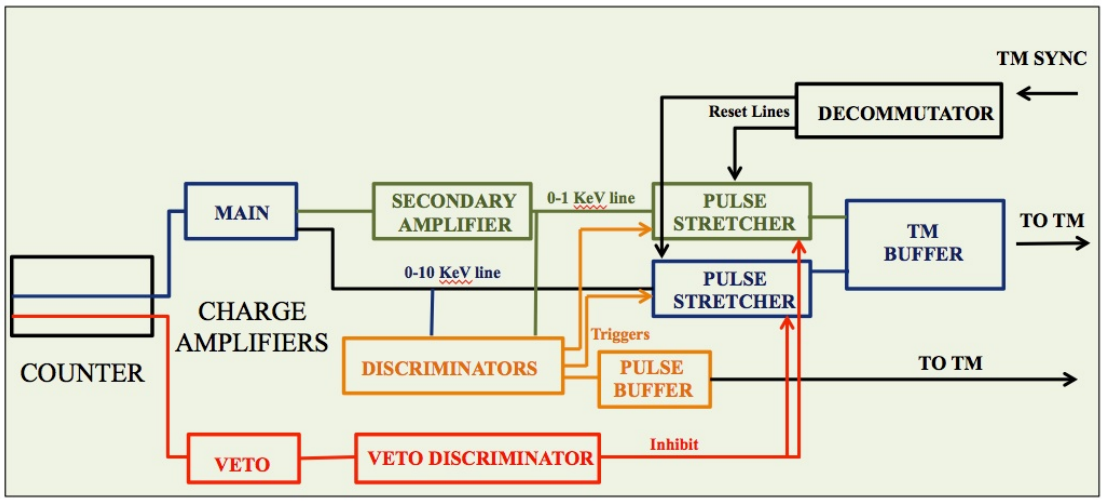

Figure 3.12: Simplified DXL electronics schematic

The X-ray charge pulses from the main amplifiers (blue line) are transferred to pulse stretchers, which are buffered out to telemetry interface. The 0 - 10 keV pulses from main amplifiers are transmitted down the upper pulse stretchers, and is called the UP channel. The 0 - 1 keV pulses from the main amplifiers are voltage amplified by the secondary amplifiers, and obtained from the lower pulse stretchers, or the LOW channel. The signals from the veto amplifiers (red lines) are used to identify and inhibit non-x-ray events at pulse stretchers. Backup science can be obtained from Discriminators, which also have a vital role in "triggering" pulse stretchers for "good" events. The data are transmitted real-

time through NASA's telemetry (TM) system. Descriptions of important electronic systems, along with calibration information, are provided in next few sub-sections.

3.10.1 Charge Amplifier (CA)

There are two charge amplifier boxes mounted towards the front of each detectors, labeled main amplifier (MA) and veto amplifier (VA). Charge pulses generated by X-rays in the main anode wires in each counter is read out by the MA. Each box has several outputs to transfer the signal. One of the main amplifier outputs is directly sent to upper channel (0-10 keV) of data acquisition line. Second output line is further amplified by a secondary amplifier and sent down the lower channel (0-1 keV). Other outputs relay the charge information to discriminator boxes. Each amplifier can be calibrated by an external pulse generator through an input line in the amplifier box. Ordinarily, the input of the main amplifier is connected to an internal pulser (Section 3.10.10), and used to cross calibrate the UP and LOW channels during counter operation.

The linearity of the main amplifiers can be tested by sending pulse signal from external pulse generator through a capacitor and measuring the output pulse. The MAs on the two detectors are linear, with gain of 13.60 in CI and 11.67 in CII as shown in Figure 3.13.

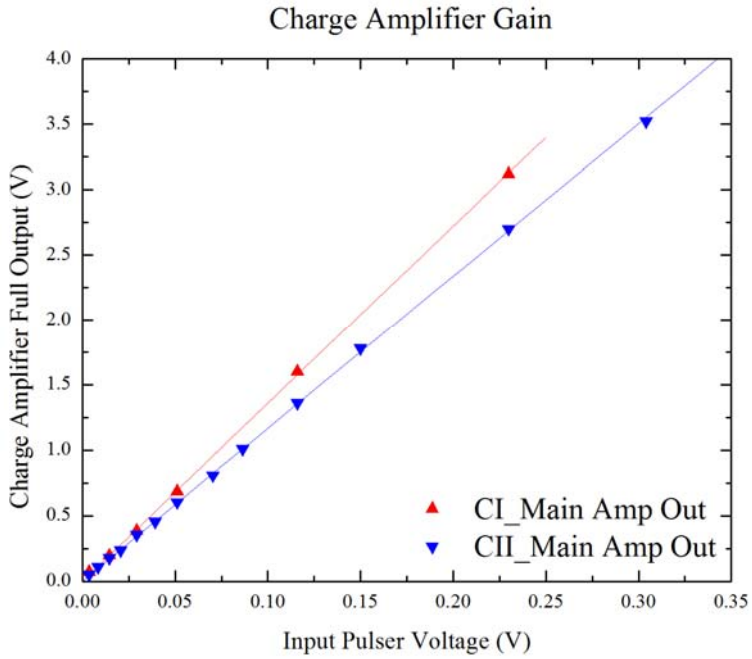

Figure 3.13: Charge Amplifier output vs input voltage supplied from external pulse generator through a 2 pf capacitor

3.10.2 Veto Amplifier (VA)

The veto anodes are connected to the Veto amplifiers, and they carry the non-X-ray signals like particle background events, into the data acquisition chain to inhibit a dubious event from being recorded as a useful event. Veto amplifier drives the lowest level discriminator to trigger veto effect on the circuitry to eliminate non-X-ray signals. The veto amplifiers on both counters were checked and calibrated before the flight just like main amplifiers. We find gains of 53.42 and 54.92 respectively for CI and CII veto amplifiers (Figure 3.14).

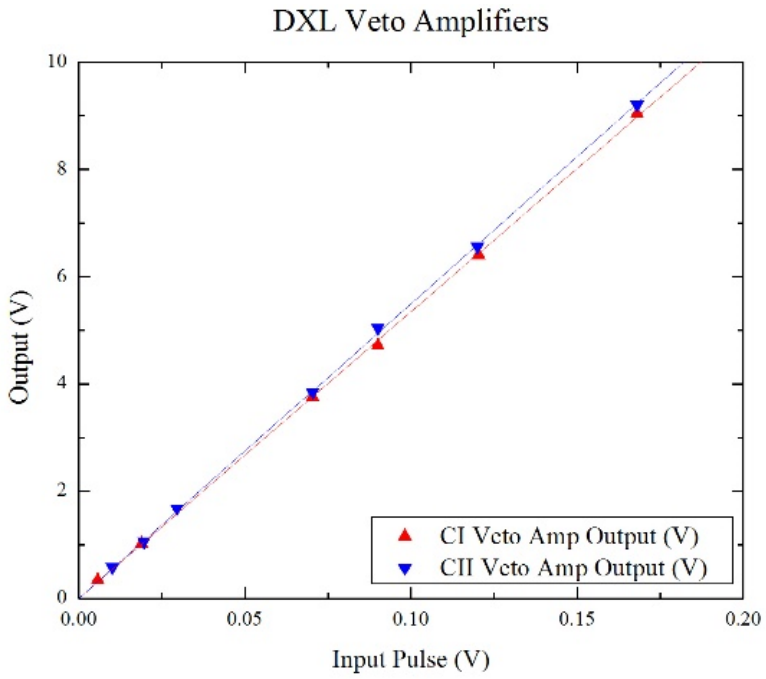

Figure 3.14: Veto Amplifier output vs input voltage supplied from external pulse generator through a 2 pf capacitor

3.10.3 Secondary Amplifier (SA)

Secondary amplifier is just a voltage-to-voltage amplifier employed to expand the voltage scale when the energy is below 1 keV. One of the outputs of the secondary amplifier is transmitted as primary signal to the lower channel (0 - 1 keV). Other outputs connect to the first four discriminators, D1 through D4. CI and CII secondary amplifier gains are 9.679 and 11.564 respectively and fairly linear as shown in Figure 3.15.

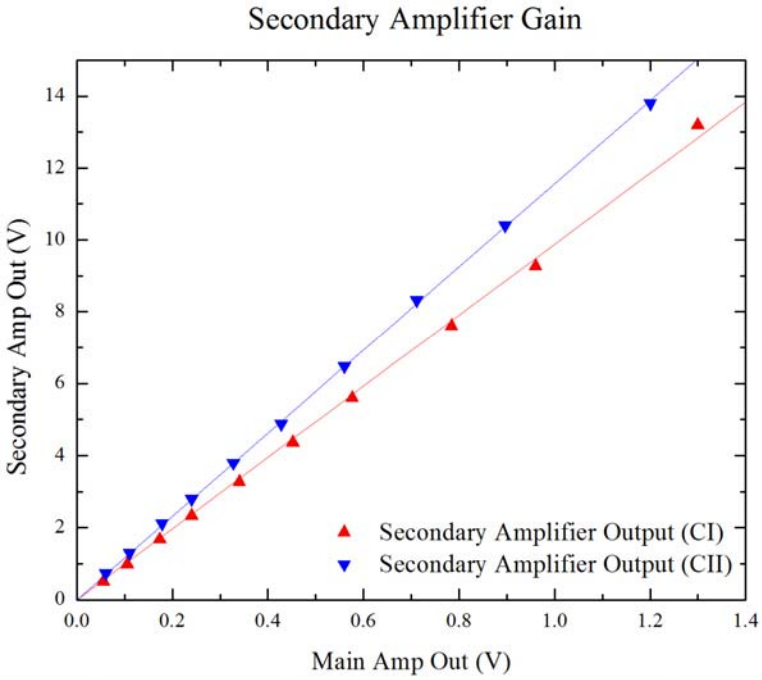

Figure 3.15: Gain of DXL Secondary Amplifiers

Note that the gain of the secondary amplifiers can also be calculated from the ratio of lower Pulse Stretcher to upper Pulse Stretcher outputs (section 3.10.4). We find that the gain calculated in this method is best since the ratio links directly to the ratio measured by the telemetry. Using this technique, we calculated gains of 7.957 (CI) and 10.059 (CII) from the data taken just before flight. I re-did the test 9 months later, and found gains of 7.56 (CI) and 9.75 (CII), both within 5% difference.

3.10.4 Pulse Stretcher and Logic

There are 4 pulse stretchers, UP and LOW for each detector. The LOW channel transmit X-rays in the energy range of 0 - 1 keV and the UP channel handles 0 - 10 keV

signals. The science signal directly goes into the UP pulse stretcher from the main amplifier. The signal is however amplified by secondary amplifier before going into the LOW pulse stretcher. These circuits simply hold the highest voltage they receive until they are digitized. The input inhibit is always on if a pulse is waiting to be digitized, thereby rejecting another larger pulse that may arrive prior to the first pulse being telemetered. There is also a reset input to reset the gate for another pulse once the pulse being held is telemetered. Pulse stretchers work closely with the logic for pulse stretcher that mainly does checks and balances of the data in and out of the pulse stretchers. It receives the trigger signal from the lowest discriminator (section 3.10.5), indicating that there is a pulse, and cross checks with veto gate (section 3.10.6) to verify that it is a valid pulse.

We calibrated the pulse stretchers prior and after the flight. Figure 3.16 shows the outputs of pulse stretchers few days before the flight plotted against the main amplifier. These data were obtained through the NASA TM section. The linearity of the PSs did not deviate significantly when tested post-flight through TM simulator over 6 months later.

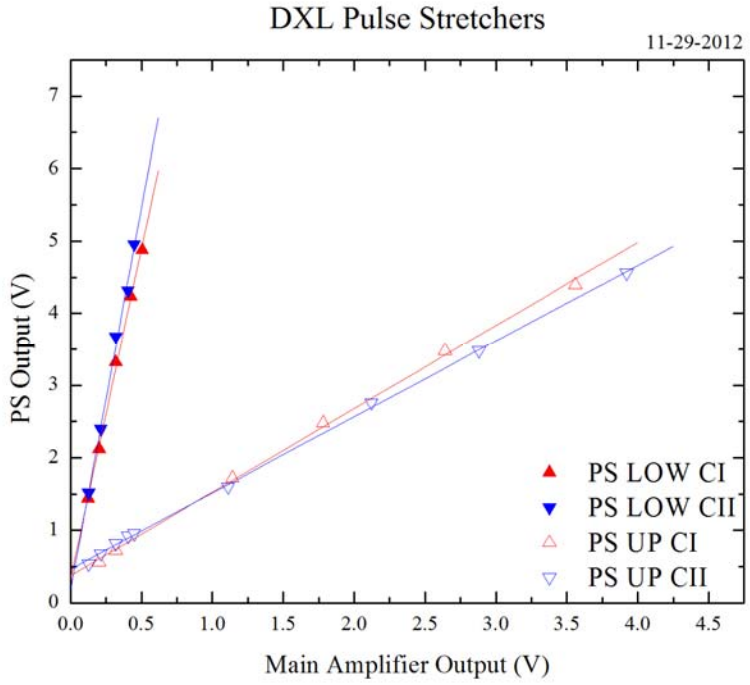

Figure 3.16: DXL pulse stretchers output voltage plotted against the main amplifier output

The ratio of the slopes of the LOW and UP channels (Secondary Amplifier gain) comes out as 7.957 for CI and 10.059 for CII as discussed in section 3.10.3. There are offsets present in the linearity of the pulse stretchers, introduced from the main and the secondary amplifiers. They are calculated from the position of the internal calibration peaks described in section 3.10.10.

3.10.5 Discriminators (D)

A set of Discriminators are used to “discriminate” the signals according to their “pulse height” and provide an estimate of the pulse amplitude as a backup for the main pulse

acquisition system. Each counter has 8 discriminators, D1 through D8. D8 is also called veto discriminator since it receives a veto signal directly from veto amplifier. The signal from veto discriminator is sent to the Veto Signal Veto Gate (section 3.10.6) which ultimately inhibits the system to discard the signal as non-X-ray event.

Each discriminator also has two inhibit inputs, one from a veto gate, and other from a higher discriminator. Two outputs are obtained from each discriminator, an integral output any time signal crosses the threshold and a differential output if signal is above the threshold and input inhibits are off. A variable resistor can be adjusted to set the threshold input value. The levels of the seven non-veto discriminators are set at:

	D1	D2	D3	D4	D5	D6	D7
Counter	eV	eV	eV	eV	eV	eV	eV
I	125	278	444	972	1666	4720	7774
II	62	199	416	832	1661	4596	7701

Table 3.3: Discriminator levels

The main discriminators are mounted in a cascade mode, where the output of each is connected to the inhibit input of the one just below it. The differential counter of each discriminator outsources the good events, while the integral output is counting all events that trigger it.

3.10.6 Veto Gates (VG)

Veto Gates regulate the overall data acquisition scheme. There are 5 veto gates in operation; Veto Signal Veto Gate (VSVG), High Discriminator Veto Gate (HDVG), Low

Discriminator Veto Gate (LDVG), PSU Veto Gate (PSUVG) and PSL Veto Gate (PSLVG). VSVG is the main veto gate that drives all the other gates directly or indirectly. The deadtime of the detectors are obtained from the other 4 veto gates.

3.10.7 Top Plate Electronics

The top-plate houses decommutator, housekeeping A and B, DC-DC converters and a board with multiple power distribution posts. Decommutator produces the timing signals from the TM clock and Frame Sync to reset the detector pulse height peak holding circuits shortly after they have been read out by the TM. Various monitors (temperature, voltages, solenoid states, pressures) are handled by the two housekeeping boxes. Six Mil Electronics MS85 low-noise DC-DC converters use 28V input supply to output +5, +10, -10 and +25 volts required by the electronic boxes. Two 50-pin cables carry the signal from the detectors to the top-plate. Each cable also carries DC voltages for the experiment, the reset signal from the commutator, and the control signals for the detector operations. The top-plate components are shown in Figure 3.17.

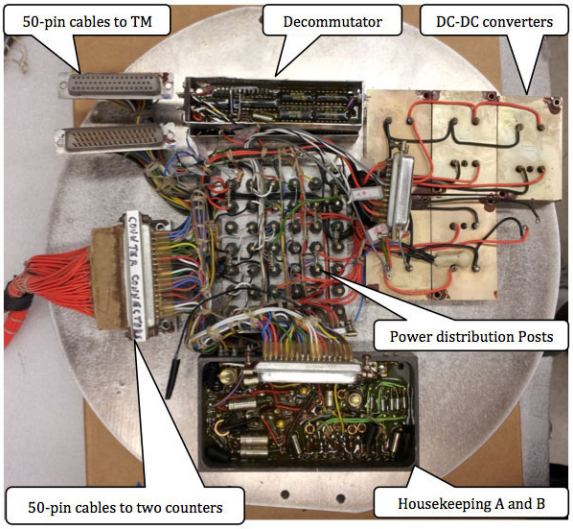

Figure 3.17: Top-plate electronics of DXL, with connectors to TM

3.10.8 Ground Support Equipment (GSE)

Ground Support Equipment (GSE) is a fully analog large metal box with various meters, interface connectors, LEDs and BNC outputs in the front. Behind the casing, a complex assortment of parts are intricately installed. A 28V power supply, clock, digital and analog boards are on the back of the GSE. Figure 3.18 shows the front and back of the DXL GSE.

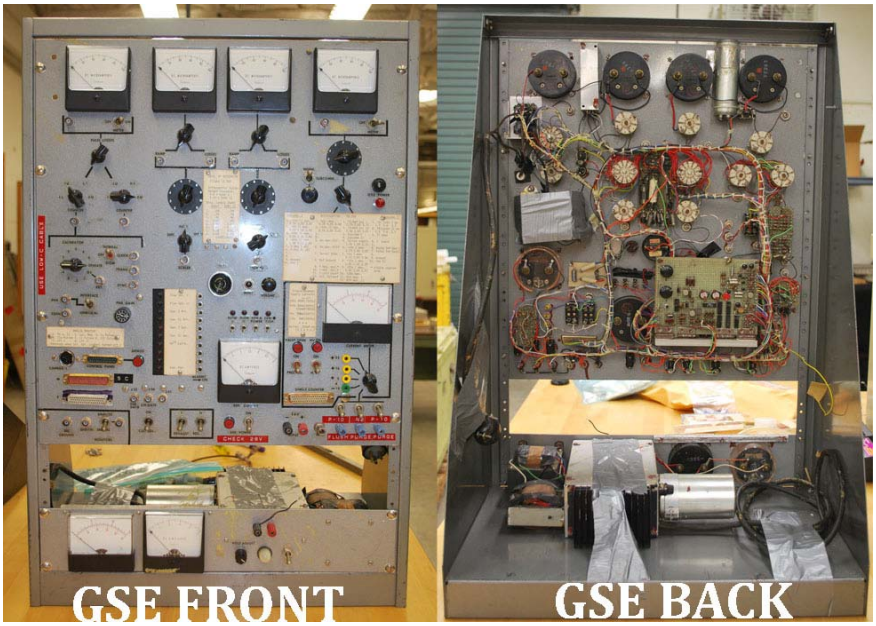

Figure 3.18: DXL GSE (Front and back view)

The GSE runs in 3 modes, namely, the Single Counter Mode (connecting the counters directly, one at a time), the Payload Mode (connecting to both counters simultaneously through top-plate) and the Umbilical Mode (25-pin connector hooked up to Wallops Flight Facility control panel). GSE can be used to control the experiment, and in addition, can output discriminator counters, deadtime, housekeeping data, and clock and PS analog signals. To send the signals from the GSE to a computer, we built a "computer GSE" that receives digitized signals from the "hardware GSE." Computer GSE requires a TM simulator and Frame Sync (provided by NASA/Goddard Space Flight Center) to digitize and serialize payload data from the hardware GSE. Frame Sync synchronizes serial data into TM matrix format (see section 3.10.9 and Figure A.5) and sends the frames in packets through USB to the computer. A LabVIEW program reads and displays the DXL data in

real-time. The simulator was designed to digitize our data in the same way the NASA's TM encoder does during flight.

3.10.9 Telemetry (TM) Format

DXL telemetry runs on an 8 MHz clock (1.25μs). Data is organized into 10 bit words (12.5μs), and the words arranged into a 16-word frame called the Minor Frame (200μs, labeled 1-16). 32 minor frames, labeled 0 through 31, make a paragraph called the Major Frame (6.4ms) (see Figure A.5). A TM simulator and a Frame Sync were built by NASA Goddard Flight Center working in tandem with the GSE software to transmit and digitize DXL signals real-time during calibrations in the lab.

Our calibrations were done through the TM simulator while flight data was obtained through the real NASA TM. To compare the TM simulator and the real TM, we triggered the main amplifiers and checked the output signals for comparison. The outputs are obtained on a GSE computer in the 0 - 1024 channel signal. To obtain a direct way to convert charge to channel, we used an external pulse generator to trigger main amplifiers through a 2 pF capacitor and obtained the data via TM simulator post-flight and via real TM just prior to flight. We fitted the output against the input charge (Using Q=CV, where C=2 pF and V= input voltage) and obtained (Figure 3.19) the following relation:

CI: Channel=1.073E16*charge, CII: Channel=1.0995E16*charge-22.4.

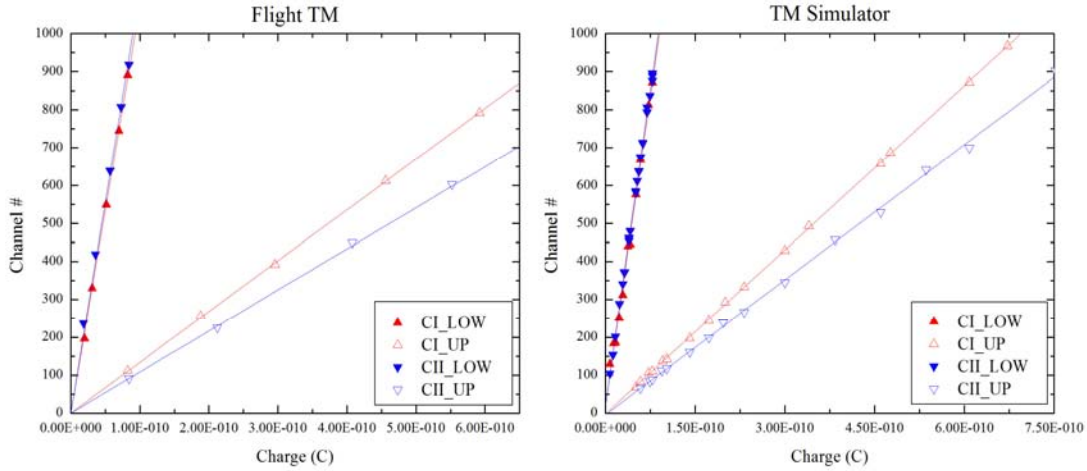

Figure 3.19: Charge to channel conversion calculated for flight TM and TM simulator

We find that the charge to channel conversion is consistent between the TM simulator (used for calibrations) and the NASA's TM (Used for flight). We can simply re-scale the data by the Fe-55 line when converting the calibration data from TM simulator to flight without any additional corrections!

3.10.10 Internal Pulser

A built in circuitry, activated by the calibration solenoid control, sends a pulse into the charge amplifiers that appear simultaneously in the UP and LOW channel. Such arrangement facilitates a conversion factor between the two channels to cross calibrate them and check electronic gain. Besides, any offsets that may occur in the electronics chain are calculated from the positions of the pulser in the UP and LOW channels as $= \frac{G \times U - L}{G - 1}$, where O=offset, G=secondary amplifier gain, U= pulser peak in the UP channel and

L=pulser peak in the LOW channel. For all the calibrations, we consistently used the above relation to calculate any offsets.

3.10.11 Ground

We noticed a 20-30 mV offset between the voltages sent to TM by the DXL counters and the voltage read by TM in the housekeeping data. In addition, there was a residual signal, synchronized with the clock on the experiment return line. We figured out that such effects were due to grounding issues. DXL grounding is bit complicated in a sense the counter body are part of ground themselves. Each counter acts as a common ground point rather than the skin of the payload. The common ground is used for the DC lines from the counters to the interface plate, causing the offset, and the same return is used for the clock, causing the residual clock signal. The grounding set-up of DXL and TM section is shown in Figure 3.20. We minimized the effect of grounding errors as much as we can, while resorting to offset calibration for integrations, flight and calibrations.

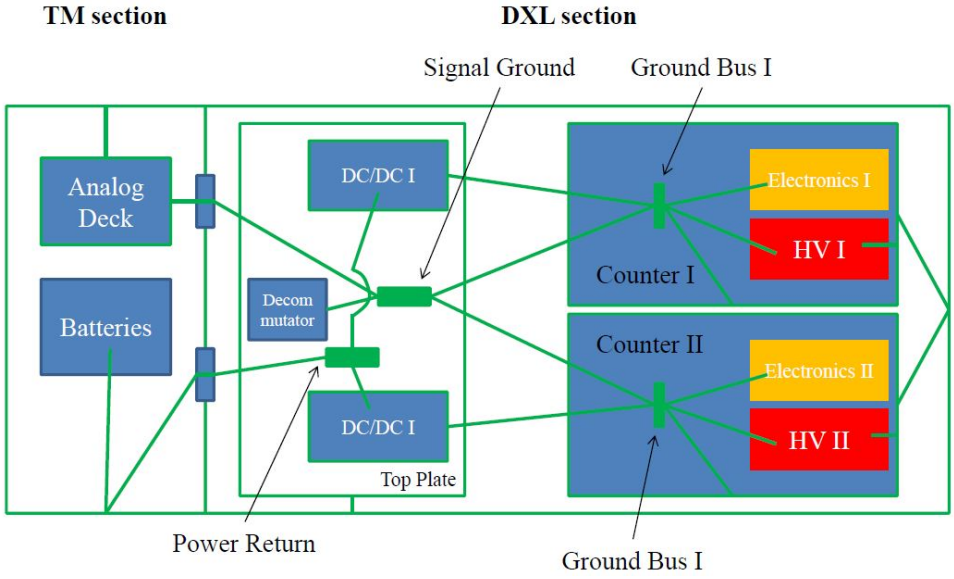

Figure 3.20: Ground setup of DXL detectors

3.11 Detector Calibrations

Measuring the outputs of each detector by exposing them to monochromatic X-rays enables us to obtain the non-linearity of the detectors and build accurate response function. We use Be, Zr, B, C, N, O, Fl, Al, Si and Fe energy lines to check for linearity of DXL detectors. The first 9 are fluorescent sources activated by radioactive 100 µCi Po-210. 100 µCi Fe-55 radioactive isotopes are also installed on the DXL detectors that emit 5900 eV photons. Table 3.4 lists the energy lines along with their energies used to calibrate DXL detectors.

Element	Line	Energy (eV)	Material
Beryllium (Be)	$K_{\alpha 1,2}$	108.5	Be Foil
Zirconium (Zr)	M_{ζ}	152.6	Zr Foil
Boron (B)	$K_{\alpha 1,2}$	183.3	Boron Nitride (BN_2) wafer
Carbon (C)	$K_{\alpha 1,2}$	277	Teflon
Nitrogen (N)	$K_{\alpha 1,2}$	392.4	Boron Nitride (Bn2) wafer
Oxygen (O)	$K_{\alpha 1,2}$	524.9	Silicon Dioxide (SiO_2) wafer
Fluorine (Fl)	$K_{\alpha 1,2}$	676.8	Teflon
Aluminum (AL)	$K_{\alpha 1,2}$	1486	Aluminum plate
Silicon (Si)	$K_{\alpha 1,2}$	1740	Silicon Dioxide (SiO_2) wafer
Iron (Fe)	-	5900	Radioactive Fe-55 capsule

Table 3.4: DXL calibration lines

Each detector is pumped down to sub-torr pressures in a vacuum tank, and exposed to the fluorescent sources to obtain the output pulses through computer GSE. We built a custom support along the rails of the vacuum tank so we could move the sources across the surface of each detector. Each source is placed inside a small aluminum holder with radioactive Po-210 bombarding it. X-rays generated in this manner are directed towards the detector.

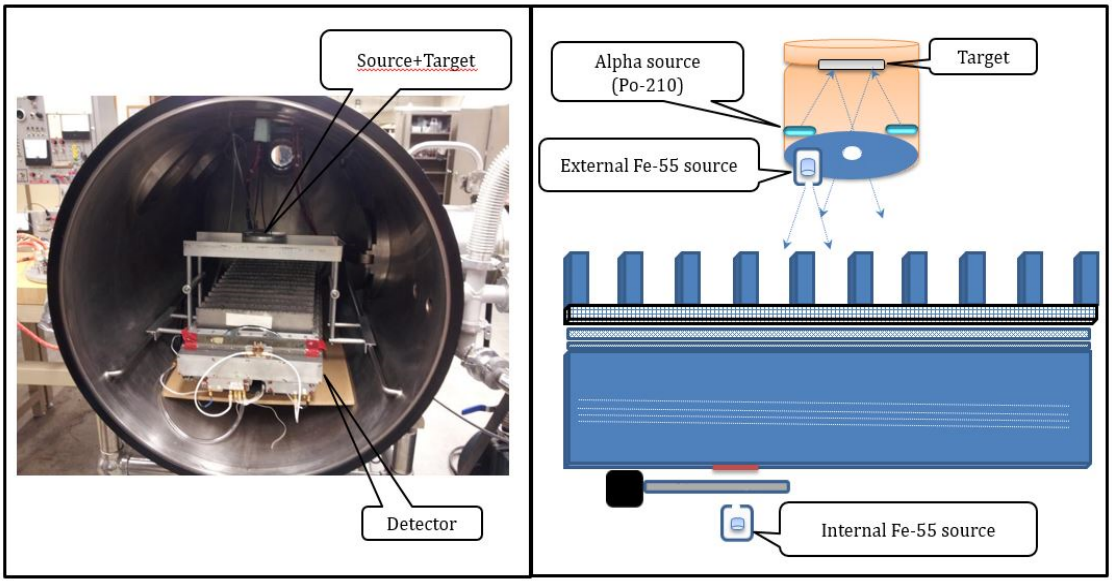

Figure 3.21: DXL calibrations set-up, left side showing a photo of one detector inside a vacuum tank. An aluminum stage carries a container with X-ray sources, and slides back and forth along the rails. The container can move along the perpendicular axis of the rails. The right hand schematic shows the arrangement of internal and external iron sources, along with Po-210 and fluorescent targets

The DXL calibration set-up is shown in Figure 3.21. The left side of the figure shows one detector installed inside a vacuum tank, with fluorescent source and Po target in a holder placed on Al support structure. The counter pressure is regulated internally via pressure regulation system to assure consistency in pressure during calibrations. The right hand side of the figure shows a general schematic for calibrations, including internal Fe-55 source regulated by a calibration solenoid gate. To cross-calibrate both channels, an internal pulser automatically comes on when the calibration solenoid is turned on.

For each energy line, we collected the data twice: with and without the calibration solenoid turned on. When the solenoid is off, we just see the calibration line and the external iron line. When calibration solenoid is on, there are two calibration pulser lines and an internal iron line in addition to the above mentioned lines. The data are then plotted in Origin to find the peak positions of the calibration lines, the internal pulser and Fe-55. Each calibration line has at least four peaks between the UP and the LOW channels: calibration peak, external iron peak, internal iron peak, internal pulser peak.

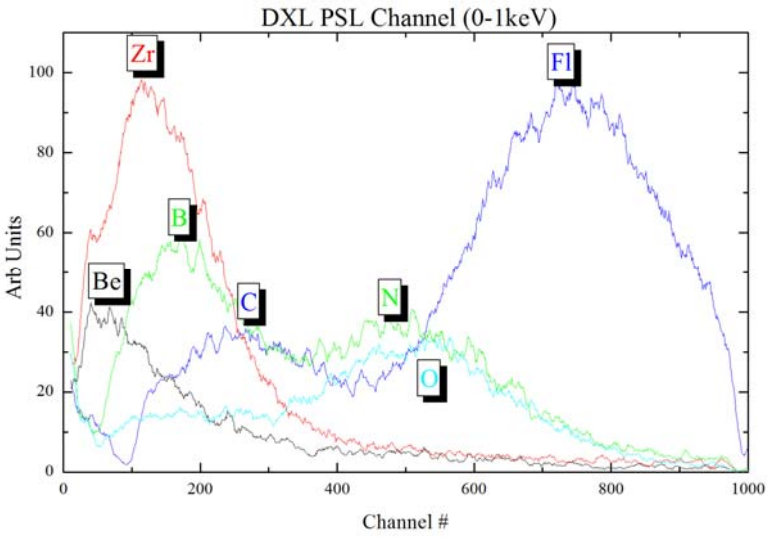

Figure 3.22: Sample peaks of calibration X-ray lines in the LOW Channel

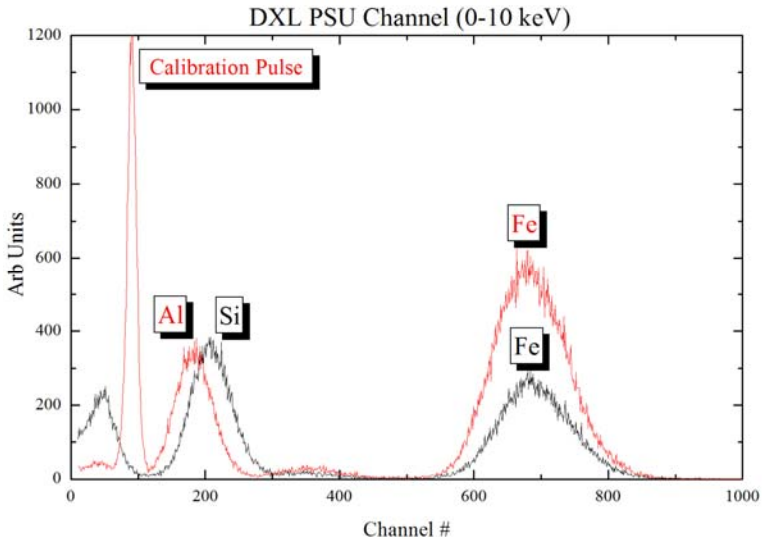

Figure 3.23: Sample peaks of calibration X-ray lines (UP Channel), along with the internal pulser signal around channel #100

Figure 3.22 and Figure 3.23 show the calibration lines in the two channels. The energy lines have been labeled. The shapes and heights are different for these lines since the exposure time varies. A peak from internal calibration pulse is shown in Figure 3.23. Note that I do not show the calibration pulse in the lower channel since the data I used to generate the plot were all taken when calibration was done without turning on the calibration solenoid.

Using Gaussian fits to the data, we obtained the peak positions of all the relevant lines. The position of the internal iron source is used to adjust for gain changes. The internal pulser positions are used to calculate the offsets in each line. The final peak positions of each line are plotted against the energy to obtain the non-linearity of the detectors. Figure

3.24 shows the DXL proportional counters' deviation from linearity. The calibration information is used to build and test a response function of DXL detectors.

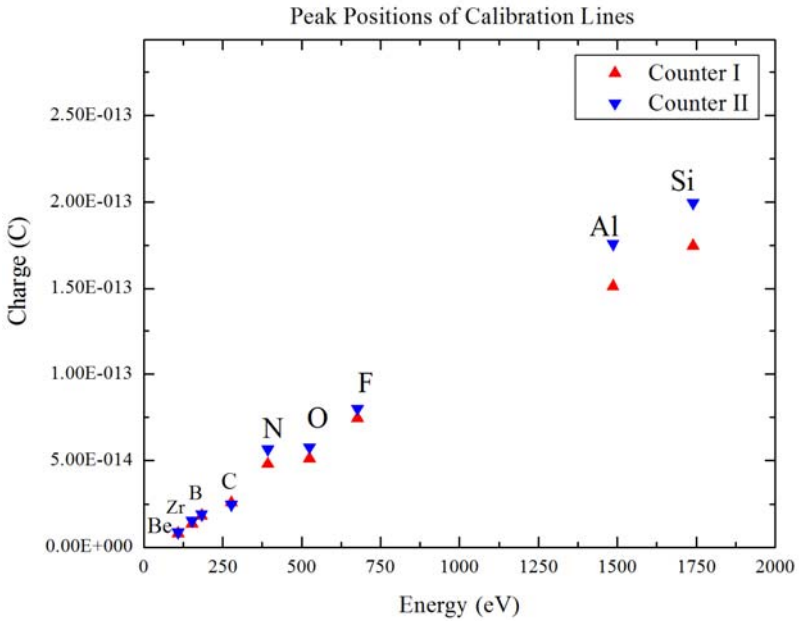

Figure 3.24: Charge generated from the calibration peaks as a function of their energy

3.12 Response Function

Building detector response is vital in astrophysical instrumentation, and are critical for testing models to data, especially data from low resolution detectors. DXL response functions were built into two separate files, a Redistribution Matrix File (RMF) and an Auxiliary Response file (ARF). RMF is basically a matrix that contains the spread of the counts from the detectors due to inherent resolution capabilities. While ideal detectors have diagonal elements, proportional counters have widely spread out matrices due to low

resolution. RMF contains the pulse height distributions, non-linearity, gas gain and any offsets determined from calibrations. A pre-defined model can be folded through a RMF to obtain counts directly comparable to the observed counts from a detector. Such comparison enables adjustment to input models until they deviate the least from the actual observations. We built response functions for both DXL counters based on the Jahoda and McCammon [94], and our calibration results discussed in section 3.11. We reduced the calibration data to derive the following set of input parameters (Table 3.5) to best characterize the DXL detectors.

Parameter	Unit	CI	CII
μ_{LOW}	-	$(2.56\text{-}3.55\times10^{-4}\times E)10^4$	$(2.81\text{-}3.29\times10^{-4}\times E)10^4$
μ_{UP}	-	$(0.91\times Exp[-E/1601.48]+1.69)10^4$	$(0.71\times Exp[-E/1226.48]+2.14)10^4$
h	-	1.4	1.4
W	eV	29	29
f'	-	0.175	0.175
D/w	μm	15	15
λ	μm	See section 3.9	See section 3.9
Note:		*E=Energy*	*E=Energy*

Table 3.5: Values of the DXL response parameters. See section 3.1 for the definitions of the listed terms

We verified that using the best fit parameters obtained from the calibrations, the charge vs energy output of our routine (dotted lines) successfully traced the calibration data (triangles) shown in Figure 3.25. However, the nitrogen data is offset closer to the oxygen response. We suspected that the boron nitride wafer used was contaminated with oxygen, but we didn't find oxygen peaks in X-ray diffraction.

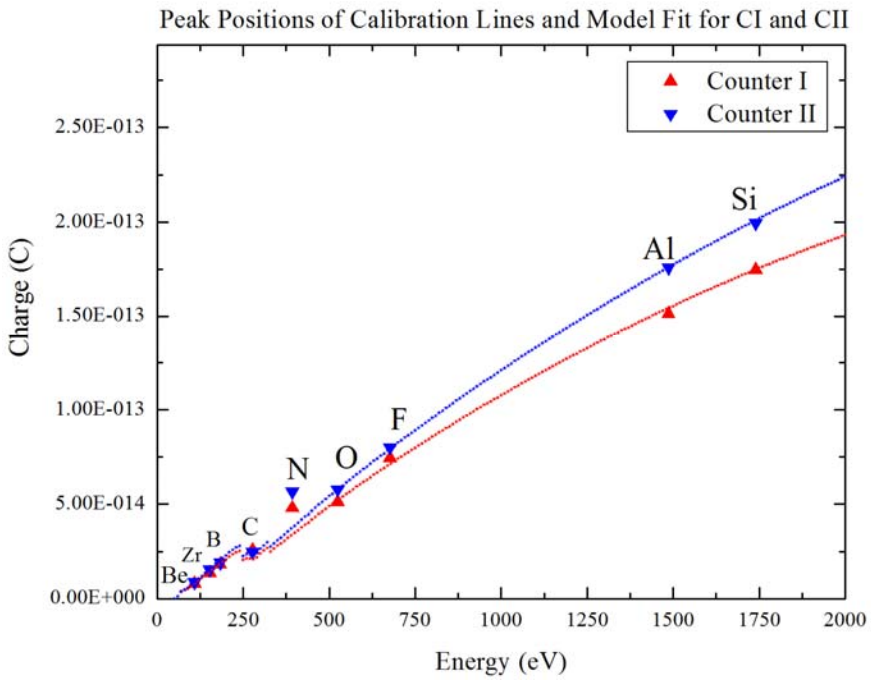

Figure 3.25: Charge calculated from energies of the calibration lines, both experimentally (triangles) and from response function routine (solid lines)

We also built a separate ARF file. An ARF file contains the information on the detectors ability to intercept photons. It includes the response of the windows and collimators to X-rays, the open area of the detectors, and the transmission of the mesh. A single column ARF file is obtained by simply multiplying the open area of the detector with the responses of the windows, mesh and collimator as a function of energy. The unit turns out as cm^2-sr, where the sr-the solid angle unit, comes from the collimator response as discussed in the section 3.4. The area to solid angle product is called the "grasp" of the detector (Figure 3.26). DXL has significantly higher grasp than other current or future missions, making it an ideal instrument to study the spatial variation of heliospheric SWCX [38].

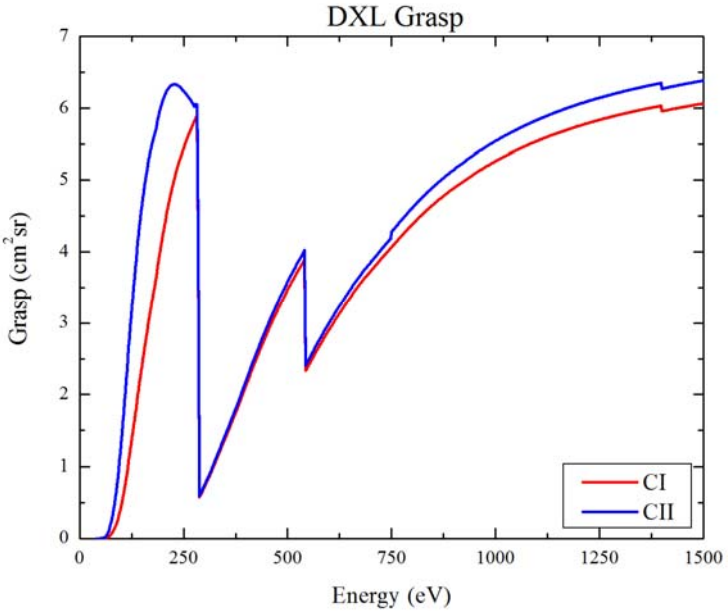

Figure 3.26: DXL grasp as a function of energy

3.13 ROSAT Equivalent Response Bands

To facilitate comparison with ROSAT in a band by band basis, we generated six DXL bands similar to ROSAT R1, R2, R4, R5, R6 and R7 bands. See Table 3.6 for DXL band definitions. Note that the channels below 111 were empty in the RMF matrix for the LOW channel of CI, hence we do not have the range for D0. Also note that the bands D0 through D4 are defined from the LOW channel while the rest come from the UP channel.

Band Name	Pulse Stretcher	Channel Range (CI)	Channel Range (CII)
D0	LOW	NA	10-149
D1	LOW	150-240	150-240
D2	LOW	241-350	241-350
D4	LOW	600-900	600-900
D5	UP	95-135	70-104
D6	UP	136-180	105-140
D7	UP	181-250	141-200

Table 3.6: DXL band definitions

The RMF and ARF file are used to generate the band-by-band grasps for DXL. The limits were chosen by trial to find the best match with the bands defined for ROSAT.

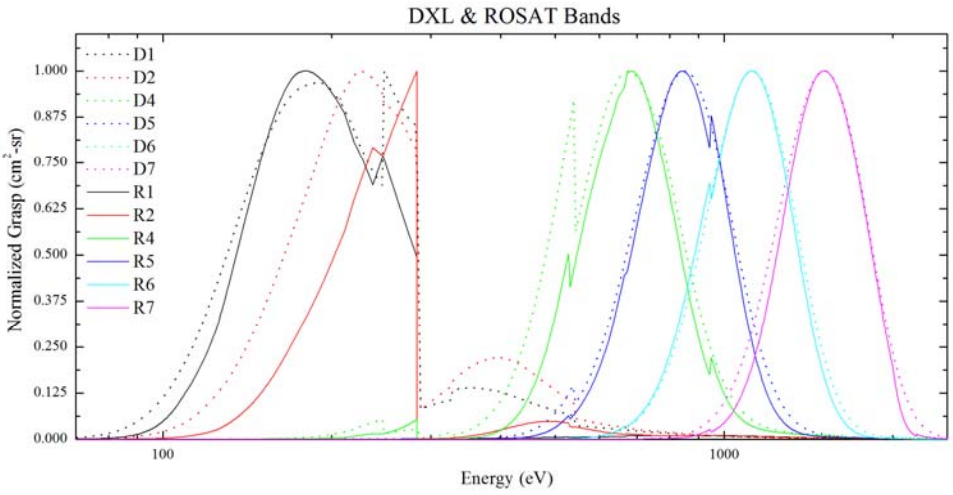

Figure 3.27: Normalized DXL bands D1 through D7 in close match with ROSAT bands. The apparent mismatch for D2 bands is just a normalization effect

Figure 3.27 shows the close similarity of DXL and ROSAT bands (solid lines for DXL and dotted lines for ROSAT). Since ROSAT defines R12, R45 and R67 bands as ¼, ¾ and 1.5 keV, DXL D12, D45 and D67 bands represent the same energy bands.

CHAPTER 4 **DATA REDUCTION AND ANALYSIS**

4.1 Data Reduction

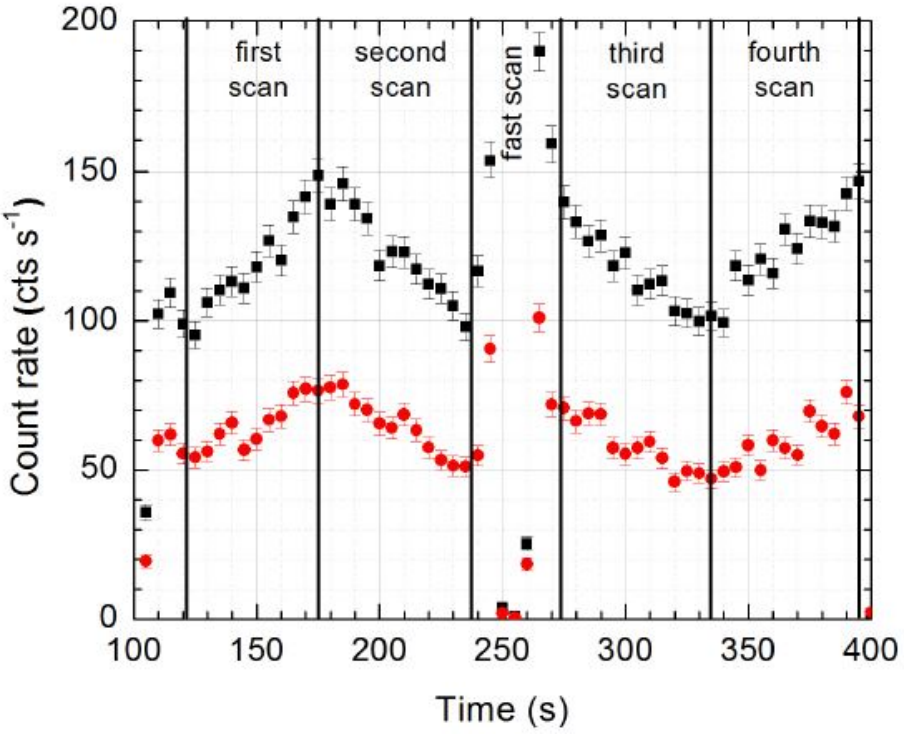

Figure 4.1: DXL count rate versus time [39]

The flight count rates vs time for CI (red) and CII (black) are shown in Figure 4.1 [39]. The observation started off the Helium Focusing Cone (HFC), moved towards the nose of the cone for a first scan and back for a second scan, then performed an Earth scan (fast scan) to measure the background. Then, the DXL returned to the nose of the cone, and performed a third scan off the cone, and went back to the nose for a fourth scan. The scan pattern is shown in Figure 4.2, especially the galactic longitude (blue line) showing the

scan in and out of the cone, and a 360^0 scan along time axis. A total of four slow scans along the cone, and 1 fast Earth scan were performed. The slow scan was done at 0.7 degrees per second, while fast scan moved by 10 degrees per second.

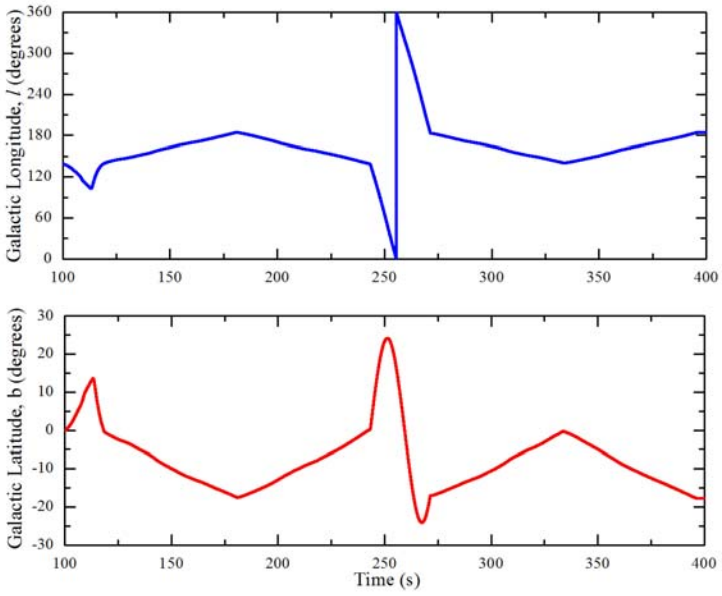

Figure 4.2: Galactic coordinates vs time for DXL flight plan

Flight data was provided by NASA on a CD-ROM in ASCII format organized according to TM Matrix. The TM data was also being fed into computer GSE during the flight for real-time visualization. The data consisted of 16 columns and 2089984 rows sampled every 0.2ms. Pulse stretcher data was extracted from the Matrix into the UP and LOW channels, and divided into calibration and science data. The histogram of the calibration data is shown in Figure 4.3. It shows the 4 internal pulser lines, 2 in each channel

per counter and 2 iron lines, one in each counter. Gaussian fits to the peaks were used to generate the peak positions.

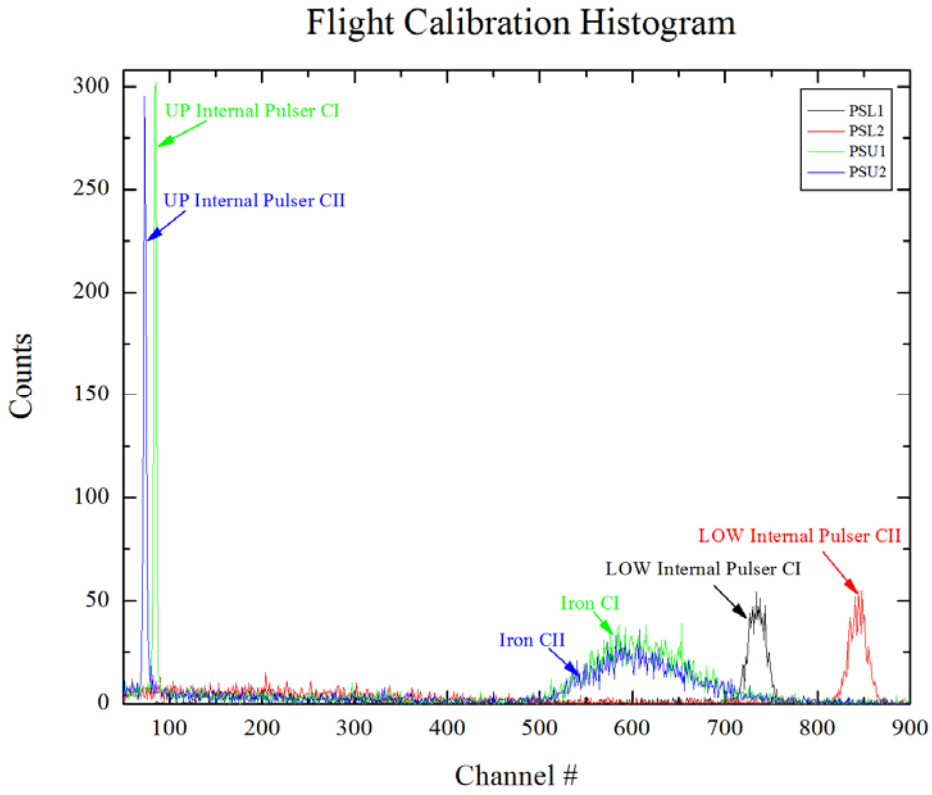

Figure 4.3: Histogram of the internal pulser and Fe-55 obtained for the flight data

Peak	CI		CII	
	Position	Sigma	Position	Sigma
PSL	734.73±0.13	9.52±0.13	843.72±0.28	9.74±0.32
PSU	84.53±0.03	1.35±0.03	73.45±0.05	1.35±0.06

Table 4.1: DXL flight pulser peak positions

As described in section 3.10.10, we calculated offsets of -8.893 for CI and -11.576 for CII from the pulser peak postions in Table 4.1. These offsets were added to the flight data.

We had an internal Fe-55 radioactive source exposed for ~1.5s every 30s during the flight to track any gain changes. An exponential decay fit of the form $y = y_0 + Ae^{-(x-x_0)/t}$ was fitted to the calibration data in the UP channel to calculate the gain changes.

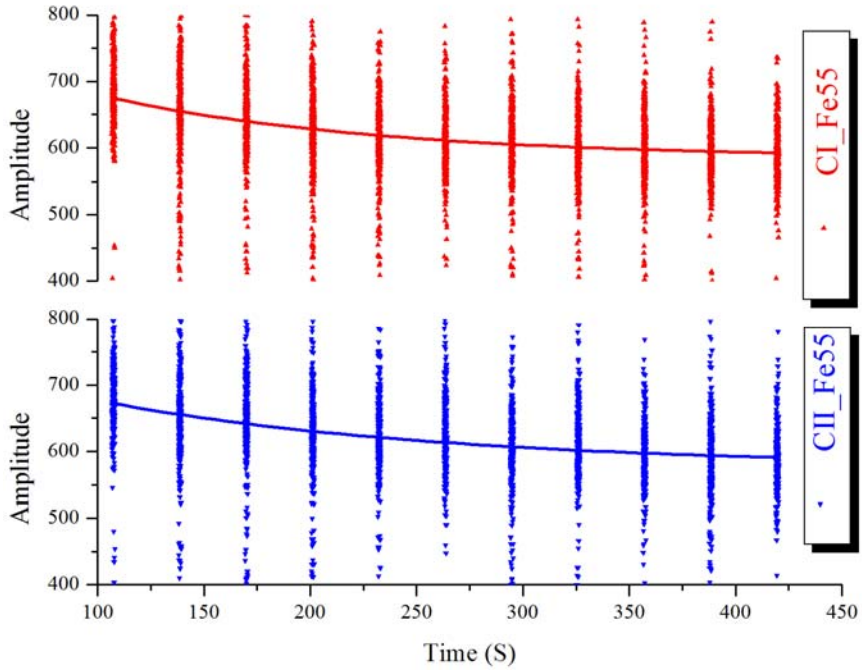

Figure 4.4: Gain drift of the flight data, with exponential decay fit shown as a solid line

Parameter	CI	CII
y_0	583.5±4.5	576.5±7.5
x_0	100±0	100±0
A	96.3±4	100.3±6.2
t	131.5±16.7	163.8±28.9

Table 4.2: DXL flight gain change fitting parameters

Having established the offset and gain drift, the flight data was normalized to have Fe-55 line centered at channel #700. Then we calculated the "nominal energy" by placing Fe-

55 line at 5900 eV. A histogram of the LOW channel in 1-1024 eV "nominal energy" bins is shown in Figure 4.5. The discriminator trigger level during the flight is also shown in the same figure.

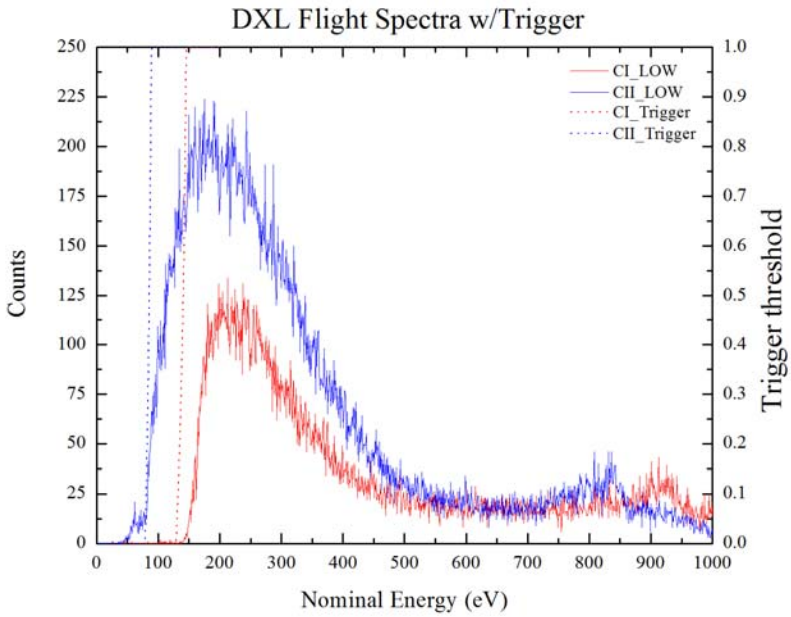

Figure 4.5: DXL flight spectra

We compared the flight DXL spectra with the APEC thermal emission model of ROSAT data. This model was folded through DXL response to obtain a model fit. The model to data fit is shown in Figure 4.6 where red (CI) and blue (CII) lines represent DXL spectra. The ROSAT model is shown in black line. The plot shows that the model folded through the DXL response function fits the data well.

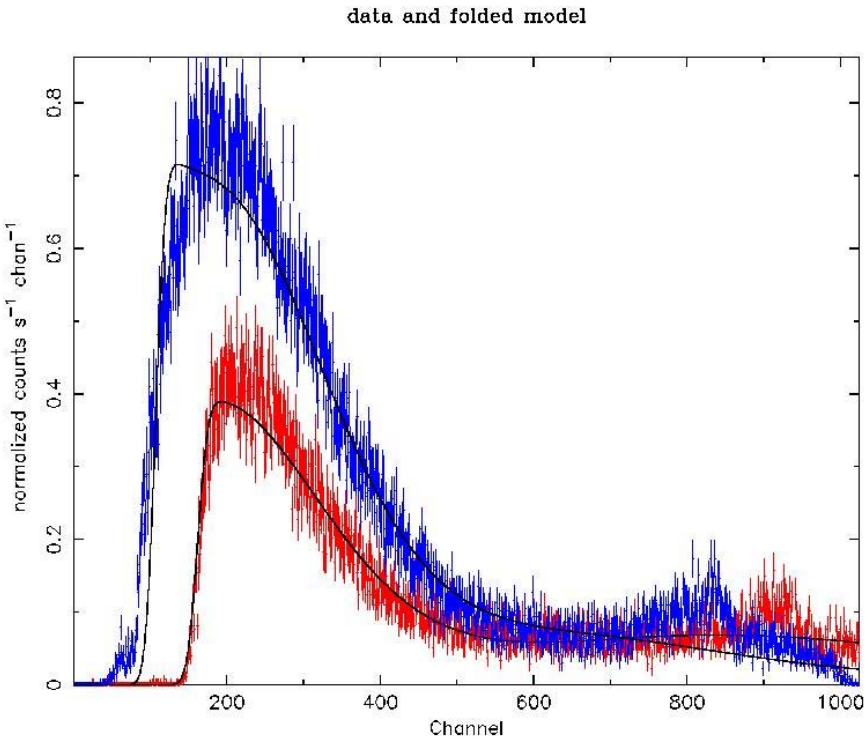

Figure 4.6: DXL spectra and the RASS model

Files containing information from atmospheric transmission, ACS and deadtime (both due to electronics chain and the internal pulser) are then combined by a FORTRAN routine to extract counts in a selected channel interval (defined by the DXL bands). A histogram generating routine then produces count rate in each band as a function of any chosen co-ordinates, along with errors defined by the square root of the number of events per interval of choice. We generated histograms for each DXL band in 1 eV and 5 eV intervals. We selected the 1 eV interval data in the slow scan region, while 5 eV data were present elsewhere to better fit the slow scan region.

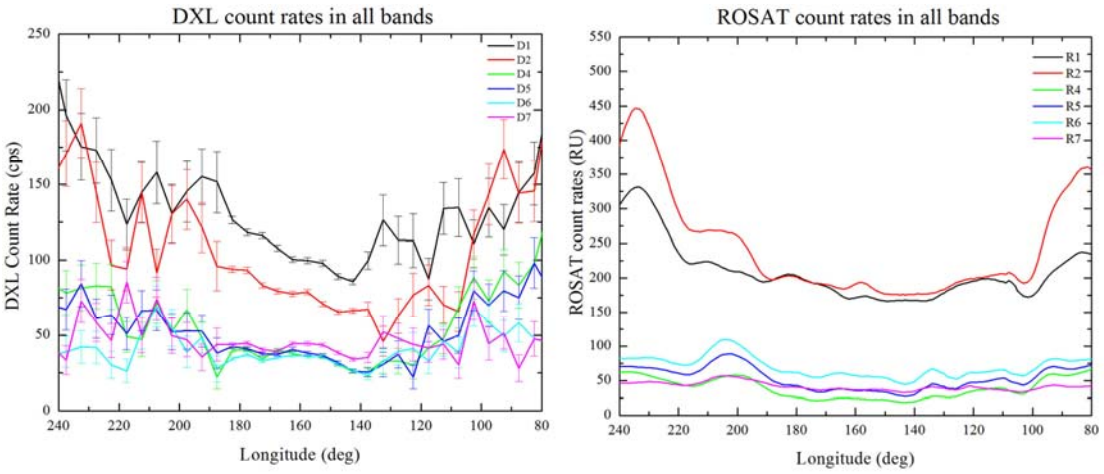

Figure 4.7: DXL and ROSAT count rates in all energy bands

We also extracted ROSAT data in the six bands for direct comparison with DXL. ROSAT rates were averaged over DXL collimators for the 0.1s aspect points, then binned into the standard set of longitude bins using weights from the livetimes and atmospheric transmissions given in those fields. The DXL and ROSAT count rates are shown in Figure 4.7.

The ROSAT rates shown in Figure 4.7 do not include the contributions from point sources. They were removed in the R12 rates to include only the diffuse emission. We extracted the point source contributions to each ROSAT band from the ROSAT bright and faint source catalogues. Point sources count rates were added to the ROSAT rates prior to data fitting to account for the contribution from the point sources in DXL.

4.2 Calculating SWCX Contribution

The premise for extracting SWCX information from DXL is that the DXL count rate exceeds the ROSAT count rate by an amount defined by the SWCX emission due to the HFC. Both DXL and ROSAT missions measure the combined emission of the LHB and the SWCX in the selected scan region, so that the total count rate (LHB+SWCX) in both missions are equal when weighted by respective instrument responses. We derive a proportionality between the DXL and ROSAT instrument responses, and use it in the global fitting to extract SWCX count rates in both DXL and ROSAT.

To calculate the count rate due to SWCX, a line of sight integral of the product of ion flux, neutral densities, summed product of partial cross sections for producing charge exchange and the efficiency are taken as shown in the equation below for helium and hydrogen:

$$Rate = \int \sum_i \sum_j n_i n_{He} v_{rel} \sigma_i b_{ij} g_j \, ds + \int \sum_i \sum_j n_i n_H v_{rel} \sigma_i b_{ij} g_j \, ds \qquad 4.1$$

where *i* and j are the solar wind species and the emission lines for the species respectively, σ_i are the speed-dependent interaction cross sections for individual species, b_{ij} is the line branching ratio, g_j is the instrument's response to line *j*, and v_{rel} is the relative speed between solar wind and neutral flow (both the bulk and thermal velocity). With ion density

n_i in terms of the proton density n_p at $R_0 = 1\ AU$, assuming that it scales as one over the square of the distance R from the Sun and the solar wind ion neutralizations effects are minimal (which we verified), we can define the compound cross-section as [39]:

$$\alpha = \sum_i \sum_j \frac{n_i(R_0)}{n_p(R_0)} \sigma_i b_{ij} g_j \qquad 4.2$$

In the case of constant solar-wind conditions, the solar-wind flux can be removed from the integrals, and the total charge exchange rate with H and He can be written as:

$$Rate = n_P(R_o)\, v_{rel} \alpha_{He} \left(\int \frac{n_{He}}{R^2}\, ds + \frac{\alpha_H}{\alpha_{He}} \int \frac{n_H}{R^2}\, ds \right) \qquad 4.3$$

where $\int \frac{n}{R^2}\, ds$ is the integrated neutral column density along the line of sight, weighted by one over the distance from the Sun squared ($1/R^2$) to reflect the dilution of the solar wind as it flows outward. The assumption of isotropy of the ion flux included in the equation above is an approximation, because the flux is known to vary strongly on timescales of about a day. These fluctuations, however, are smoothed when averaging over the few-week transit time through the relevant interplanetary region in a very good agreement between four complete sky surveys performed years apart by different missions [7].

We verified that the neutralization effects on the solar wind ions are negligible due to charge exchange. Using the suggested 3×10^{-15} cm^2 cross section and a typical solar minimum and maximum neutral helium distribution towards the central direction of the cone, we find that the loss of ions due to charge exchange are minimal as seen in Figure 4.8.

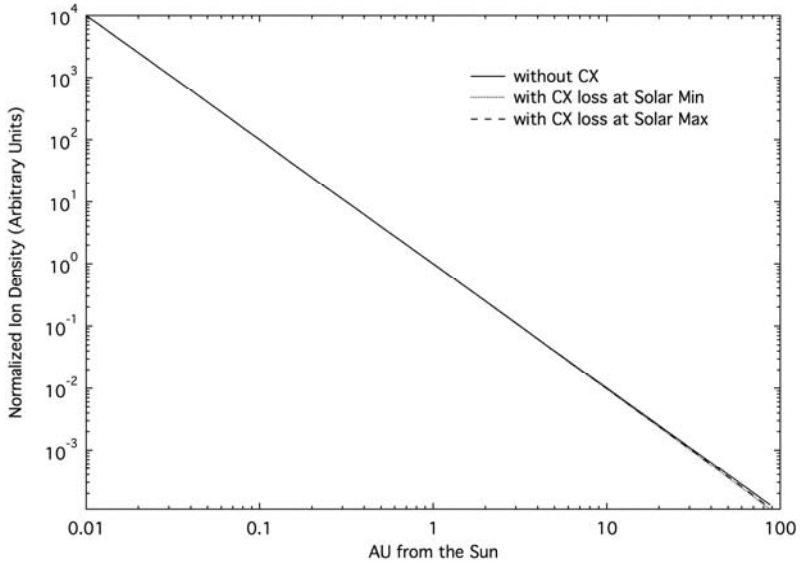

Figure 4.8: Normalized ion density as a function of distance from the Sun (D. Koutroumpa)

The density integrals for both H and He were calculated for each point along the DXL scan path from the expected neutral distributions due to the solar wind conditions for both DXL and ROSAT missions. The integrals above can be calculated with confidence for all lines of sight based on the calculations of the solar ionization conditions derived from measurements of backscattered solar radiation and checked by in-situ sampling [30].

To quantify the SWCX, we compared both DXL and ROSAT count rates to well determined models (Figure 4.9 and Figure 4.10) of the interplanetary neutral distribution along the lines of sight for both sets of measurements [30], [39], [103].

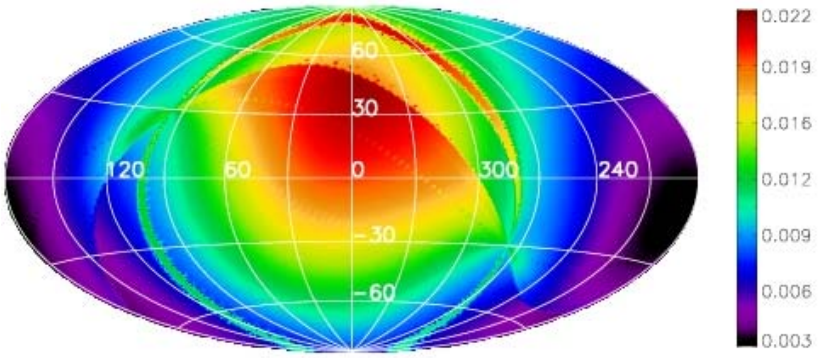

Figure 4.9: Interplanetary H density integrals for ROSAT geometry in units of $cm^{-3}AU^{-1}$) (Liu et al., in preparation)

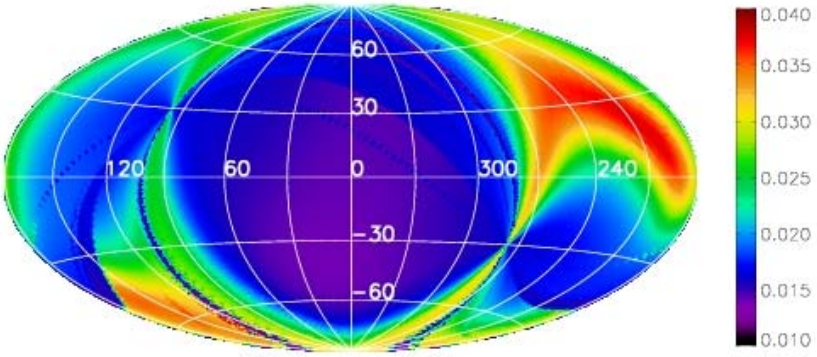

Figure 4.10: Interplanetary He density integrals for ROSAT geometry (units: $cm^{-3}AU^{-1}$) (Liu et al., in preparation)

Figure 4.11 shows the neutral column density distribution integrals for each line of sight along the scan path. The density distribution in the integrals is weighted by $1/R^2$,

where R is the distance from the Sun, since the solar wind dilutes as it flows away from the Sun. The red lines are the H (dashed) and He (solid) in the DXL geometry. The blue lines show the ROSAT H (dashed) and He (solid) integrals. DXL is significantly more affected by the HFC, while H contribution is small for both missions.

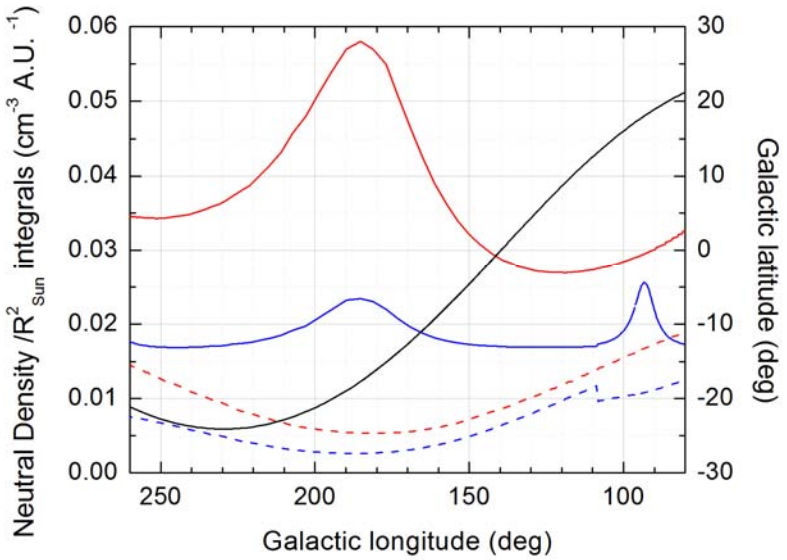

Figure 4.11: Weighted neutral atom column densities for DXL and ROSAT. The red (DXL) and blue (ROSAT) line shows neutral density along ROSAT line of sight. H (dotted lines) and He (solid lines) are shown for both DXL and ROSAT line of sight. Significantly enhanced He for DXL is due to the observational position of DXL in the HFC. The black solid line shows the Galactic latitude [39]

4.2.1 D12 Band (1/4 keV)

We inspected the ratio of DXL rate to ROSAT R12 rate as a function of R2/R1 averaged over several thermal model and abundances, and found quite independent of the models or

abundances. The ratio is necessary to normalize ROSAT and DXL responses in the global fitting to calculate SWCX. We used ROSAT maps[4] for a target at l=170^0, b=-10^0 to extract the count rate in the DXL slow scan region. We then fit the data using an unabsorbed thermal plus absorbed thermal and power law components. For the unabsorbed component, we tested the APEC, MEKAL and Raymond-Smith thermal models[5], and Savage & Sembach and Anders & Grevesse abundance models. The fit was done with different temperatures for the unabsorbed component in order to cover the observed range of the ROSAT R2/R1 ratio (spanning from 1.0-1.5). We evaluated the neutral hydrogen column density value, required to model the absorption coefficient, using the Infrared Astronomy Satellite (IRAS) 100 μm data. We used the absorbed thermal model (representing the Galactic Halo) with a temperature of 0.397 keV and a normalization of 5.967E-6 obtained from a fit of ROSAT rates at the target l=170^0, b=-10^0 with the APEC thermal model. In order to include the contribution of unresolved point sources, we used a power law with photon index fixed at 1.4 [34], [104]. Finally we folded the best fit model through DXL response to calculate the count rate in the DXL bands. The DXL to ROSAT count rates for ¼ keV band are plotted against the observed R2/R1 ratios (Figure 4.12). The best fit data is then used in the global fitting routine to correlate ROSAT to DXL observed rates.

[4] http://skyview.gsfc.nasa.gov/current/cgi/titlepage.pl
[5] https://heasarc.gsfc.nasa.gov/xanadu/xspec/manual/XspecModels.html

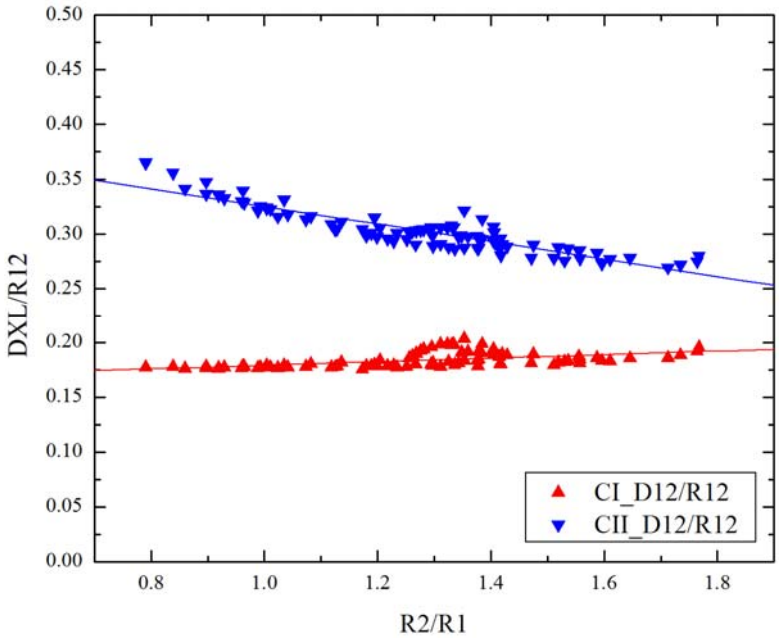

Figure 4.12: DXL/ROSAT rate vs R2/R1 ratio for ¼ keV band. The DXL rates were calculated by folding various thermal and abundances models for a wide range of temperatures of the unabsorbed component (to cover the widest range of ROSAT R2/R1 ratio) into DXL response. The temperature and normalization of the absorbed component, and the photon index and normalization of the power law were fixed to the best fit values obtained by fitting ROSAT data at the center of the slow scan region

For the fit of DXL data in D12 band with ROSAT data in R12 band, we took the combination $n_P(R_o)\, v_{rel}\alpha_{He}$, the ratio of solar wind fluxes for the two missions $n_P(R_o)\, v_{rel}\alpha_{He_{DXL}}/n_P(R_o)\, v_{rel}\alpha_{He_{ROSAT}}$, and correction factors to fine-tune the calculated ratios of DXL counter response to the ROSAT ¼ keV response as free parameters. With DXL rates (cps), ROSAT rates (RU), neutral density distributions ($cm^{-3}AU^{-1}$) for both missions, and the distribution of CI/R12 and CII/R12, we did a global least-

squares fit for both DXL counter rates for each point along the scan path to obtain SWCX information.

The fitting is done with different assumptions of the geocoronal contribution to ROSAT and the ratio between hydrogen and helium compound cross sections. To account for a potential geocoronal contribution to ROSAT, the "GeoC" factor is included in the fitting. We fitted DXL D12 band data with a zero geocoronal contribution to R12, and re-fitted with 50 RU after current best estimate (Kuntz, K. et al., manuscript in preparation). There is insufficient variation in the hydrogen column densities to determine its effective cross section, so for the ratio of the cross-sections ($\frac{\alpha_H}{\alpha_{He}}$), we assumed ratios of one first, and two since some determinations show smaller cross sections for helium. A fit, for example, of DXL D12 band data to ROSAT R12 data is shown in Figure 4.13.

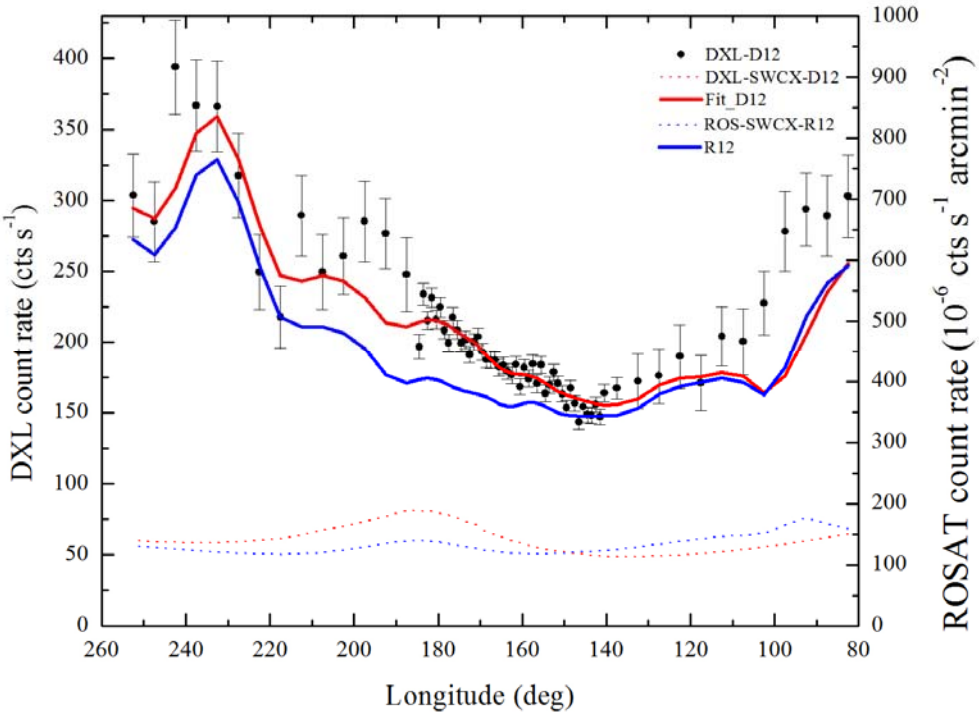

Figure 4.13: DXL & ROSAT fit in 1/4 keV band. The black dots are DXL data. Notice the error bars are smaller for slow scan region between ~140^0 to ~190^0 where we have higher statistics. The blue solid line is ROSAT count rate in RU. Red solid line represents the best fit curve of the DXL data. The SWCX contribution to DXL and ROSAT are shown in red and blue dotted lines respectively.

The best fit to the DXL count rates (red line), ROSAT rates (blue line) and combined CI and CII rates (black dots) plotted against the Galactic longitude in degrees are shown in Figure 4.13 corresponding to the condition 1 in Table 4.3. The figure also shows the contribution from SWCX to ROSAT and DXL bands. SWCX contributions to DXL and ROSAT are shown in red and blue dotted lines respectively. For each fit, we have 4 conditions:

a. *Condition 1:* $\frac{\alpha_H}{\alpha_{He}}$=1, Geocoronal contribution to ROSAT band =0 RU

b. *Condition 2:* $\frac{\alpha_H}{\alpha_{He}}$=1, Geocoronal contribution to ROSAT band =50 RU

c. *Condition 3:* $\frac{\alpha_H}{\alpha_{He}}$=2, Geocoronal contribution to ROSAT band =0 RU

d. *Condition 4:* $\frac{\alpha_H}{\alpha_{He}}$=2, Geocoronal contribution to ROSAT band =50 RU

Results of the global fit of DXL and ROSAT data for all four conditions are listed in Table 4.3.

Parameter	Condition 1	Condition 2	Condition 3	Condition 4
ci	0.90±0.06	0.94±0.06	0.86±0.07	0.91±0.07
cii	0.99±0.07	1.04±0.07	0.95±0.07	1.00±0.08
$n_P(R_o)\, v_{rel}\alpha_{He}$	5259.1±764	3051.8±721	4125.6±494	2711.5±465
$\frac{\alpha_H}{\alpha_{He}}$	1	1	2	2
Geocoronal SWCX contribution (RU)	0	50	0	50
DXL/ROSAT solar-wind flux	0.44±0.09	0.65±0.19	0.53±0.12	0.74±0.19
X^2*(136 d.o.f)*	225.77	215.08	224.47	213.29

Table 4.3: Summary of best fit parameters. The four conditions represent different assumptions of geocoronal contributions to ROSAT R12 band, and the ratio between H and He compound cross-sections α_H/α_{He}. *ci* and *cii* are the ratios of the fitted DXL response to the nominal value from laboratory calibrations for CI and CII.

From the data in the Table 4.3 (condition 1), ROSAT rate was calculated at 123.60±17.96 RU at the plane of the galaxy (l~140^0, b~0^0). Given R12 rate at the same location 346.6 RU, we find SWCX contribution to ROSAT R12 band at the plane to be

~36±5%. Across the whole sky, the average of neutral hydrogen, neutral helium for ROSAT and rate in R12 band were *0.0112 (cm^{-3} AU^{-1})*, *0.0208 (cm^{-3} AU^{-1})* and 617 RU respectively. The percentage of SWCX, then, was 27±4% on average. The calculated percentages for all 4 conditions are presented in the Table 4.4. The "In-plane" values are calculated at l~140^0. The SWCX contribution to ROSAT data in the ¼ keV band in the Galactic plane is consistently around ~36% for all conditions and are not affected by our assumption of 0 or 50 RU of the geocoronal component.

Condition	ROSAT SWCX (RU) In-plane	ROSAT SWCX (RU) All-sky average	In-plane SWCX (%)	All-sky SWCX (%)
1	124±18	168±24	36 ±5	27 ±4
2	122±29	148±35	35 ±8	24 ±4
3	124±15	178±21	36 ±4	29 ±3
4	131±23	167±29	38 ±7	27 ±3

Table 4.4: SWCX contributions in R12 band

Fitted plots of the DXL D12 band for all four conditions are shown in Figure 4.14.

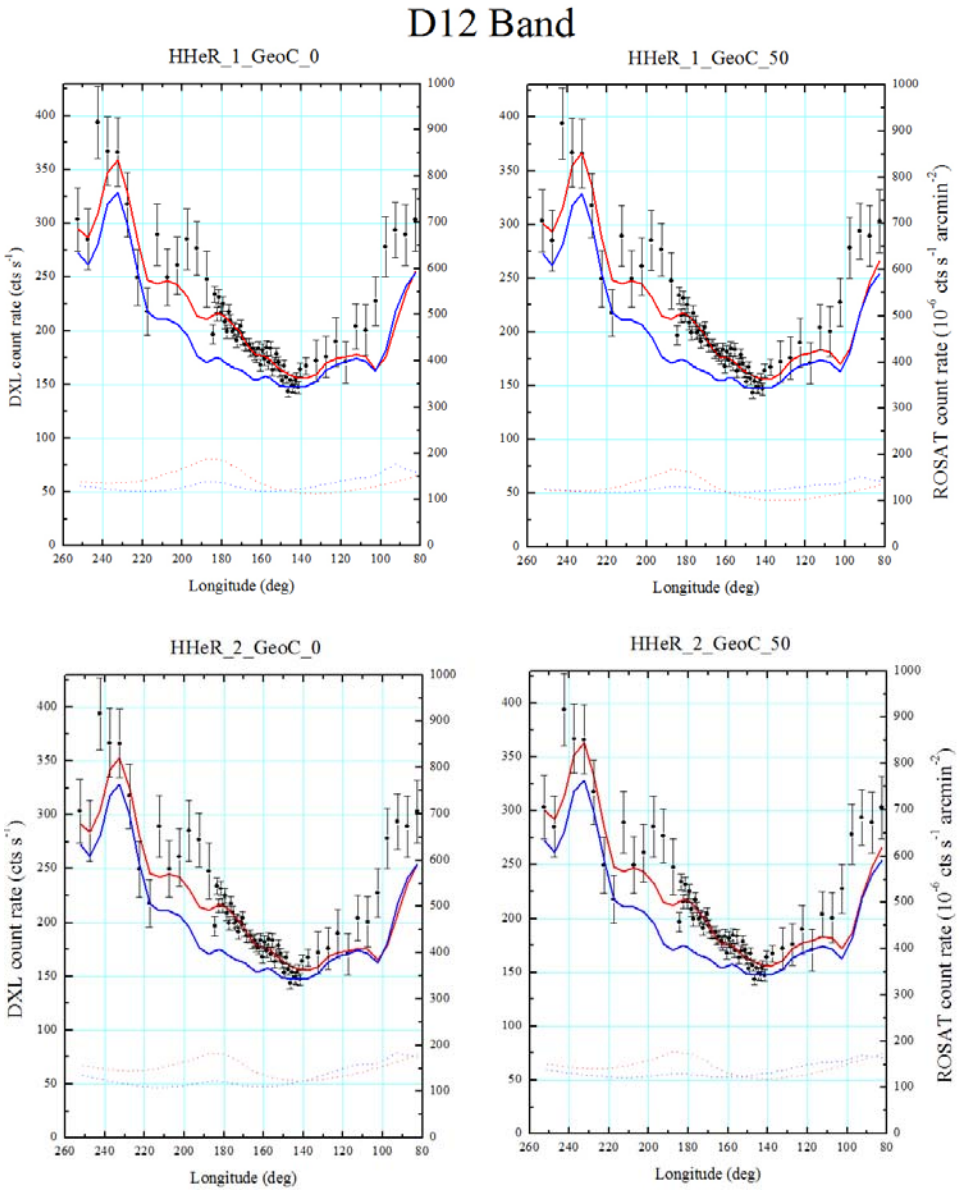

Figure 4.14: DXL & ROSAT fit in 1/4 keV band for 4 conditions. The blue solid line is ROSAT count rate in RU. Red solid line represents the best fit curve of the DXL data. The SWCX contribution to DXL and ROSAT are shown in red and blue dotted lines respectively.

From the neutral density maps of H and He, we calculated the SWCX emission and generated SWCX maps (based on condition 1) as seen in Figure 4.15.

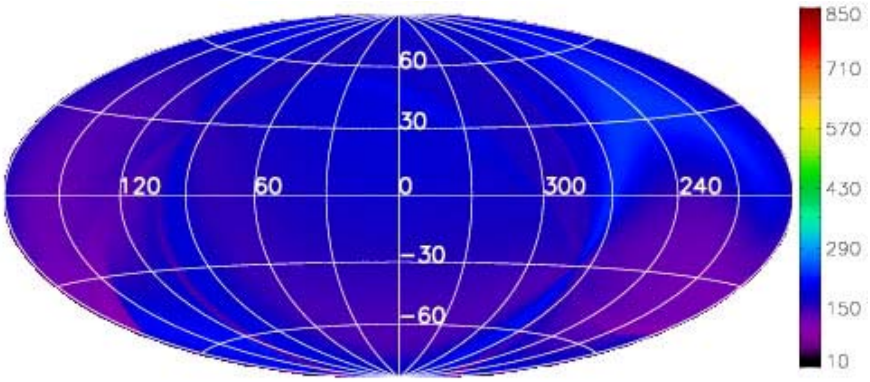

Figure 4.15: SWCX intensity in ROSAT ¼ keV band. The colorscale on the right denotes the count rate in RU (Liu et al., in preparation)

Subtracting the SWCX data point by point from the LHB map (Figure 1.2), we generated a new map (Figure 4.16) of the LHB, which represents only the emission from the hot plasma of the LHB.

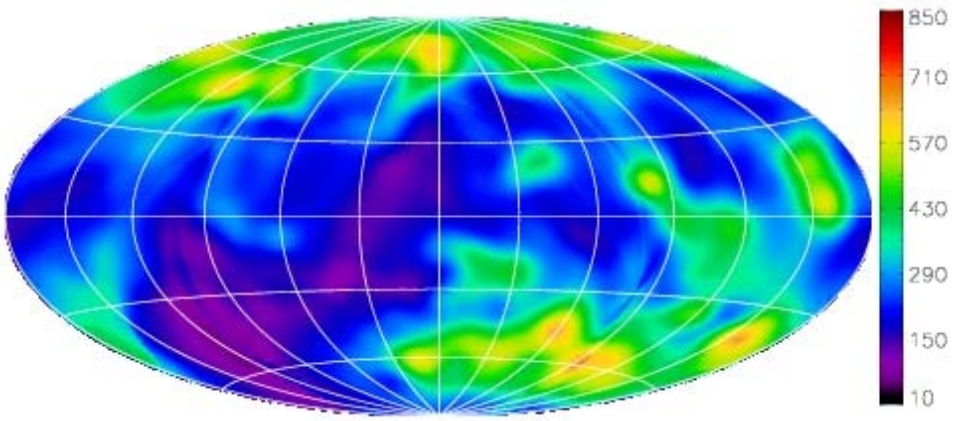

Figure 4.16: Corrected LHB map. Colorscale on the right indicates the count rate in RU (Liu et al., in preparation)

Using our results, Snowden et al., [63] subtracted the SWCX contribution from the RASS and re-evaluated the pressure equilibrium problem between the LHB and the Local Interstellar Clouds (LICs). They find the pressure of the LHB to be consistent with that of LICs, thereby removing the long-troubled pressure balance problem.

We also separated the SWCX contribution in the R1 and R2 bands individually, in the same four conditions as R12. The fittings of DXL data were performed in the same manner as the D12 band, albeit the geocoronal component used was 25 RU instead of 50 RU for each band (assuming it affects R1 and R2 bands equally). The four D1 band fittings, for four conditions, are shown in Figure 4.17 and the results of the fittings are shown in Table 4.5 and Table 4.6. The figures also show the contribution from SWCX to the ROSAT and DXL bands as red and blue dotted lines, respectively.

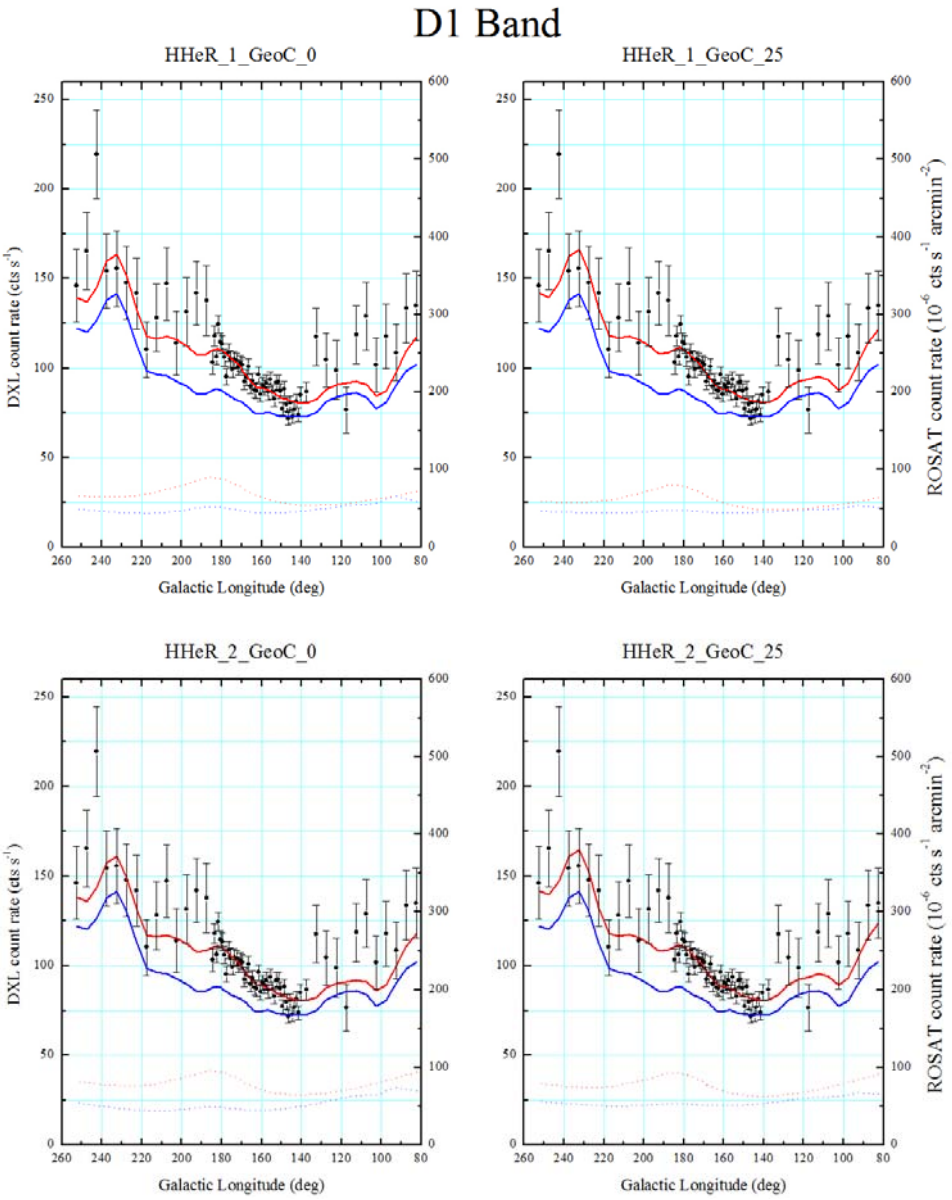

Figure 4.17: DXL & ROSAT fit in R1 band for 4 conditions. The blue solid line is ROSAT count rate in RU. Red solid line represents the best fit curve of the DXL data. The SWCX contribution to DXL and ROSAT are shown in red and blue dotted lines respectively.

Parameter	Condition 1	Condition 2	Condition 3	Condition 4
ci	0.81±0.09	0.84±0.10	0.77±0.10	0.81±0.10
cii	0.88±0.11	0.92±0.11	0.84±0.11	0.88±0.11
$n_P(R_o)\ v_{rel}\alpha_{He}$	1961±635	851.8±603	1657±393	954.4±371
$\frac{\alpha_H}{\alpha_{He}}$	1	1	2	2
Geocoronal SWCX contribution (RU)	0	25	0	25
DXL/ROSAT solar-wind flux	0.60±0.27	1.18±0.94	0.74±0.31	1.18±0.62
X^2(136 d.o.f)	187.79	185.04	186.91	184.12

Table 4.5: D1 band fit parameters

Again, the SWCX contribution to the ROSAT R1 band was calculated at 27±9% for condition 1 with R1 rate of 168.8 RU at the plane of the Galaxy. Across the whole sky, the average of neutral H, neutral He and R1 count rate were *0.0112 (cm^{-3} AU^{-1})*, *0.0208 (cm^{-3} AU^{-1})* and 268 RU, respectively. The percentage of SWCX, then, was 23±8% on average. Similar calculations for all four conditions of the fits are shown in Table 4.6.

Condition	ROSAT SWCX (RU) In-plane	ROSAT SWCX (RU) All-sky average	In-plane SWCX (%)	All-sky SWCX (%)
1	46±15	63±20	27 ±9	23 ±8
2	45±32	52±37	27 ±19	20 ±7
3	50±12	72±17	29 ±7	27 ±6
4	54±21	66±26	32 ±12	25 ±6

Table 4.6: SWCX contributions in R1 band

Based on the results above, we generated corrected LHB and SWCX maps in the R1 band (condition 1) shown in Figure 4.18 and Figure 4.19.

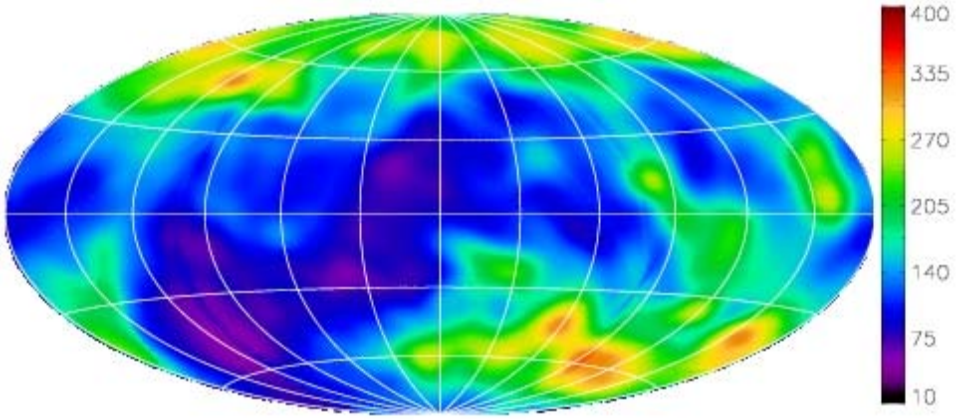

Figure 4.18: Corrected LHB map in R1 band. Colorscale on the right indicates the count rate in RU (Liu et al., in preparation)

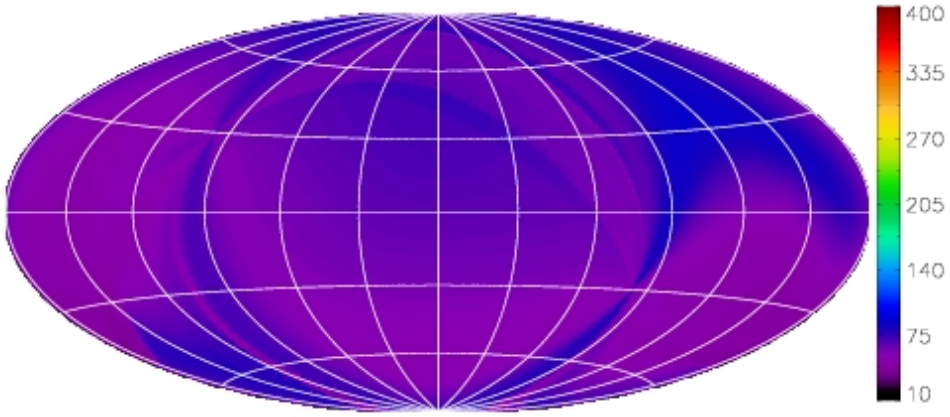

Figure 4.19: SWCX map (Band: R1) (Liu et al., in preparation)

The fittings from D2 bands are shown in Figure 4.20. The figures also show the contribution from SWCX to the ROSAT and the DXL bands as red and blue dotted lines, respectively. The results from the fitting of D2 band are listed in Table 4.7 and Table 4.8.

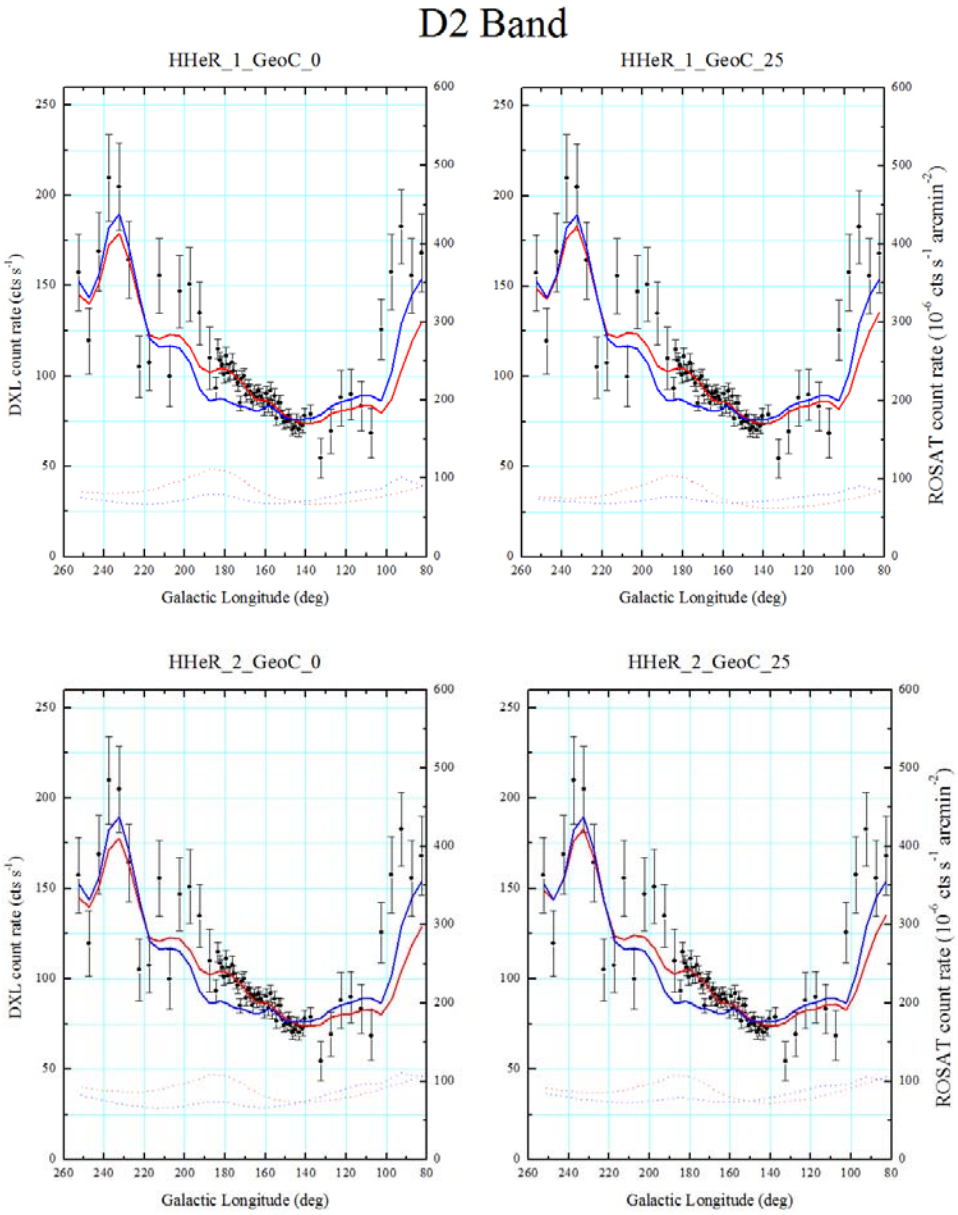

Figure 4.20: DXL & ROSAT fit in R2 band for 4 conditions. The blue solid line is ROSAT count rate in RU. Red solid line represents the best fit curve of the DXL data. The SWCX contribution to DXL and ROSAT are shown in red and blue dotted lines respectively.

Parameter	Condition 1	Condition 2	Condition 3	Condition 4
ci	0.83±0.08	0.87±0.08	0.82±0.08	0.86±0.08
cii	1.06±0.10	1.11±0.11	1.04±0.11	1.10±0.11
$n_P(R_o)\ v_{rel}\alpha_{He}$	3025±561	1970±528	2499±360	1810±341
$\frac{\alpha_H}{\alpha_{He}}$	1	1	2	2
Geocoronal SWCX contribution (RU)	0	25	0	25
DXL/ROSAT solar-wind flux	0.53±0.13	0.72±0.23	0.58±0.15	0.76±0.20
X^2*(136 d.o.f)*	187.67	181.83	186.83	180.96

Table 4.7: D2 band fit parameters

The SWCX contribution to ROSAT R2 band was calculated at 40±7% for condition 1 with R2 rate of 177.8 RU at the plane of the Galaxy. Across the whole sky, the average of *nH*, *nHe* and R2 were *0.0112 (cm^{-3} AU^{-1})*, *0.0208 (cm^{-3} AU^{-1})* and 350 RU respectively. The percentage of SWCX, then, was 28±5% on average. Similar calculations for all four conditions are shown in Table 4.8.

Condition	ROSAT SWCX (RU) In-plane	ROSAT SWCX (RU) All-sky average	In-plane SWCX (%)	All-Sky SWCX (%)
1	71±13	97±18	40 ±7	28 ±5
2	71±19	88±24	40 ±11	25 ±5
3	75±11	108±16	42 ±6	31 ±4
4	79±15	103±19	45 ±8	29 ±4

Table 4.8: SWCX contributions in R2 band

Based on the results above, we generated corrected LHB and SWCX maps in the R2 band (condition 1) shown in Figure 4.21 and Figure 4.22.

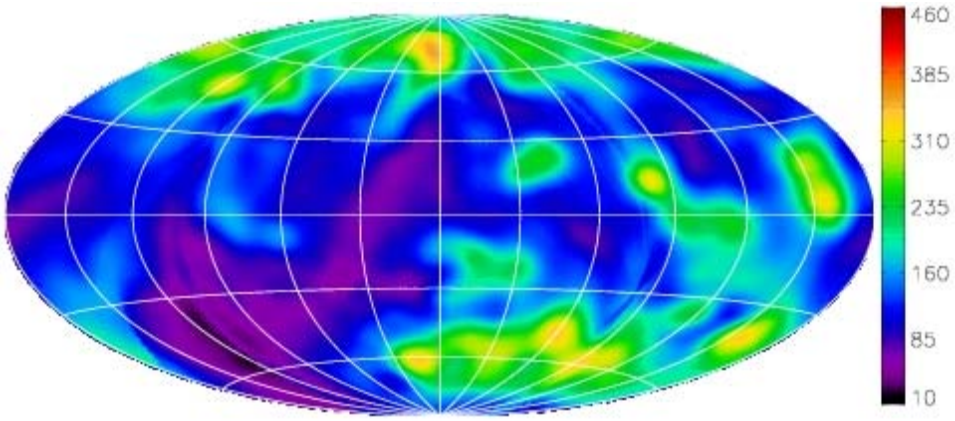

Figure 4.21: Corrected LHB map (Band: R2) (Liu et al., in preparation)

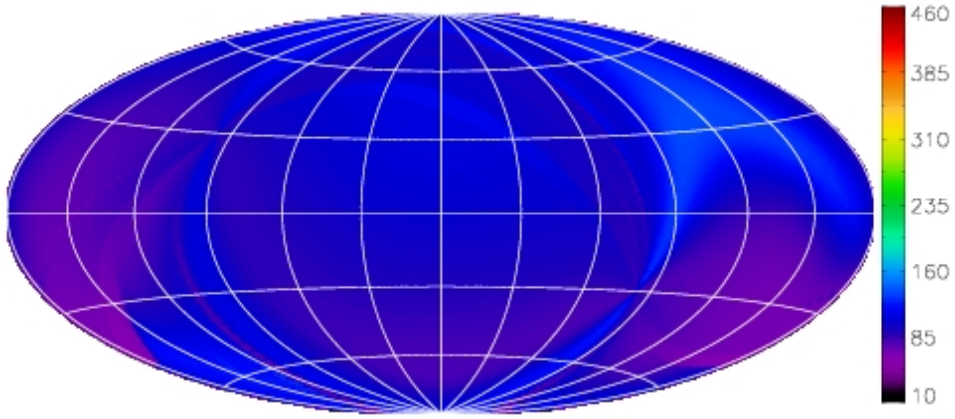

Figure 4.22: SWCX map (Band: R2) (Liu et al., in preparation)

4.2.2 D45 Band (3/4 KeV)

The global fitting of DXL and ROSAT data in this band generated a set of parameters tabulated in Table 4.9 and Table 4.10. Note that we didn't have any reasonable data to estimate the geocoronal SWCX contribution to ROSAT in this band. We set it to zero

throughout the fits. Thus the global fits were done under two conditions, 1 and 2, for $\frac{\alpha_H}{\alpha_{He}} = 1$ and $\frac{\alpha_H}{\alpha_{He}} = 2$ respectively, and are shown in Figure 3.23 for D45 band.

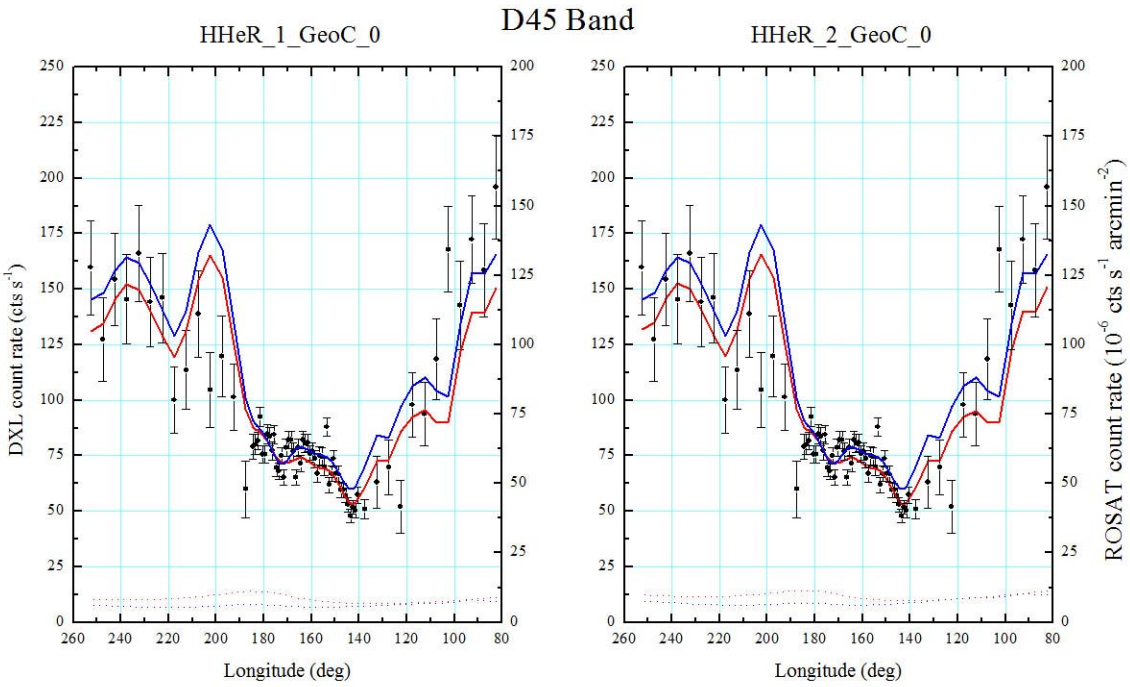

Figure 4.23: DXL & ROSAT fit in ¾ keV band for 4 conditions. The blue solid line is ROSAT count rate in RU. Red solid line represents the best fit curve of the DXL data. The SWCX contribution to DXL and ROSAT are shown in red and blue dotted lines respectively.

Similarly, the D4 and D5 bands were fitted separately for $\frac{\alpha_H}{\alpha_{He}}$ as either 1 or 2. The results from the fits in D45 band are listed in Table 4.9.

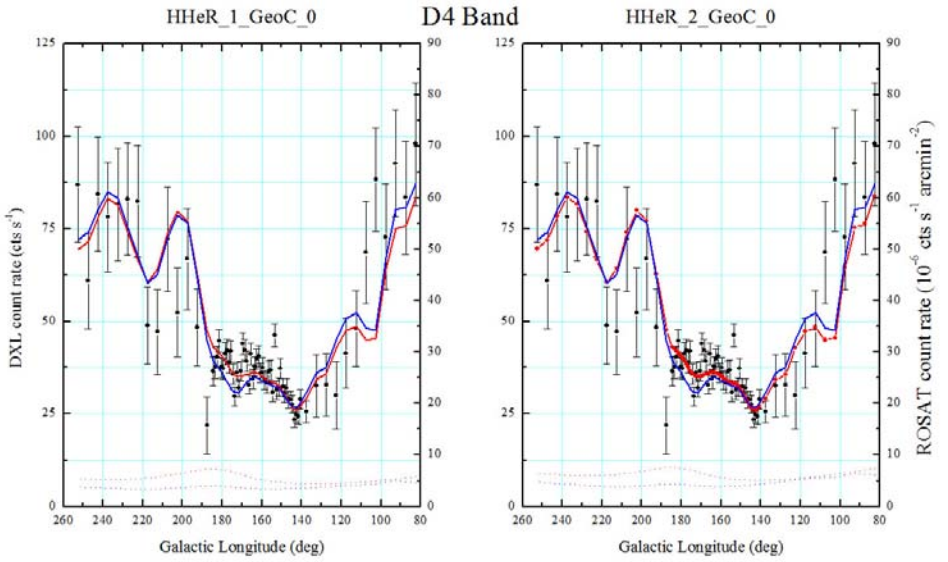

Figure 4.24: DXL & ROSAT fit in R4 band

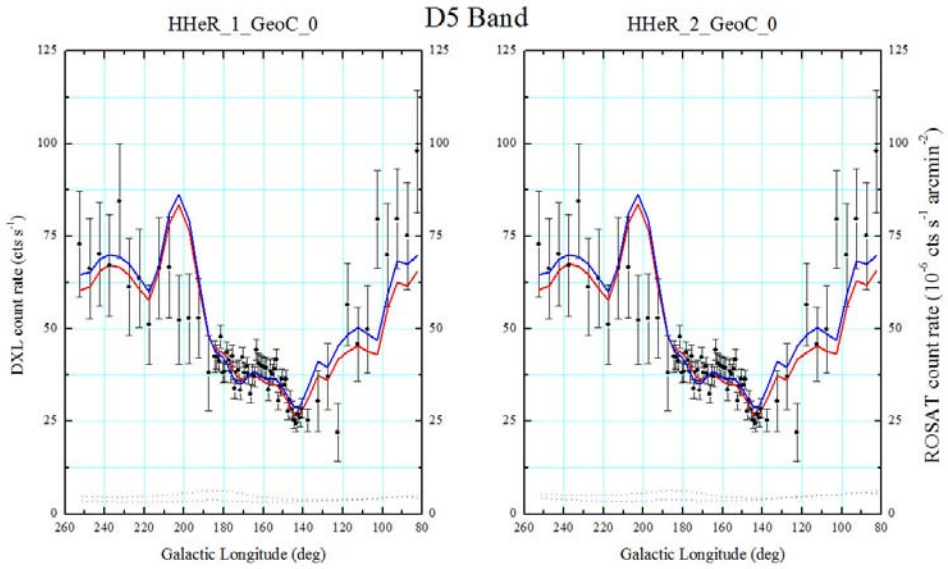

Figure 4.25: DXL & ROSAT fit in R5 band

	D4		D5		D45	
	Condition		Condition		Condition	
Parameters	1	2	1	2	1	2
ci	0.99±0.08	0.99±0.08	1.09±0.09	1.09±0.10	1.07±0.06	1.07±0.06
cii	1.19±0.09	1.19±0.09	0.96±0.08	0.96±0.08	1.08±0.06	1.08±0.06
$n_P(R_o)\, v_{rel}\alpha_{He}$	152±102	146±75	141±146	131±107	244±171	233±125
$\frac{\alpha_H}{\alpha_{He}}$	1	2	1	2	1	2
Geocoronal SWCX contribution (RU)	0	0	0	0	0	0
DXL/ROSAT solar-wind flux	0.74±0.38	0.74±0.30	0.74±0.63	0.74±0.51	0.74±0.40	0.74±0.32
X^2*(136 d.o.f)*	239.38	239.39	222.43	222.55	361.36	361.41

Table 4.9: D45 band fit parameters

The SWCX contribution to the ROSAT R4 band was calculated at 11±8% for condition 1 with R45 rate of 50.79 RU at the plane of the Galaxy. Averaging across the whole sky (using average of neutral H, neutral He and R4 were *0.0112 (cm^{-3} AU^{-1})*, *0.0208 (cm^{-3} AU^{-1})* and 155.2 RU respectively), and both fitting conditions, we find that the SWCX contributes 9±5% to the ¾ keV band. Note that R4 and R5 rates are 20.27 RU and 30.52 RU at the plane, while they average at 67.6 RU and 87.6 RU across the whole sky. The SWCX contributions to ROSAT R4, R5 and combined R45 bands are listed in Table 4.10.

Band	Conditions	ROSAT SWCX (RU) In-plane	ROSAT SWCX (RU) All-sky	SWCX (%)	
				In-plane	All-sky
D4	1	3.6±2.4	5±3	18±12	5±3
	2	4.4±2.2	6±3	22±11	6±5
D5	1	3.3±3.4	5±5	11±11	5±5
	2	4.4±3.6	6±5	14±12	6±5
D45	1	5.7±4.0	8±5	11±8	8±5
	2	7.0±3.7	10±5	14±7	10±5

Table 4.10: SWCX contributions in R45 band

We calculated the SWCX contributions across the sky for R45 band and generated a map (condition 1) which is shown in Figure 4.26.

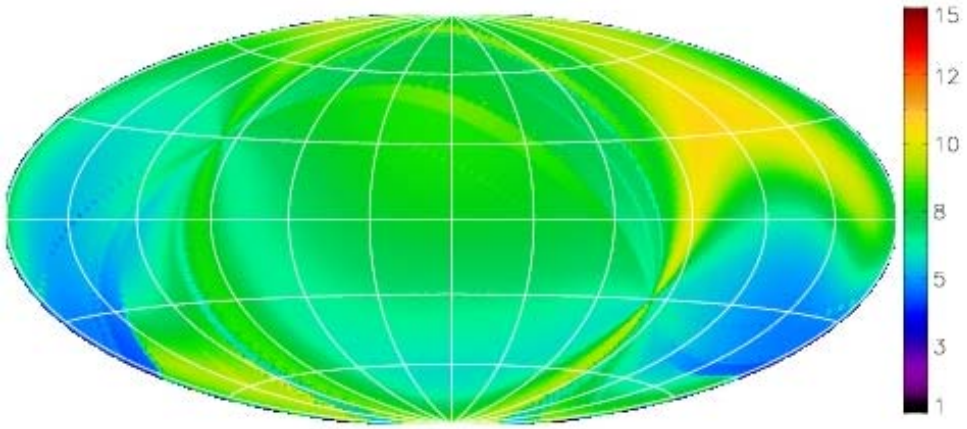

Figure 4.26: SWCX map (Band: R45) (Liu et al., in preparation)

We calculated an average SWCX count rate of 9.1±5.55 RU for $|b|>30^0$ (Off-plane) and 9.5±5.8 RU for $|b|<30^0$ (In-plane) in the R45 band. We faked a ROSAT spectrum based on the SWCX count rate in the R4 and R5 bands and fitted with "The AtomDB Charge

Exchange (ACX)" model [105] in XSPEC with temperature and normalization as free parameters. We found the OVII/OVIII ratio of 1.28 for both In- and Off-plane emission. Using ROSAT effective areas of 36.05cm^2 and 76.6 cm^2 for OVII and OVIII, we calculated that 1 LU=3.05 RU (OVII) and 1 LU=6.48 RU (OVIII). Hence, from the ratio of OVII and OVIII, and LU to RU conversion, we calculated that OVII contribution to R45 band is 1.12±0.68 LU in the plane and 1.17±0.71 off the plane. Similarly, OVIII contributes 0.88±0.53 LU towards the plane and 0.91±0.56 LU off the galactic plane.

We also looked at the LHB contribution to the R45 band. Based on the average temperature of 0.0847 keV of the LHB in the plane ($|b|<30^0$), and the emission measure of 1.83×10^{-3} cm^{-6} pc, we calculated that the LHB generates about 2 RU in the ¼ keV band from the unabsorbed component of the APEC model. The contribution of the LHB to the ¾ keV in the galactic plane is ~4%. With SWCX contributing only up to ~13% (condition 1 and 2 averaged), we can account for up to 17% of the emission in the plane of the galaxy, requiring some way of compensating for the rest of the emission in addition to the Halo, stellar emission and beyond.

4.2.3 D67 Band (1.5 keV)

Figure 4.27 shows the DXL and ROSAT rates plotted against the galactic longitude with fitting curves. We find that the SWCX emission in the 1/5 keV band is compatible with zero.

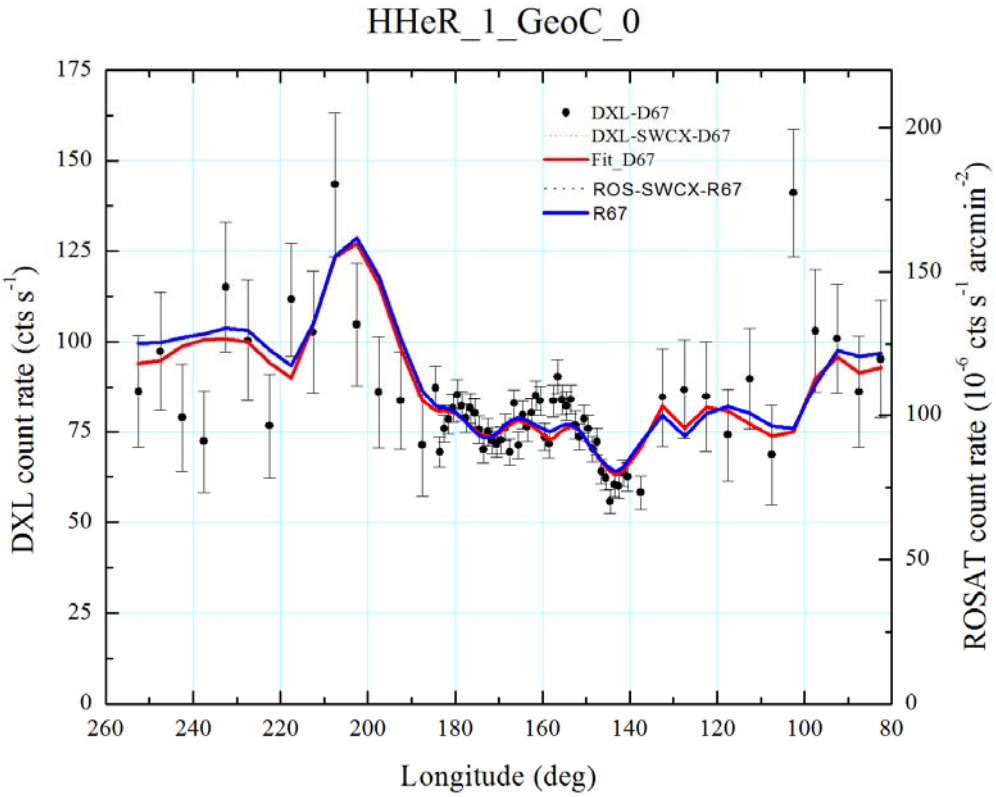

Figure 4.27: DXL & ROSAT fit in R67 band. The blue solid line is ROSAT count rate in RU. Red solid line represents the best fit curve of the DXL data.

CHAPTER 5 **CONCLUSIONS**

5.1 Results

Quantifying Solar Wind Charge Exchange (SWCX) X-ray emission, and separating it from the background was critical towards better modeling and understanding of the Interstellar Medium (ISM). The most accessible part of the ISM is the solar neighborhood, where an enhancement of helium neutrals due to focusing of the Sun's gravity into a Helium Focusing Cone (HFC) creates a region of excess X-ray emission by SWCX mechanism. The DXL (Diffuse X-ray Emission from the Local Galaxy) mission observed the excess X-ray emission during a sounding rocket experiment conducted in December 2012 when scanning a selected region of the sky through the HFC. The same region of the sky was scanned by the ROSAT satellite in September 1990 while 1 AU away and parallel to the HFC. A global least-squares fit of the two DXL counters' X-ray data was performed with the ROSAT data point by point along the DXL scan path, separately in each of the ROSAT bands.

We quantified the SWCX emission in the ¼ keV band as 36±5% towards the galactic plane with the count rate of 124±18 RU. All-sky averaged SWCX contribution to ROSAT is 168±25 RU, effectively 27±4%. We find that the emission from the LHB dominates in the ¼ keV band. Using the DXL results, Snowden et al. [39] find that the calculated LHB pressure adequately balances the thermal pressure and magnetic field pressure of the LICs for equilibrium, thereby eliminating the problem of pressure unbalance between the LHB

and the LICs [63]. In the ¾ keV band, SWCX contributions at the galactic plane is 13±11%. It contributes 8±5 RU (5.0±3.5%) when averaged across the whole sky. We calculated the OVII and OVIII line contributions in the ¾ keV band. We find that on the galactic plane ($|l| < 30^0$), OVII and OVIII contribute 1.12±0.68 LU and 0.88±0.53 LU respectively. For off-plane contributions ($|l| > 30^0$), we find OVII with 1.17±0.65 LU and OVIII with 0.91±0.51 LU.

In conclusion, we have established that the LHB exists and dominates the emission in the ¼ keV band. The total heliospheric and geocoronal SWCX contributions to the ¼ keV band is 36% at maximum. In the ¾ keV band, the SWCX emission is ~13%. SWCX and LHB combined can only account for ~17% of the emission observed in the galactic plane in the ¾ keV band, raising new questions on the origin of the ¾ keV emission.

APPENDIX A

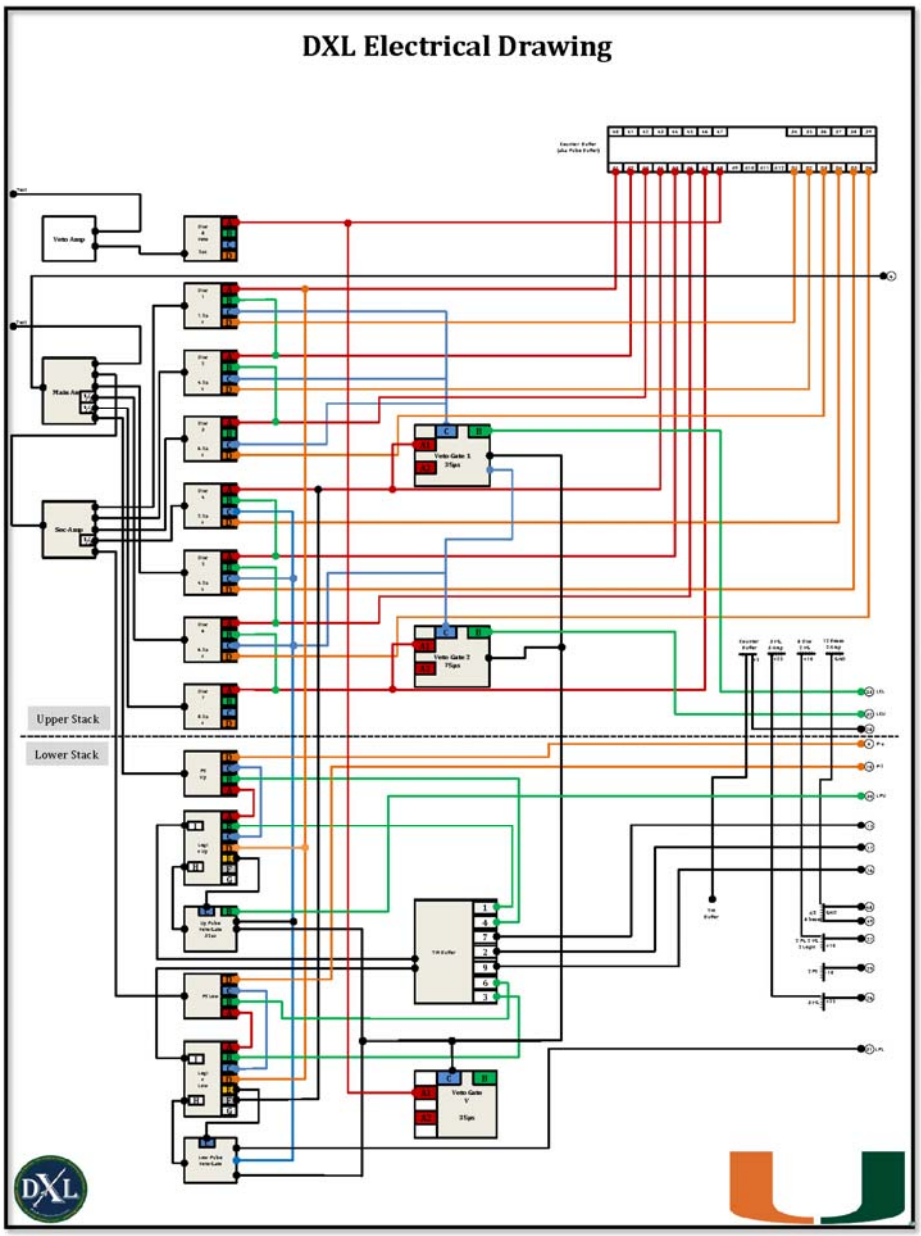

Figure A.1: DXL Electronics Schematic

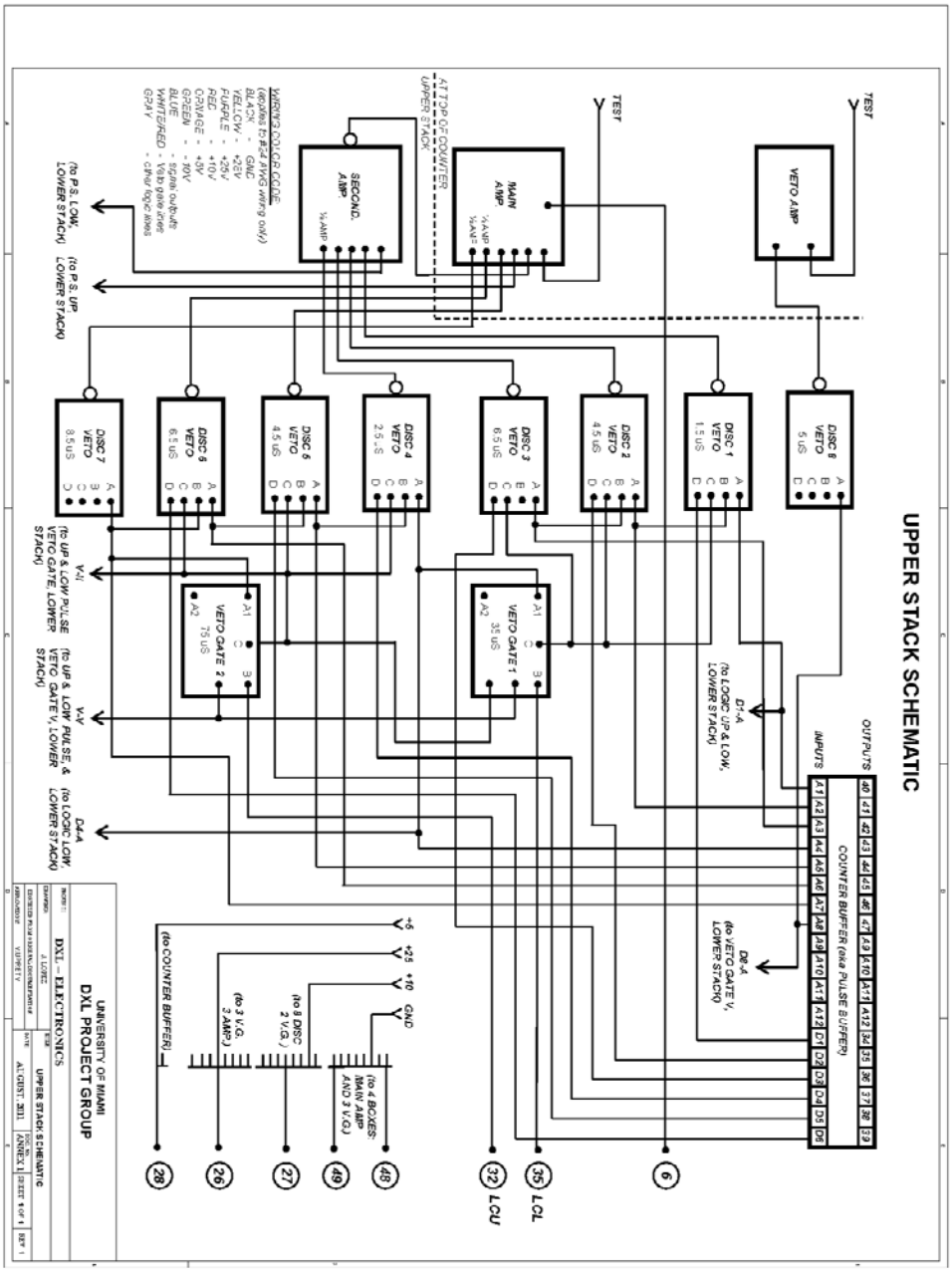

Figure A.2: Upper Stack Electronics Schematic

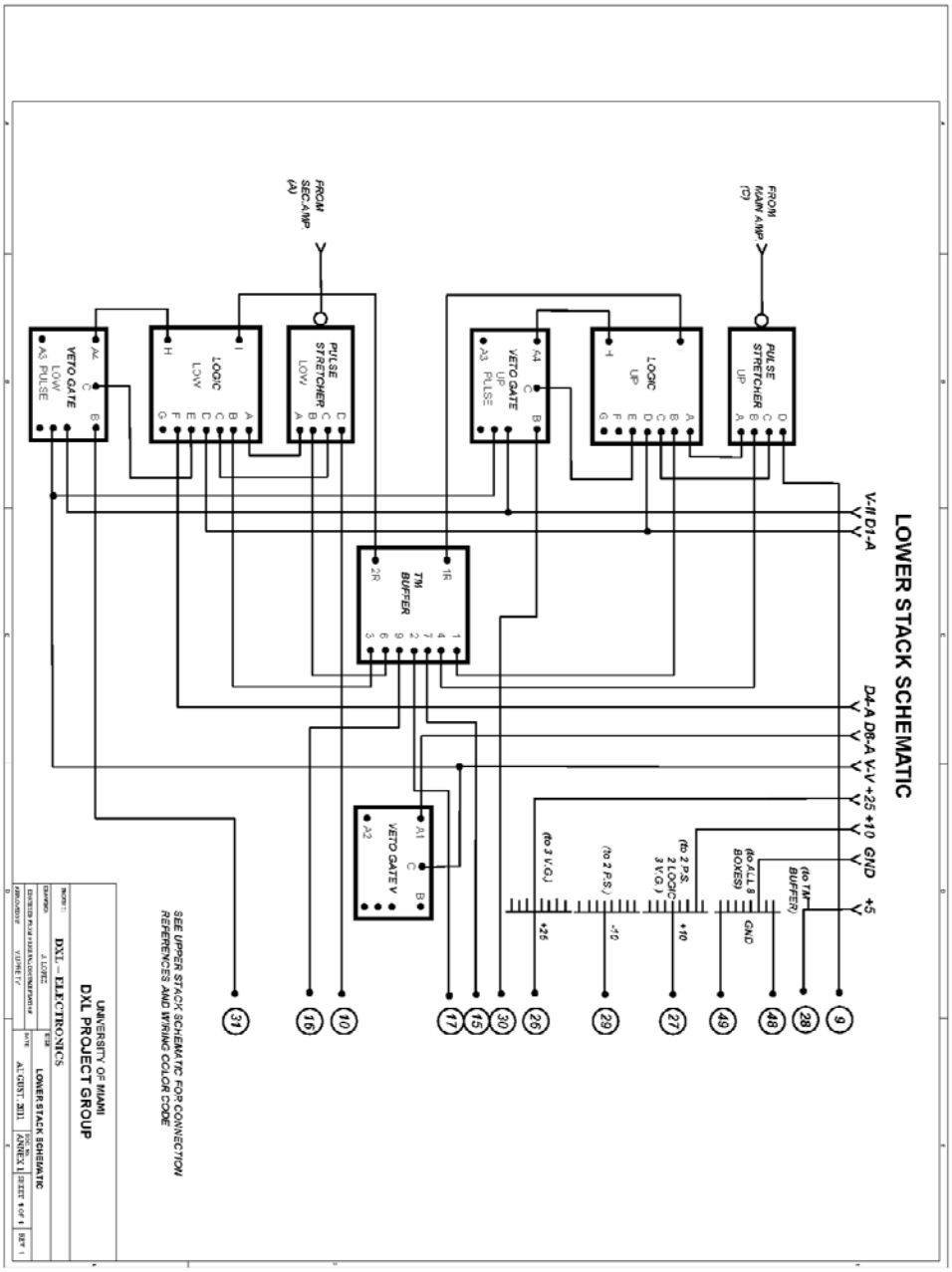

Figure A.3: Lower Stack Electronics Schematic

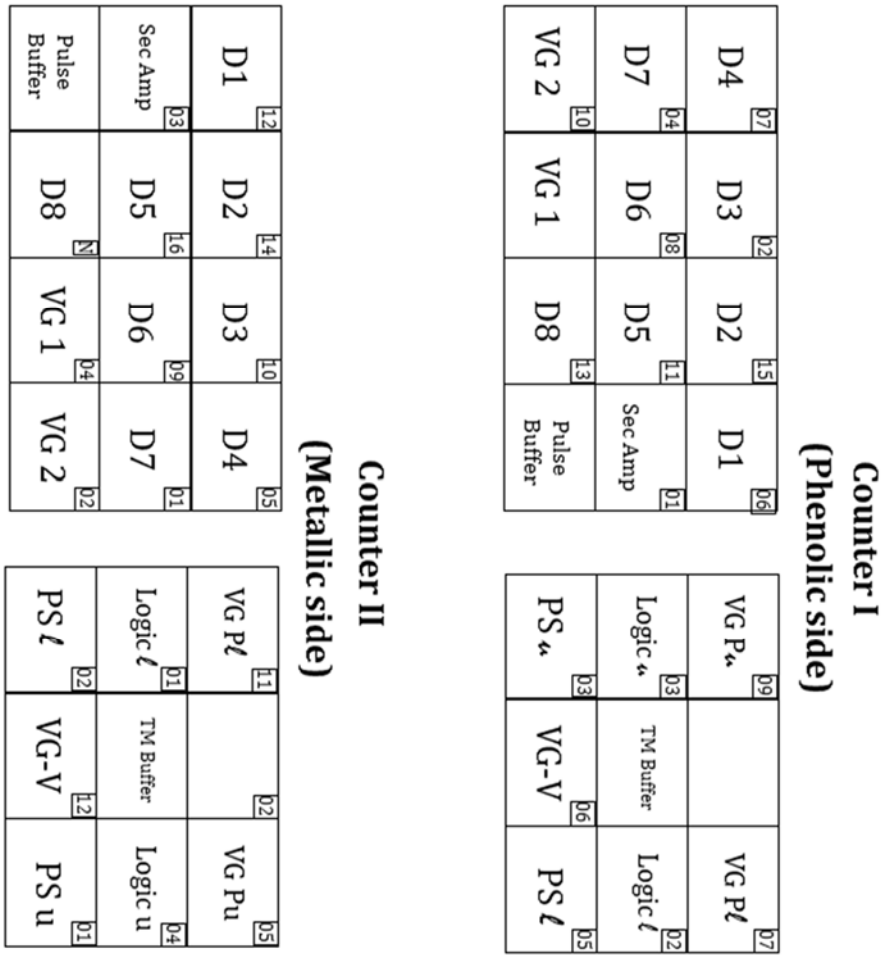

Figure A.4: Upper and Lower Stack Electronics Arrangement

	1	2	3	4	5	6	7	8	9	10	11	12	13	14	15	16
0	SFID	PS1.a	PS1.1	PS II.a	ES II.1	Counter 1	Flow Sol monitor I	Counter 17	T2	PS1.u	Analog Spare	PS II.u	Flow So. Monitor II	Cal Sol Monitor	Frame Sync	Frame Sync
1	SFID	PS1.a	PS1.1	PS II.a	ES II.1	Counter 2	Flow Sol monitor I	Counter 13	LCU-I	PS1.u	Analog Spare	PS II.u	Flow So. monitor II	Cal Sol monitor	Frame Sync	Frame Sync
2	SFID	PS1.a	PS1.1	PS II.a	ES II.1	Counter 3	Flow Sol monitor I	Counter 19	LPU-II	PS1.u	Analog Spare	PS II.u	Flow So. monitor II	Cal Sol monitor	Frame Sync	Frame Sync
3	SFID	PS1.a	PS1.1	PS II.a	ES II.1	Counter 4	Flow Sol monitor I	Counter 20	T5	PS1.u	Analog Spare	PS II.u	Flow So. monitor II	Cal Sol monitor	Frame Sync	Frame Sync
4	SFID	PS1.a	PS1.1	PS II.a	ES II.1	Counter 5	Flow Sol monitor I	Counter 21	LPU-I	PS1.u	Analog Spare	PS II.u	Flow So. monitor II	Cal Sol monitor	Frame Sync	Frame Sync
5	SFID	PS1.a	PS1.1	PS II.a	ES II.1	Counter 6	Flow Sol monitor I	Counter 22	Subcomm I	PS1.u	Analog Spare	PS II.u	Flow So. monitor II	Cal Sol monitor	Frame Sync	Frame Sync
6	SFID	PS1.a	PS1.1	PS II.a	ES II.1	Counter 7	Flow Sol monitor I	Counter 23	LCU-II	PS1.u	Analog Spare	PS II.u	Flow So. monitor II	Cal Sol monitor	Frame Sync	Frame Sync
7	SFID	PS1.a	PS1.1	PS II.a	ES II.1	Counter 8	Flow Sol monitor I	Counter 24	LCU-I	PS1.u	Analog Spare	PS II.u	Flow So. monitor II	Cal Sol monitor	Frame Sync	Frame Sync
8	SFID	PS1.a	PS1.1	PS II.a	ES II.1	Counter 9	Flow Sol monitor I	Counter 25	LPU-II	PS1.u	Analog Spare	PS II.u	Flow So. monitor II	Cal Sol monitor	Frame Sync	Frame Sync
9	SFID	PS1.a	PS1.1	PS II.a	ES II.1	Counter 10	Flow Sol monitor I	Counter 25	Pressure I	PS1.u	Analog Spare	PS II.u	Flow So. monitor II	Cal Sol monitor	Frame Sync	Frame Sync
10	SFID	PS1.a	PS1.1	PS II.a	ES II.1	Counter 11	Flow Sol monitor I	Counter 27	Pressure II	PS1.u	Analog Spare	PS II.u	Flow So. monitor II	Cal Sol monitor	Frame Sync	Frame Sync
11	SFID	PS1.a	PS1.1	PS II.a	ES II.1	Counter 12	Flow Sol monitor I	Counter 23	Subcomm II	PS1.u	Analog Spare	PS II.u	Flow So. monitor II	Cal Sol monitor	Frame Sync	Frame Sync
12	SFID	PS1.a	PS1.1	PS II.a	ES II.1	Counter 13	Flow Sol monitor I	Analog Spare	T1	PS1.u	Analog Spare	PS II.u	Flow So. monitor II	Cal Sol monitor	Frame Sync	Frame Sync
13	SFID	PS1.a	PS1.1	PS II.a	ES II.1	Counter 14	Flow Sol monitor I	Analog Spare	LCL-II	PS1.u	Analog Spare	PS II.u	Flow So. monitor II	Cal Sol monitor	Frame Sync	Frame Sync
14	SFID	PS1.a	PS1.1	PS II.a	ES II.1	Counter 15	Flow Sol monitor I	Analog Spare	Exp. 28 V monitor	PS1.u	Analog Spare	PS II.u	Flow So. monitor II	Cal Sol monitor	Frame Sync	Frame Sync
15	SFID	PS1.a	PS1.1	PS II.a	ES II.1	Counter 16	Flow Sol monitor I	Analog Spare	LPU-I	PS1.u	Analog Spare	PS II.u	Flow So. monitor II	Cal Sol monitor	Frame Sync	Frame Sync
16	SFID	PS1.a	PS1.1	PS II.a	ES II.1	Counter 1	Flow Sol monitor I	Counter 17	Exp +10 V monitor	PS1.u	Analog Spare	PS II.u	Flow So. monitor II	Cal Sol monitor	Frame Sync	Frame Sync
17	SFID	PS1.a	PS1.1	PS II.a	ES II.1	Counter 2	Flow Sol monitor I	Counter 13	Exp +25 V monitor	PS1.u	Analog Spare	PS II.u	Flow So. monitor II	Cal Sol monitor	Frame Sync	Frame Sync
18	SFID	PS1.a	PS1.1	PS II.a	ES II.1	Counter 3	Flow Sol monitor I	Counter 19	Exp +5 V monitor	PS1.u	Analog Spare	PS II.u	Flow So. monitor II	Cal Sol monitor	Frame Sync	Frame Sync
19	SFID	PS1.a	PS1.1	PS II.a	ES II.1	Counter 4	Flow Sol monitor I	Counter 20	Exp -10 V monitor	PS1.u	Analog Spare	PS II.u	Flow So. monitor II	Cal Sol monitor	Frame Sync	Frame Sync
20	SFID	PS1.a	PS1.1	PS II.a	ES II.1	Counter 5	Flow Sol monitor I	Counter 21	-10 II	PS1.u	Analog Spare	PS II.u	Flow So. monitor II	Cal Sol monitor	Frame Sync	Frame Sync
21	SFID	PS1.a	PS1.1	PS II.a	ES II.1	Counter 6	Flow Sol monitor I	Counter 22	Sig. ground (0 V)	PS1.u	Analog Spare	PS II.u	Flow So. monitor II	Cal Sol monitor	Frame Sync	Frame Sync
22	SFID	PS1.a	PS1.1	PS II.a	ES II.1	Counter 7	Flow Sol monitor I	Counter 23	Solenoid monitor	PS1.u	Analog Spare	PS II.u	Flow So. monitor II	Cal Sol monitor	Frame Sync	Frame Sync
23	SFID	PS1.a	PS1.1	PS II.a	ES II.1	Counter 8	Flow Sol monitor I	Counter 24	Analog Spare	PS1.u	Analog Spare	PS II.u	Flow So. monitor II	Cal Sol monitor	Frame Sync	Frame Sync
24	SFID	PS1.a	PS1.1	PS II.a	ES II.1	Counter 9	Flow Sol monitor I	Counter 25	Analog Spare	PS1.u	Analog Spare	PS II.u	Flow So. monitor II	Cal Sol monitor	Frame Sync	Frame Sync
25	SFID	PS1.a	PS1.1	PS II.a	ES II.1	Counter 10	Flow Sol monitor I	Counter 25	Analog Spare	PS1.u	Analog Spare	PS II.u	Flow So. monitor II	Cal Sol monitor	Frame Sync	Frame Sync
26	SFID	PS1.a	PS1.1	PS II.a	ES II.1	Counter 11	Flow Sol monitor I	Counter 27	Analog Spare	PS1.u	Analog Spare	PS II.u	Flow So. monitor II	Cal Sol monitor	Frame Sync	Frame Sync
27	SFID	PS1.a	PS1.1	PS II.a	ES II.1	Counter 12	Flow Sol monitor I	Counter 23	Analog Spare	PS1.u	Analog Spare	PS II.u	Flow So. monitor II	Cal Sol monitor	Frame Sync	Frame Sync
28	SFID	PS1.a	PS1.1	PS II.a	ES II.1	Counter 13	Flow Sol monitor I	Analog Spare	Analog Spare	PS1.u	Analog Spare	PS II.u	Flow So. monitor II	Cal Sol monitor	Frame Sync	Frame Sync
29	SFID	PS1.a	PS1.1	PS II.a	ES II.1	Counter 14	Flow Sol monitor I	Analog Spare	Analog Spare	PS1.u	Analog Spare	PS II.u	Flow So. monitor II	Cal Sol monitor	Frame Sync	Frame Sync
30	SFID	PS1.a	PS1.1	PS II.a	ES II.1	Counter 15	Flow Sol monitor I	Analog Spare	Frame Counter	PS1.u	Analog Spare	PS II.u	Flow So. monitor II	Cal Sol monitor	Frame Sync	Frame Sync
31	SFID	PS1.a	PS1.1	PS II.a	ES II.1	Counter 16	Flow Sol monitor I	Analog Spare	Frame Counter	PS1.u	Analog Spare	PS II.u	Flow So. Monitor II	Cal Sol Monitor	Frame Sync	Frame Sync

Figure A.5: TM Matrix

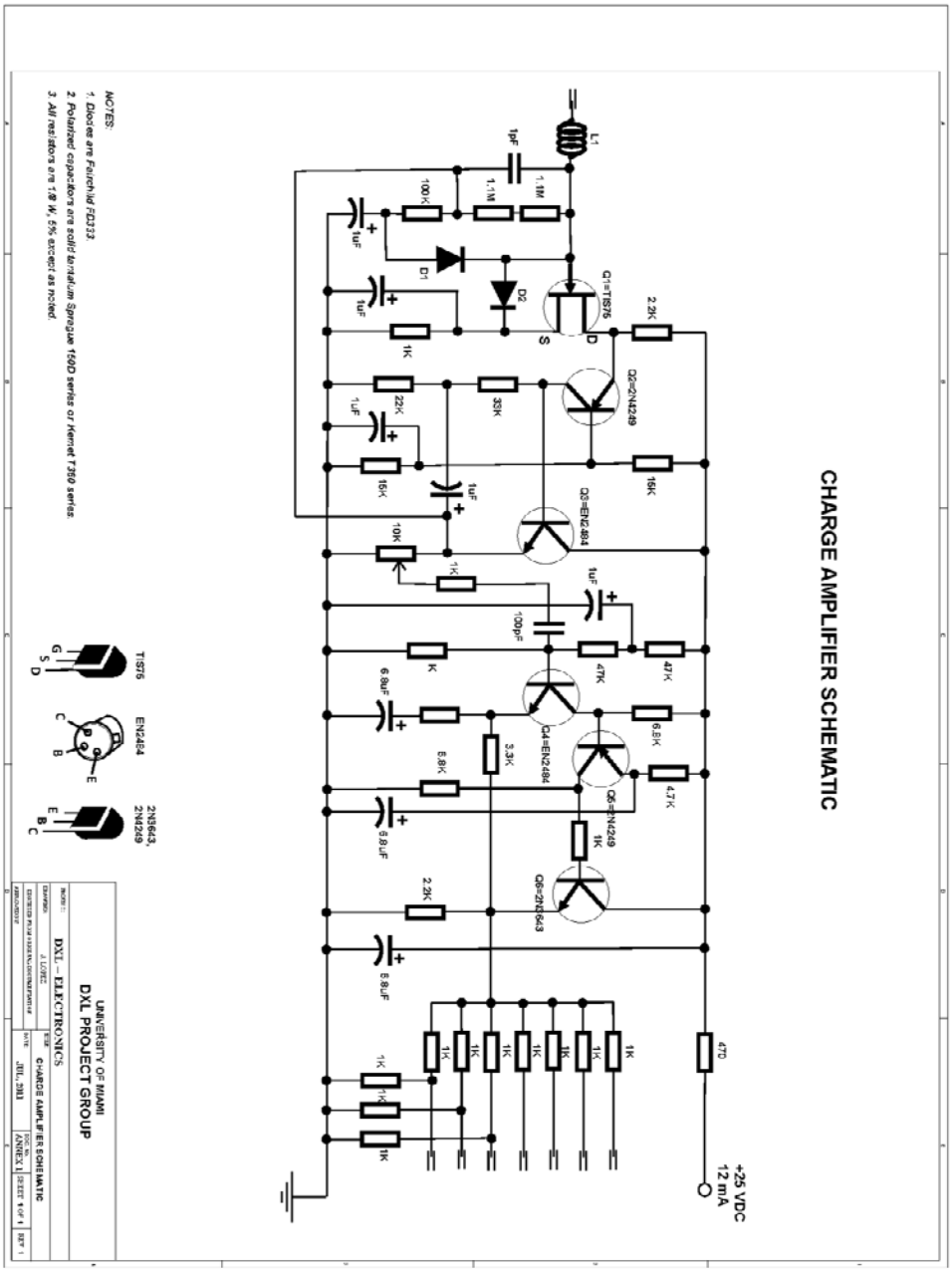

Figure A.6: Charge Amplifier Schematic

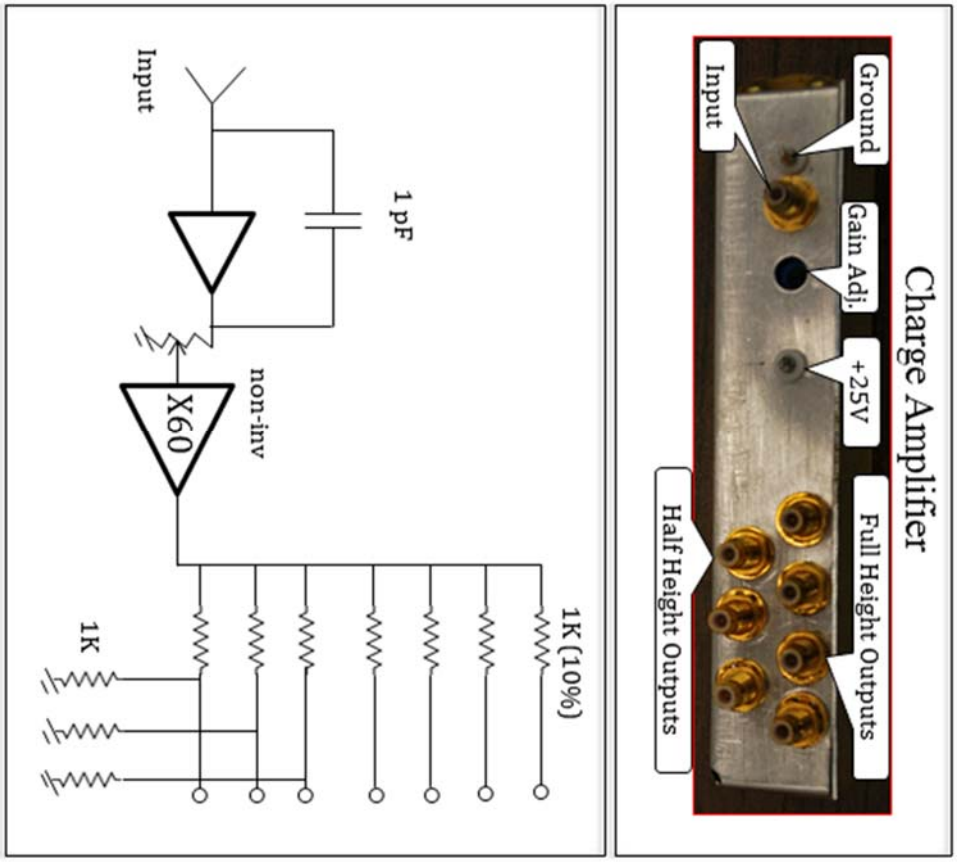

Figure A.7: Charge Amplifier

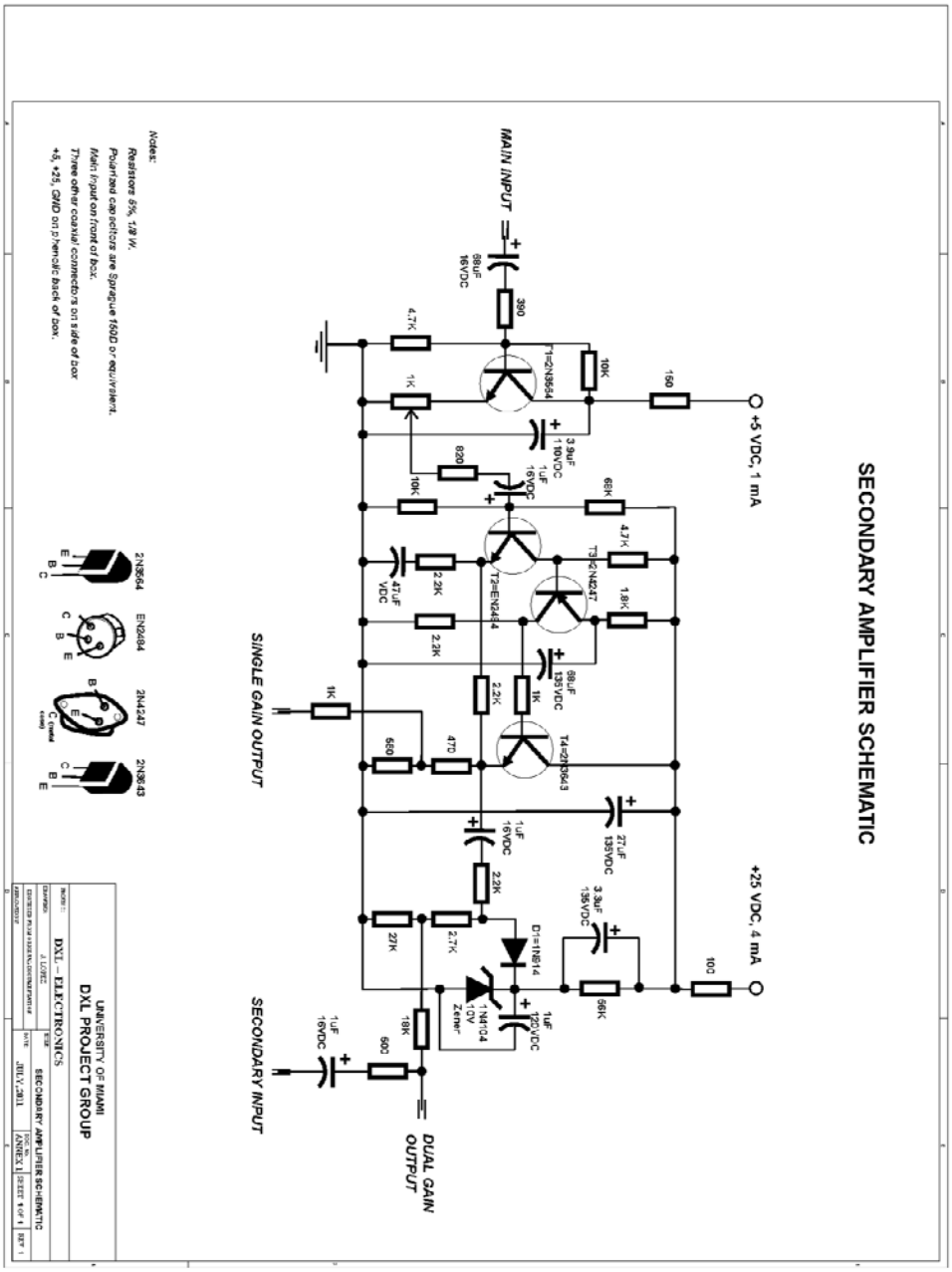

Figure A.8: Secondary Amplifier Schematic

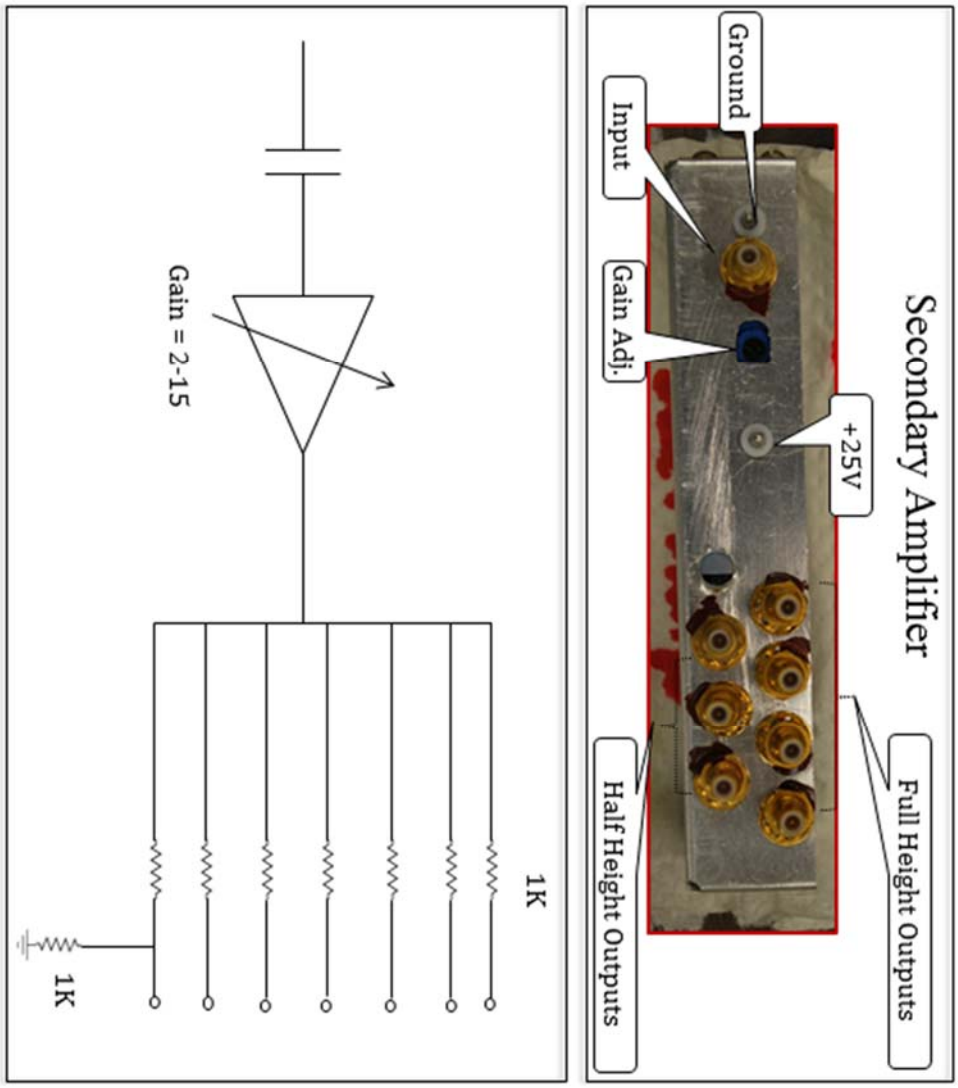

Figure A.9: Secondary Amplifier

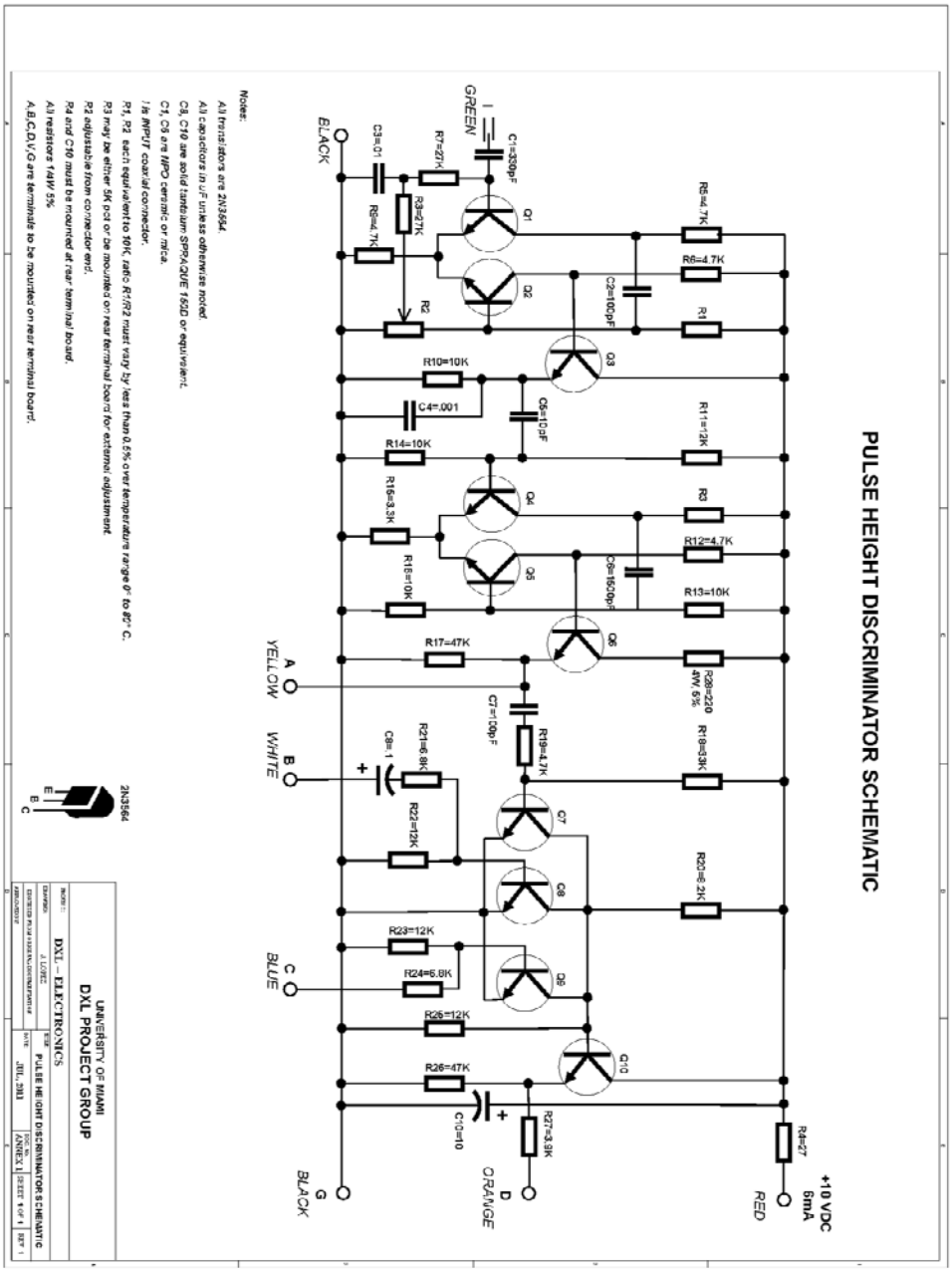

Figure A.10: Discriminator Schematic

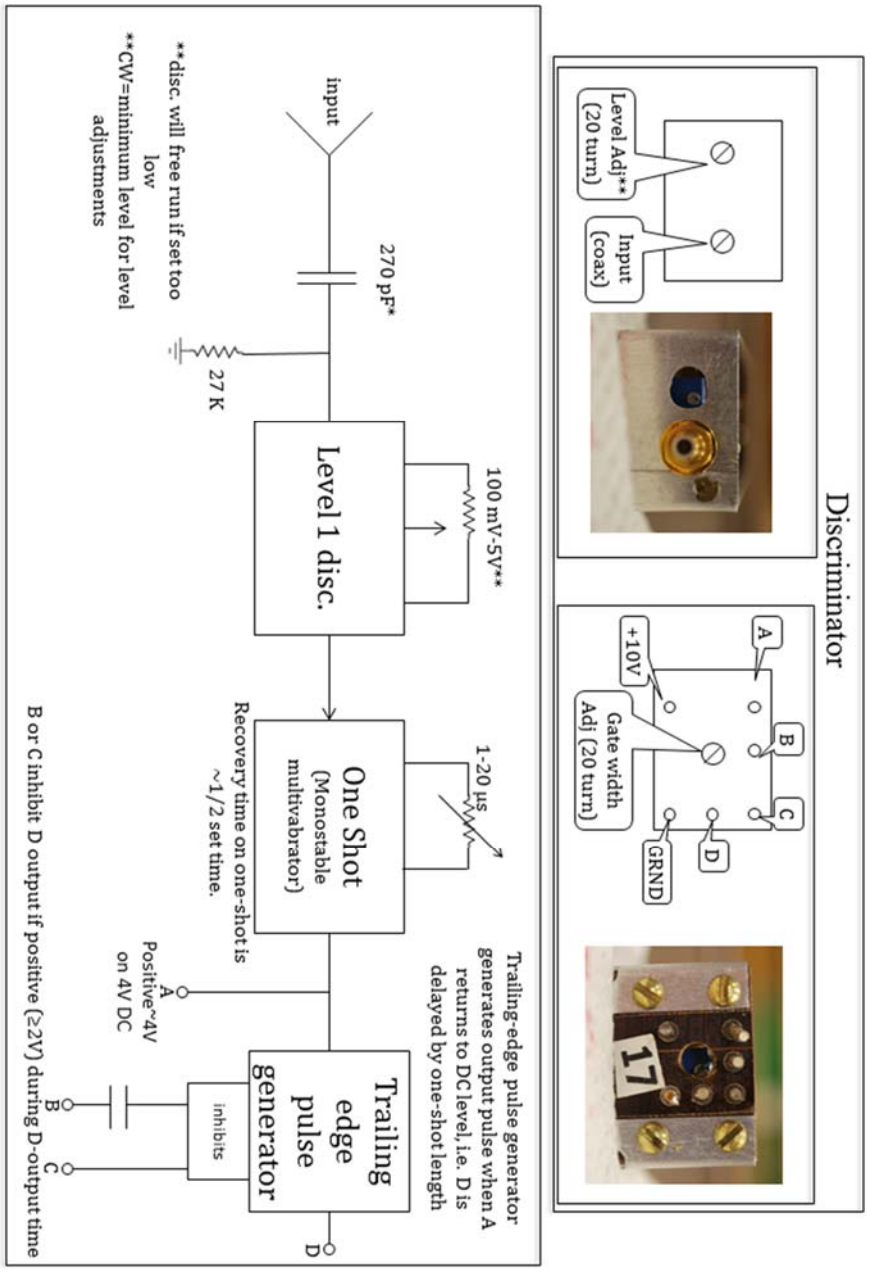

Figure A.11: Discriminator

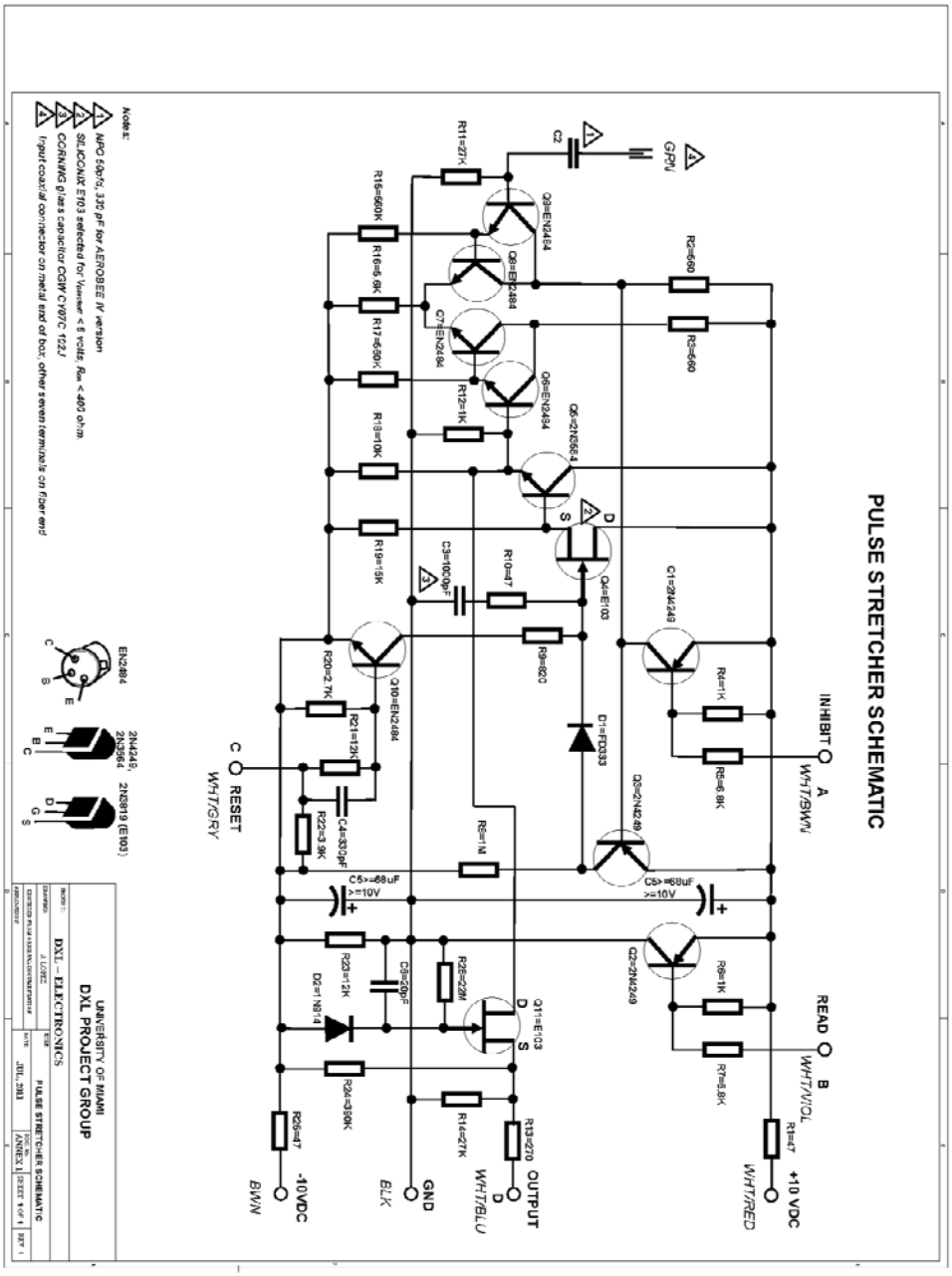

Figure A.12: Pulse Stretcher Schematic

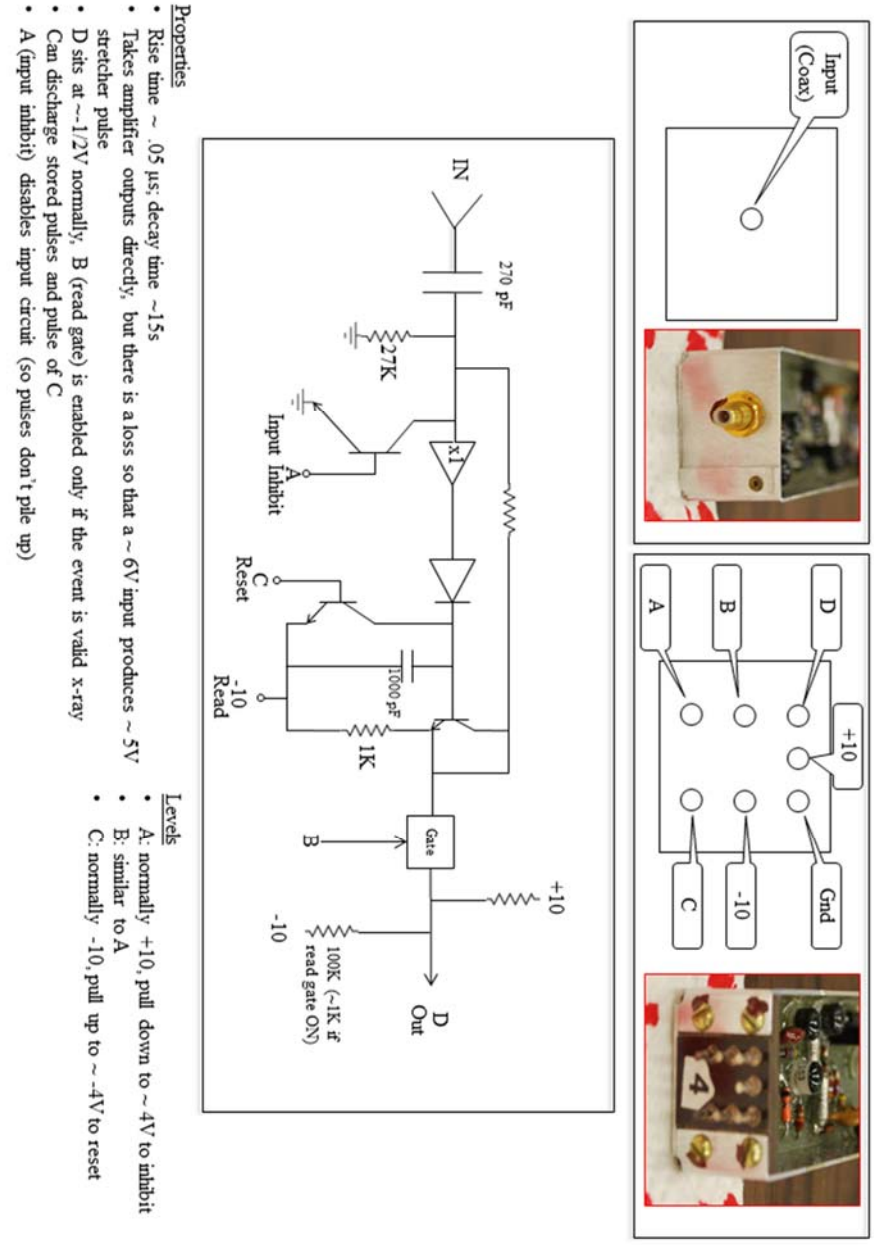

Figure A.13: Pulse Stretcher

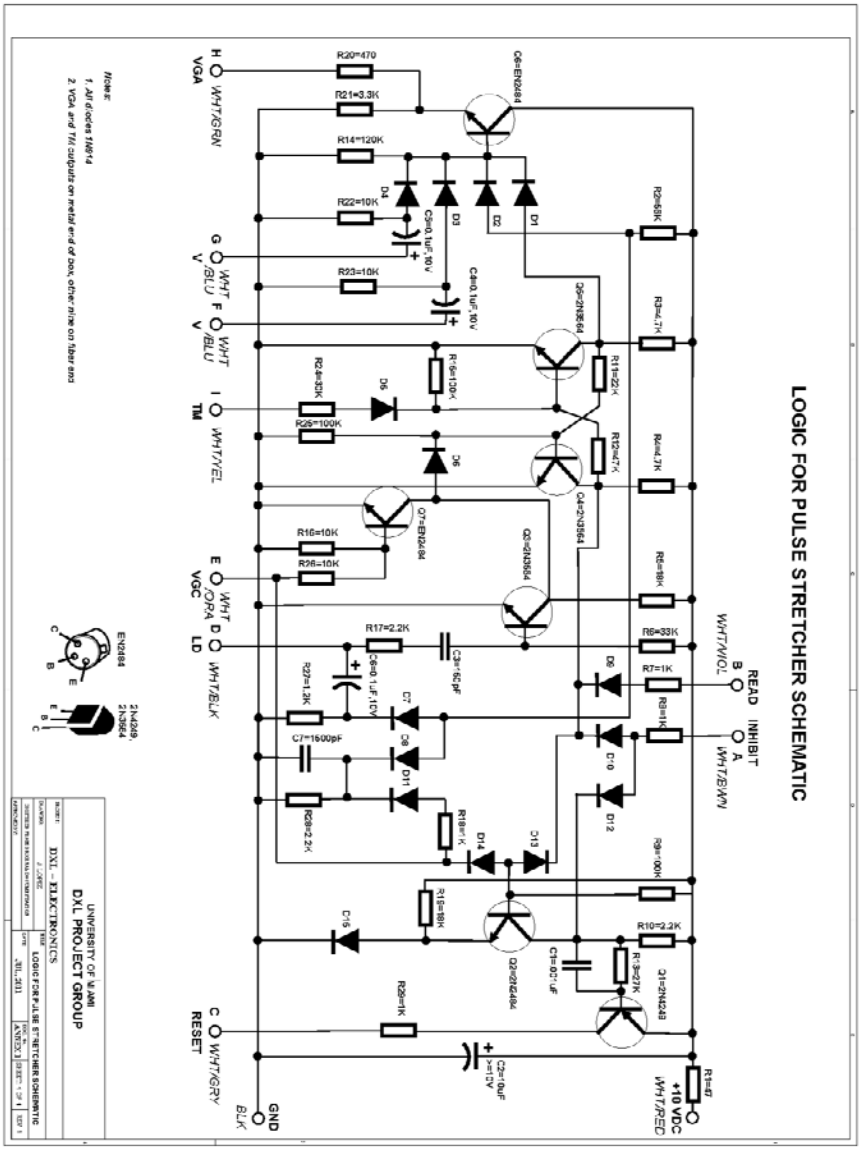

Figure A.14: Logic for Pulse Stretcher Schematic

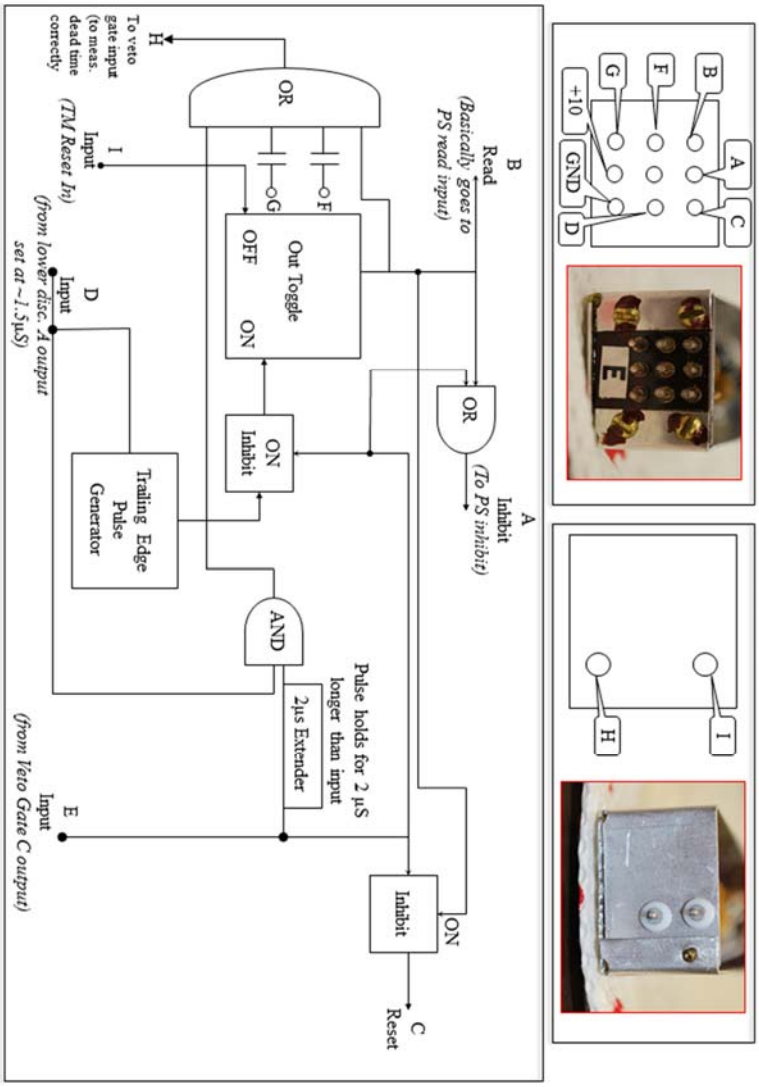

Figure A.15: Logic for Pulse Stretcher

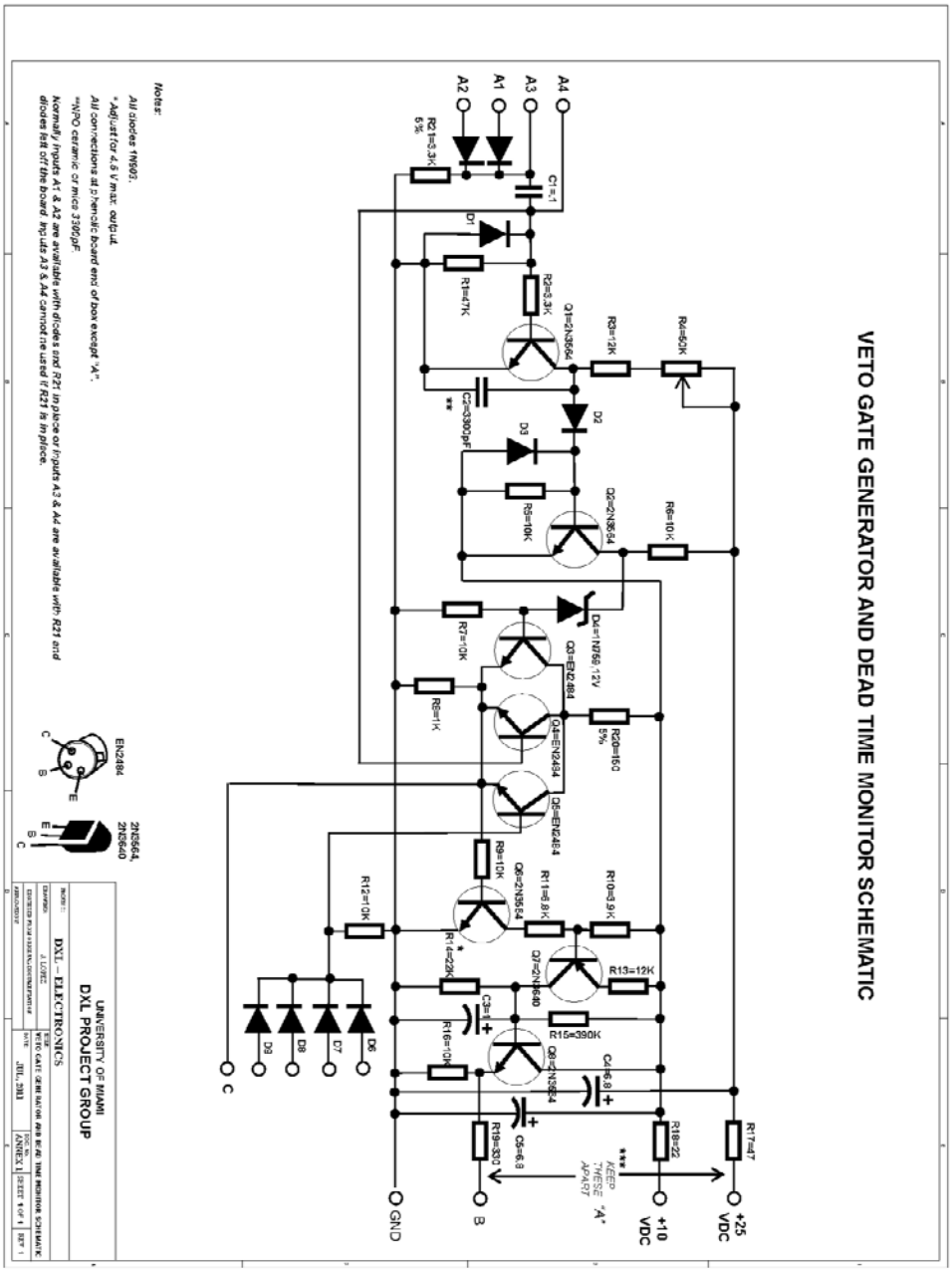

Figure A.16: Veto Gate Schematic

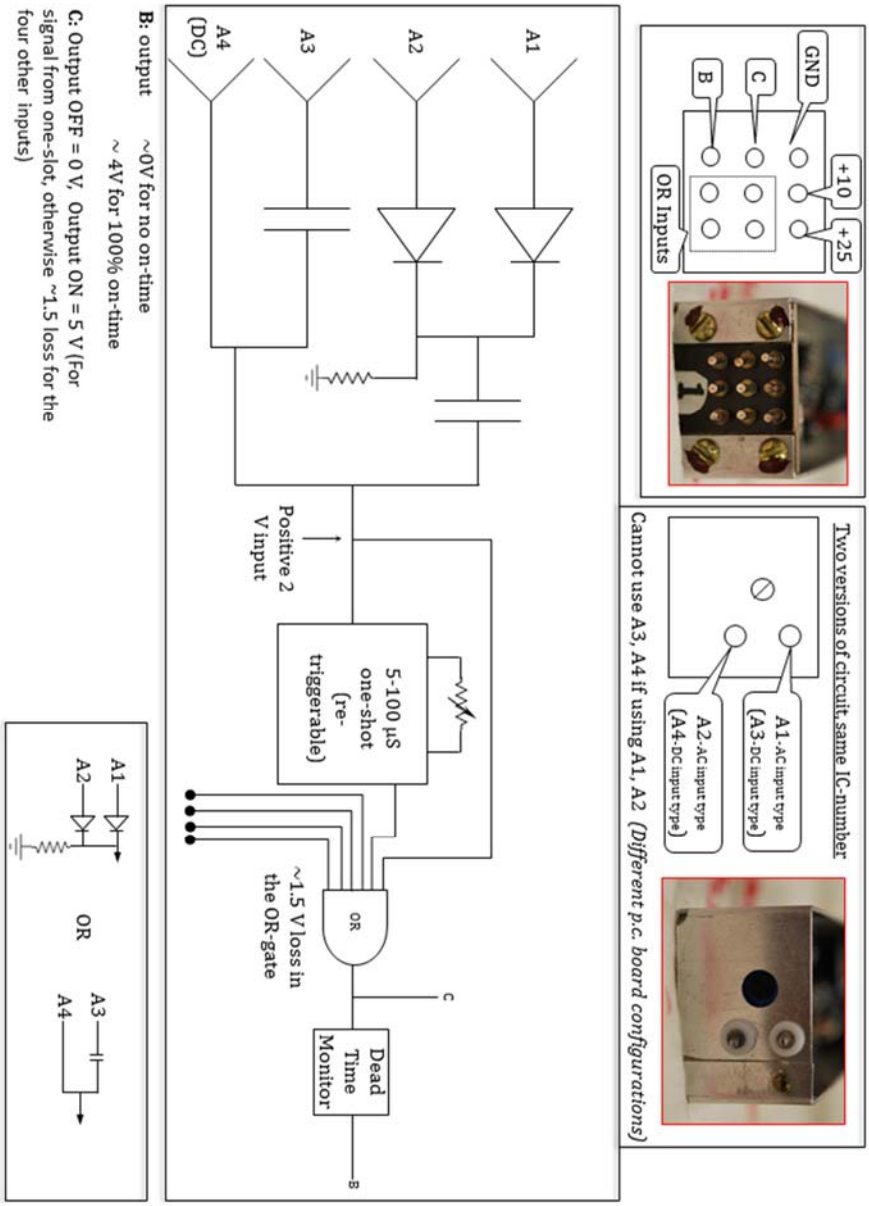

Figure A.17: Veto Gate

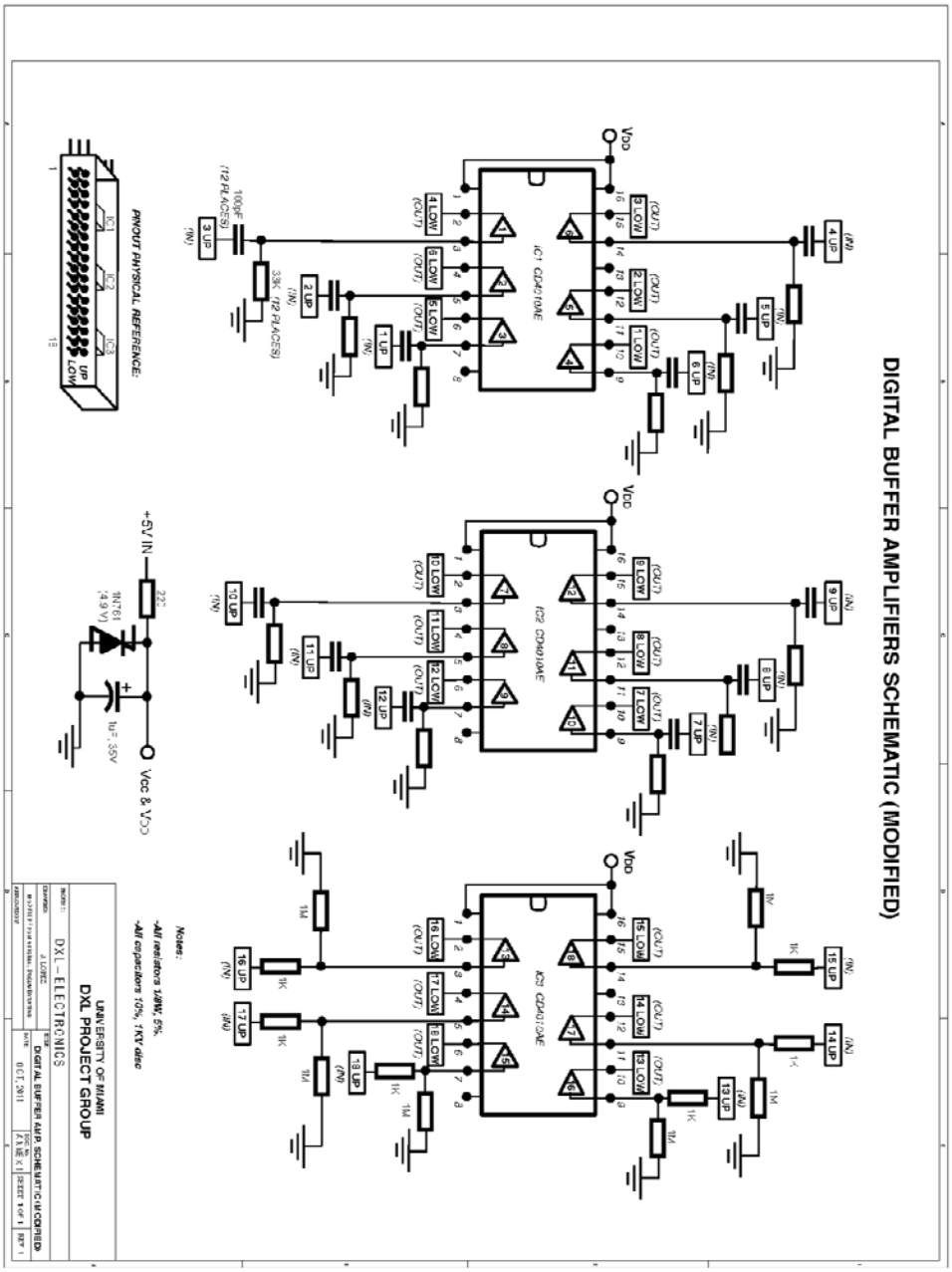

Figure A.18: Pulse Buffer Schematic

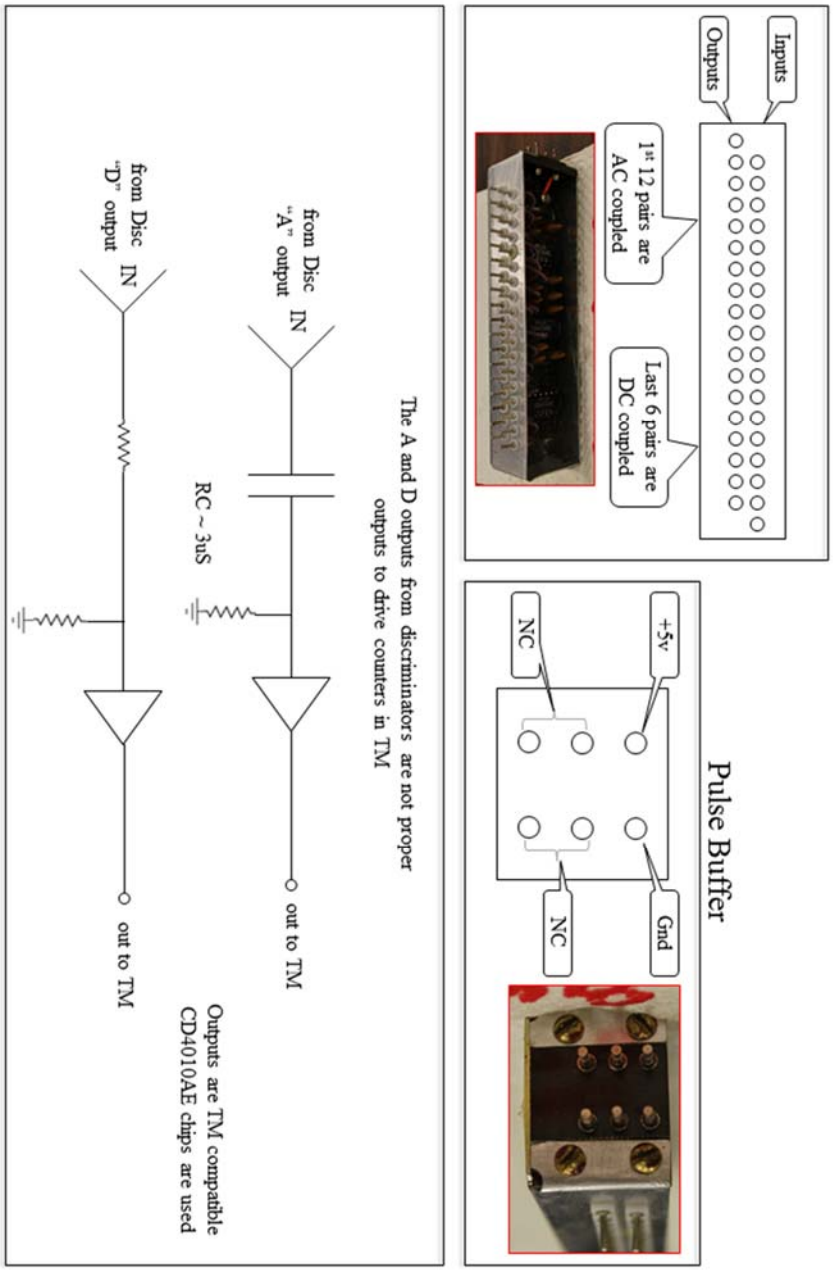

Figure A.19: Pulse Buffer

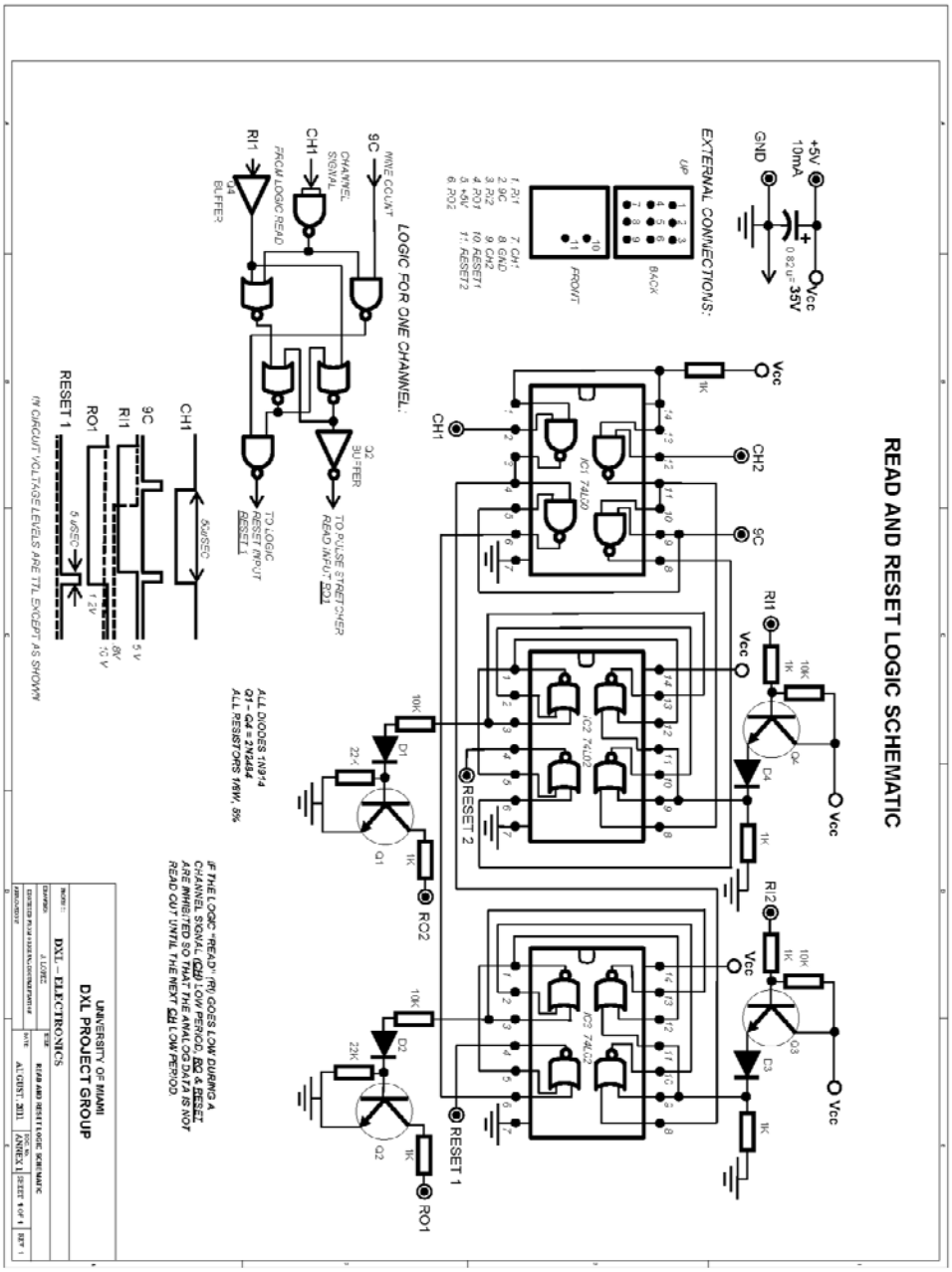

Figure A.20: TM Buffer Schematic

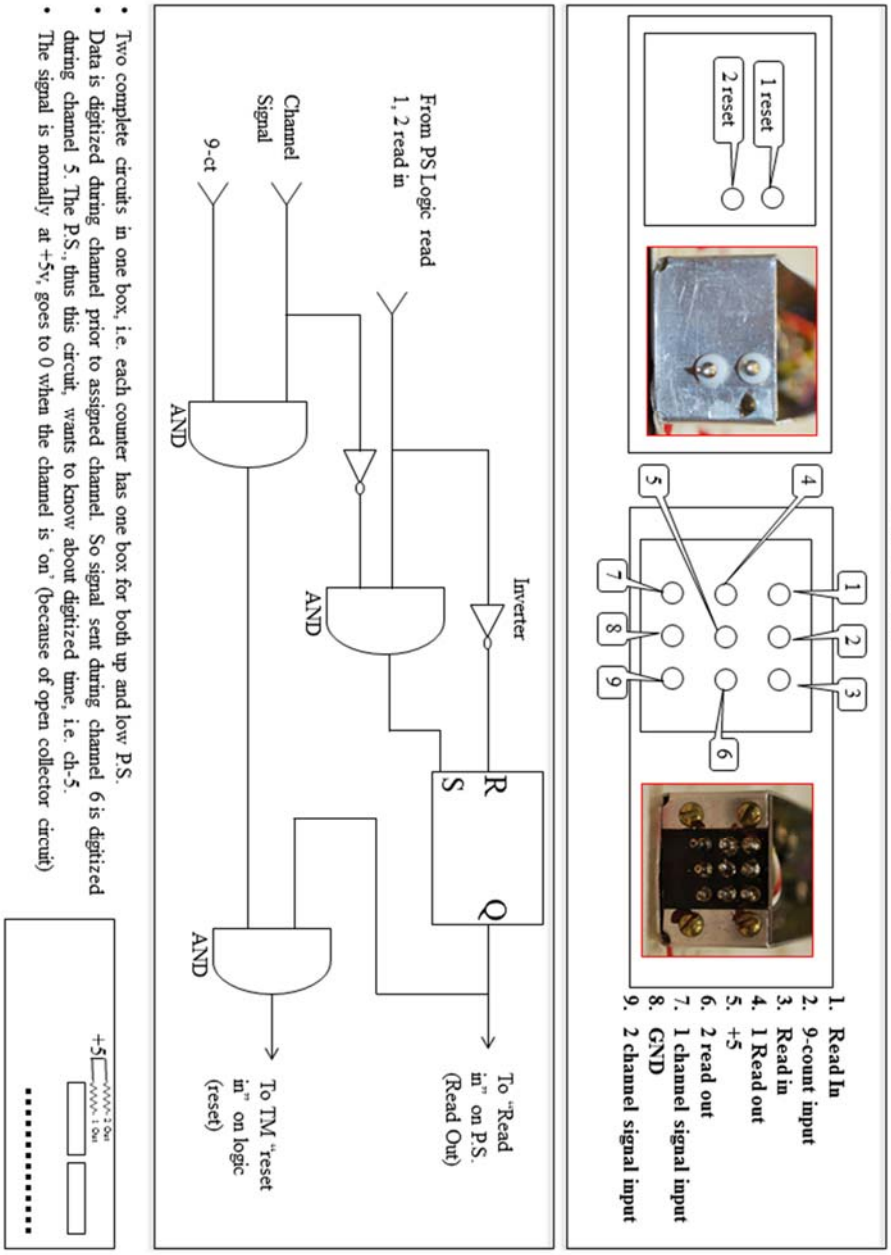

Figure A.21: TM Buffer

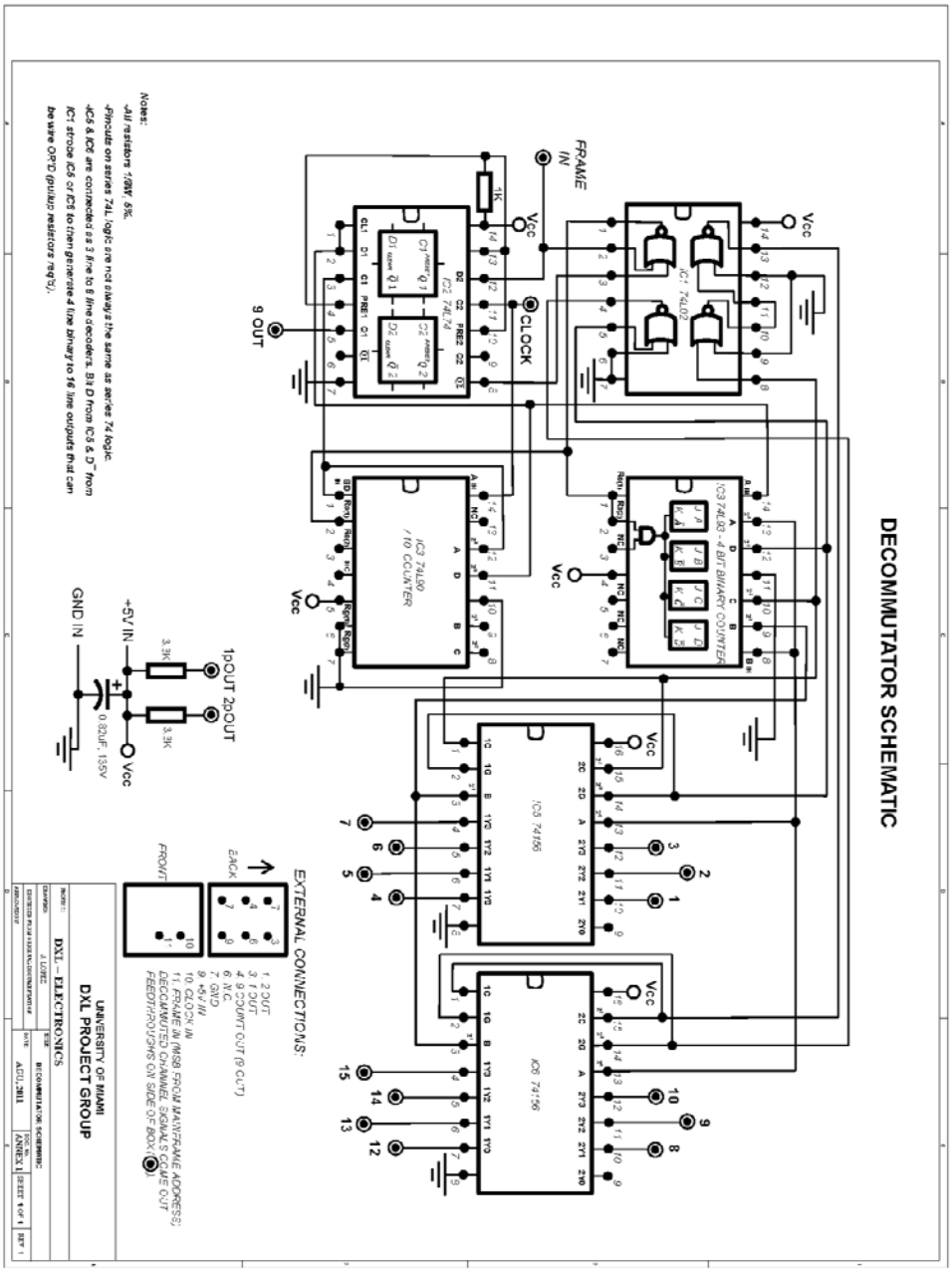

Figure A.22: Decommutator Schematic

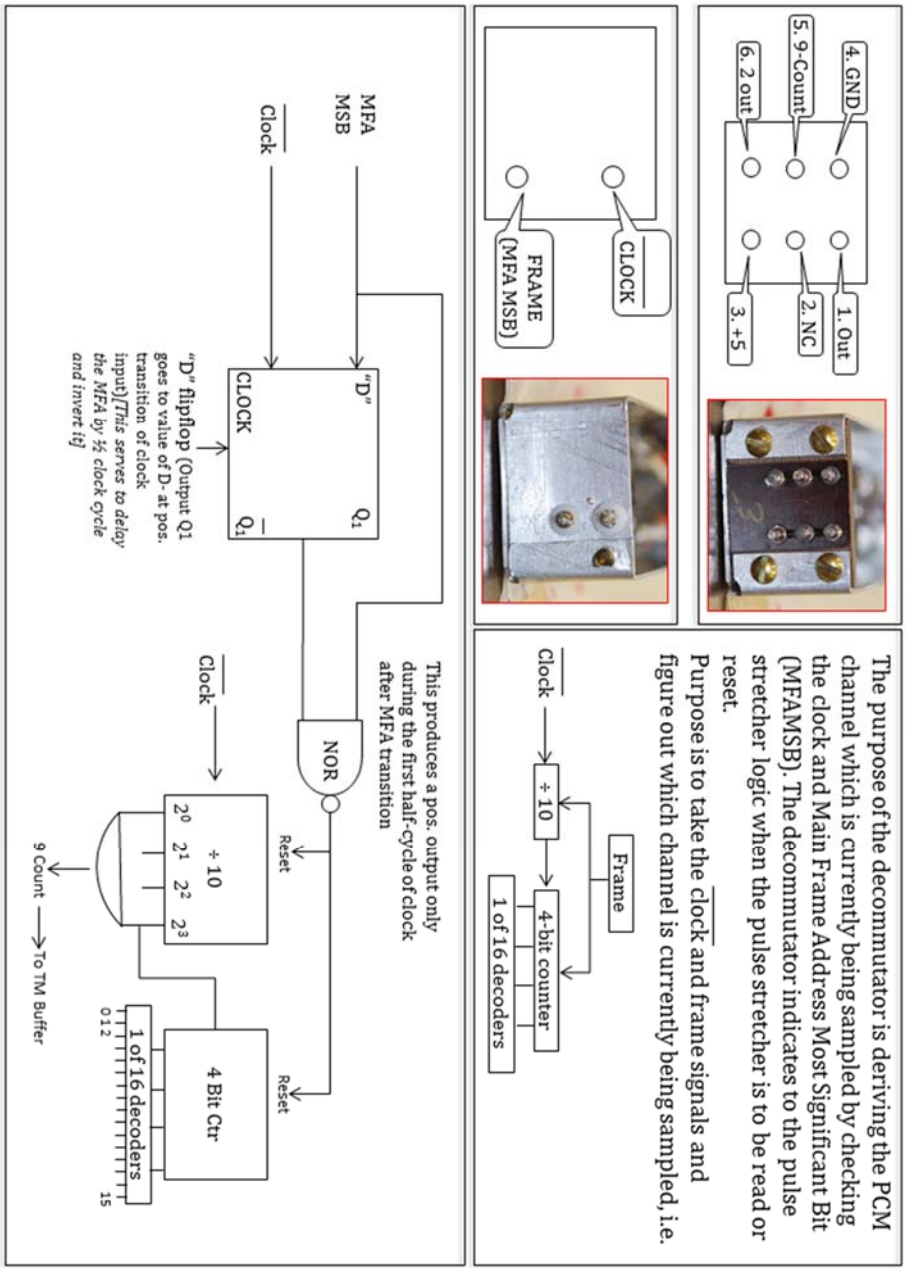

Figure A.23: Decommutator

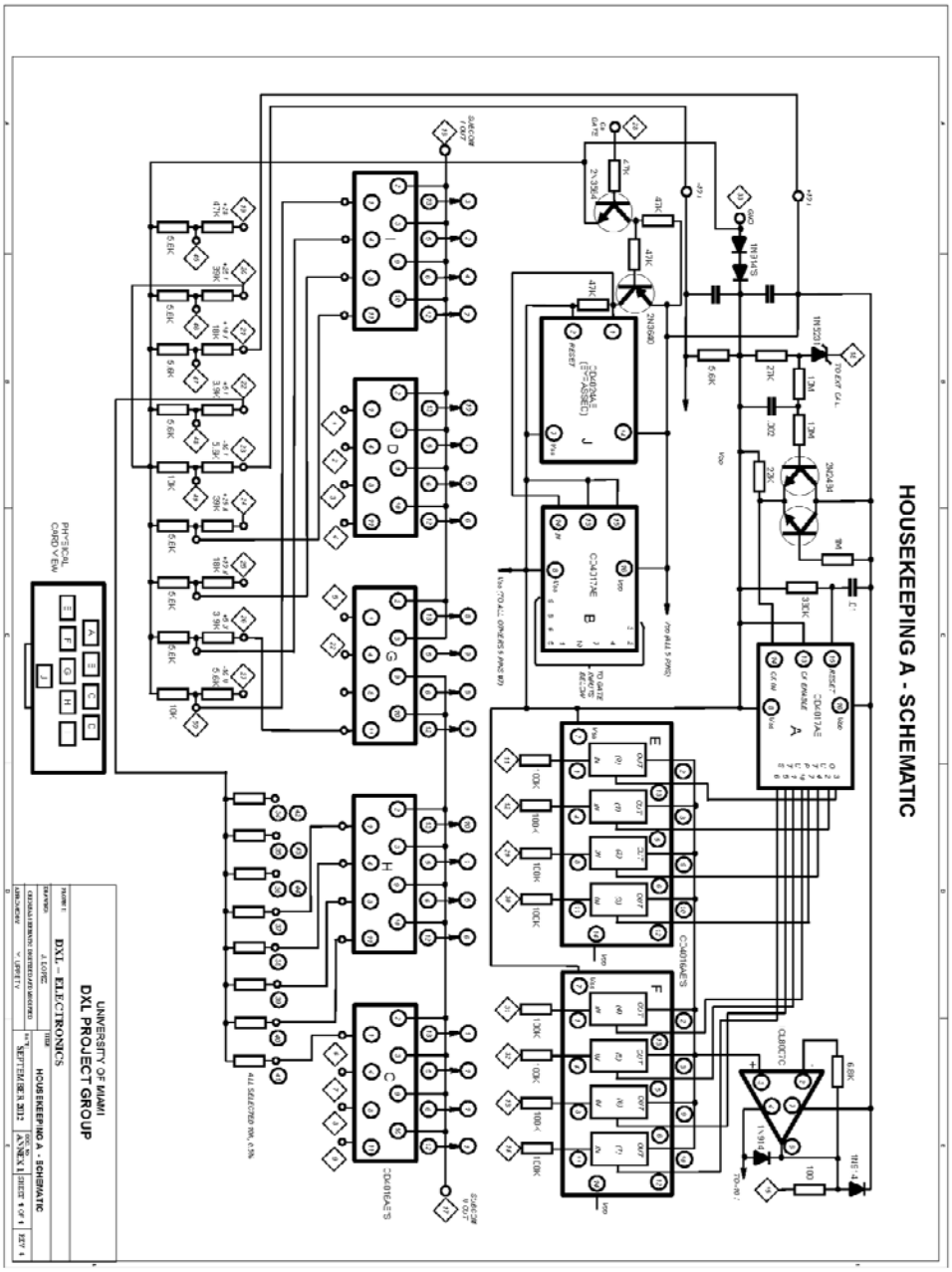

Figure A.24: Housekeeping A Schematic

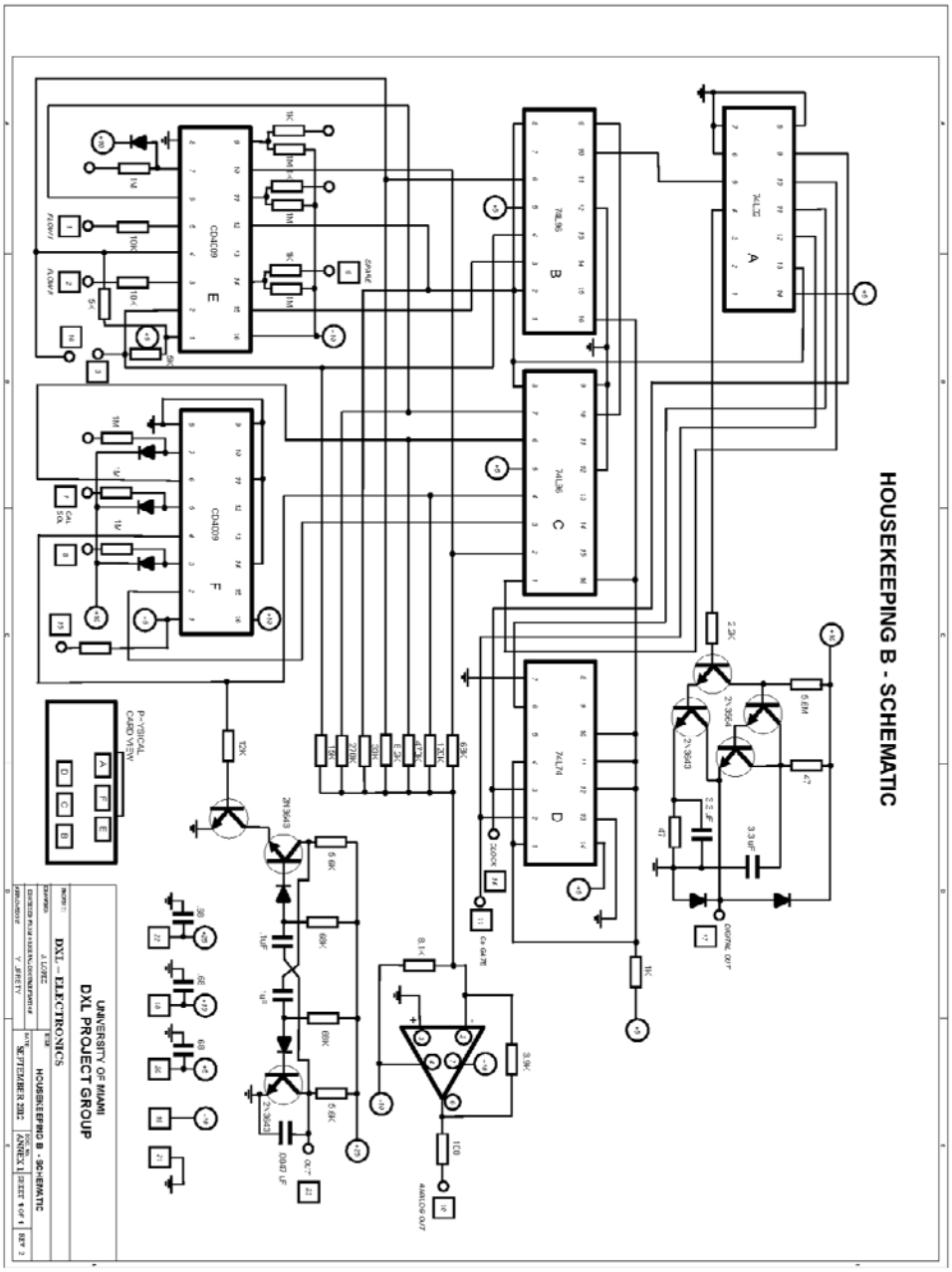

Figure A.25: Housekeeping B Schematic

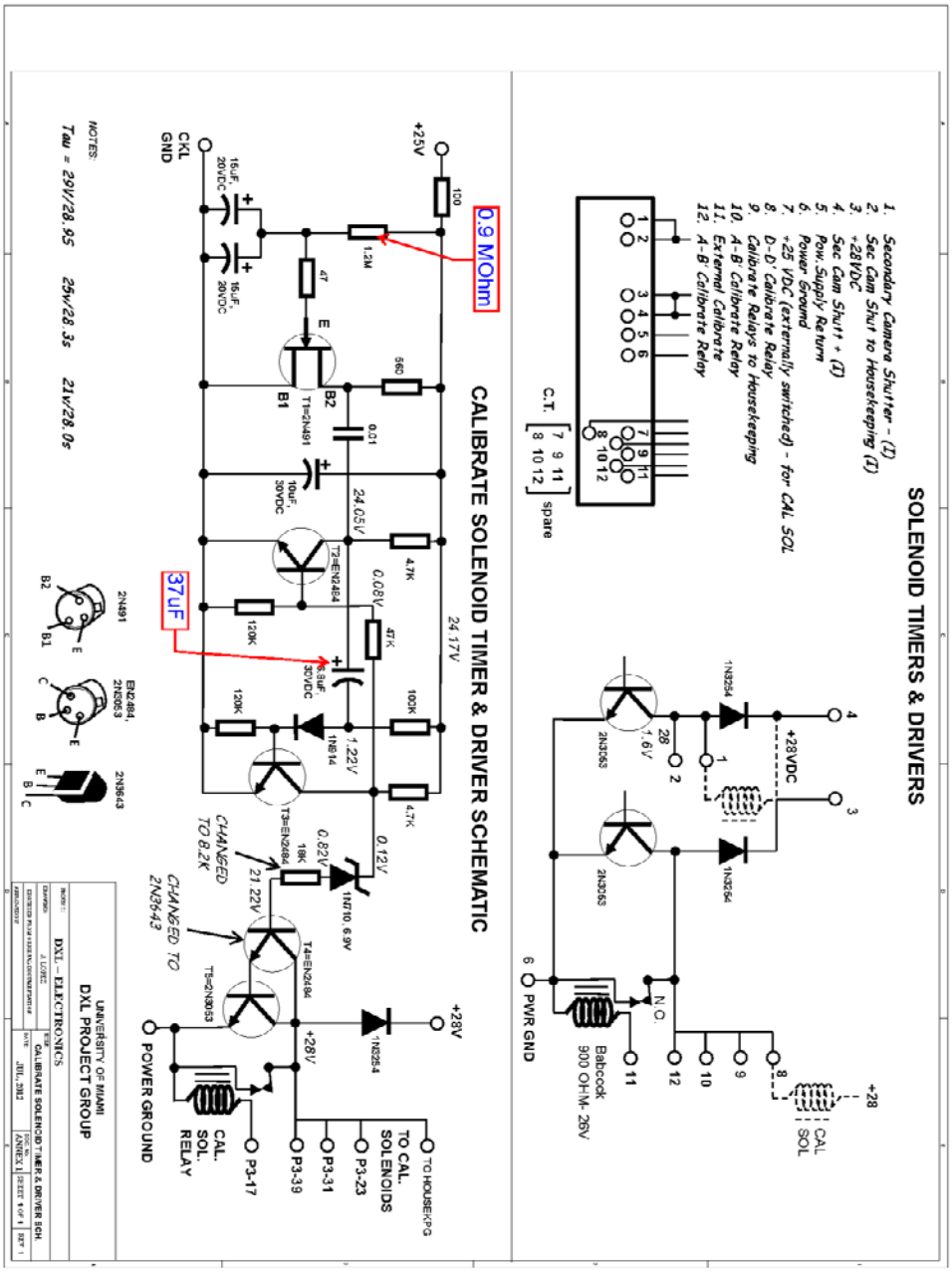

Figure A.26: Calibrate Solenoid and Timer Schematic

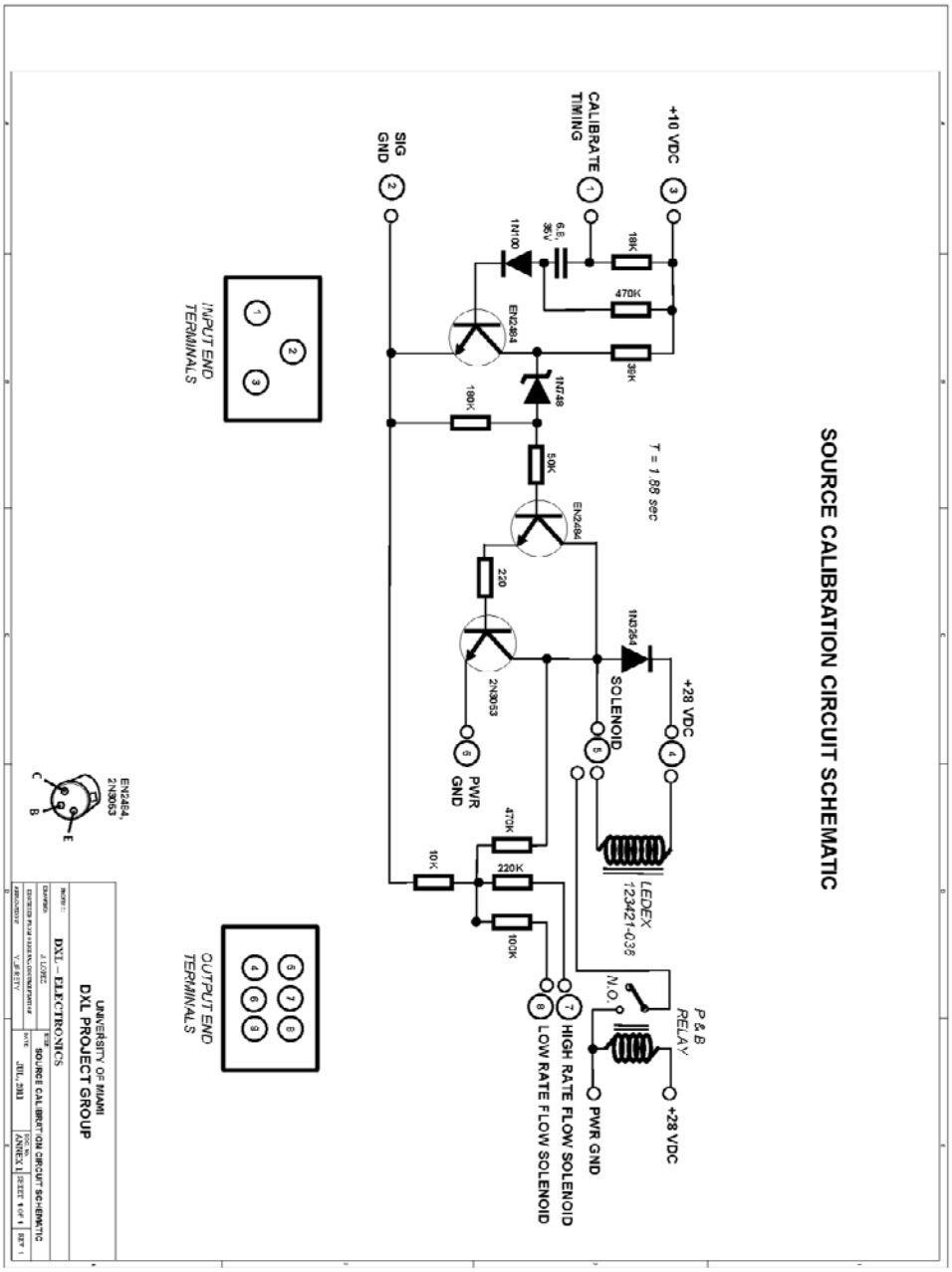

Figure A.27: Source Calibration Circuit Schematic

BIBLIOGRAPHY

[1] R. Giacconi, H. Gursky, F. R. Paolini, and B. B. Rossi, "Evidence for X rays from sources outside the solar system," *Phys. Rev. Lett.*, vol. 9, no. 11, pp. 439–443, Dec. 1962.

[2] C. S. Bowyer, G. B. Field, and J. E. Mack, "Detection of an anisotropic soft X-ray background flux," *Nature*, vol. 217, no. 5123, pp. 32–34, Jan. 1968.

[3] F. O. Williamson, W. T. Sanders, W. L. Kraushaar, D. McCammon, R. J. Borken, and A. N. Bunner, "Observation of features in the soft X-ray background flux," *Astrophys. J.*, vol. 193, p. L133, Nov. 1974.

[4] W. T. Sanders, W. L. Kraushaar, J. A. Nousek, and P. M. Fried, "Soft diffuse X-rays in the southern galactic hemisphere," *Astrophys. J.*, vol. 217, p. L87, Oct. 1977.

[5] P. M. Fried, J. A. Nousek, W. T. Sanders, and W. L. Kraushaar, "The soft X-ray diffuse background and the structure of the local interstellar medium," *Astrophys. J.*, vol. 242, p. 987, Dec. 1980.

[6] D. McCammon and W. T. Sanders, "The soft X-ray background and its origins," *Annu. Rev. Astron. Astrophys.*, vol. 28, no. 1, pp. 657–688, Sep. 1990.

[7] S. L. Snowden, M. J. Freyberg, P. P. Plucinsky, J. H. M. M. Schmitt, J. Trümper, W. Voges, R. J. Edgar, D. McCammon, and W. T. Sanders, "First maps of the soft X-ray diffuse background from the ROSAT XRT/PSPC all-sky survey," *Astrophys. J.*, vol. 454, p. 643, Dec. 1995.

[8] J. D. Slavin and P. C. Frisch, "The local bubble and beyond Lyman-Spitzer-Colloquium," in *Lecture Notes in Physics*, 1998, vol. 506, pp. 305–308.

[9] H. Gursky, R. Giacconi, F. R. Paolini, and B. B. Rossi, "Further evidence for the existence of galactic X-rays," *Phys. Rev. Lett.*, vol. 11, no. 12, pp. 530–535, 1963.

[10] A. N. Bunner, P. L. Coleman, W. L. Kraushaar, and D. McCammon, "Low-energy diffuse X-rays," *Astrophys. J.*, vol. 167, p. L3, Jul. 1971.

[11] D. McCammon, D. N. Burrows, W. T. Sanders, and W. L. Kraushaar, "The soft X-ray diffuse background," *Astrophys. J.*, vol. 269, p. 107, Jun. 1983.

[12] F. J. Marshall and G. W. Clark, “SAS 3 survey of the soft X-ray background,” *Astron. J.*, vol. 287, pp. 633–652, 1984.

[13] G. P. Garmire, J. A. Nousek, K. M. V. Apparao, D. N. Burrows, R. L. Fink, and R. P. Kraft, “The soft X-ray diffuse background observed with the HEAO 1 low-energy detectors,” *Astron. J.*, vol. 399, pp. 694–703, 1992.

[14] W. T. Sanders, R. J. Edgar, W. L. Kraushaar, D. McCammon, and J. P. Morgenthaler, “Spectra of the 1/4 keV X-Ray diffuse background from the Diffuse X□Ray Spectrometer experiment,” *Astrophys. J.*, vol. 554, no. 2, pp. 694–709, Jun. 2001.

[15] F. Paerels and S. M. Kahn, “High-resolution X-ray spectroscopy with *Chandra* and *XMM-NEWTON*,” *Annu. Rev. Astron. Astrophys.*, vol. 41, pp. 291–342, 2003.

[16] K. Mitsuda, M. Bautz, H. Inoue, R. L. Kelley, K. Koyama, H. Kunieda, K. Makishima, Y. Ogawara, R. Petre, T. Takahashi, H. Tsunemi, N. E. White, N. Anabuki, L. Angelini, K. A. Arnaud, H. Awaki, A. Bamba, K. Boyce, G. V. Brown, K. W. Chan, J. Cottam, T. Dotani, J. Doty, K. Ebisawa, Y. Ezoe, A. C. Fabian, E. Figueroa-Feliciano, R. Fujimoto, Y. Fukazawa, T. Furusho, A. Furuzawa, K. Gendreau, R. E. Griffiths, Y. Haba, K. Hamaguchi, I. Harrus, G. Hasinger, I. Hatsukade, K. Hayashida, P. J. Henry, J. S. Hiraga, S. S. Holt, A. Hornschemeier, J. P. Hughes, U. Hwang, M. Ishida, Y. Ishisaki, N. Isobe, M. Itoh, N. Iyomoto, S. M. Kahn, T. Kamae, H. Katagiri, J. Kataoka, H. Katayama, N. Kawai, C. A. Kilbourne, K. Kinugasa, S. Kissel, S. Kitamoto, M. Kohama, T. Kohmura, M. Kokubun, T. Kotani, J. Kotoku, A. Kubota, G. M. Madejski, Y. Maeda, F. Makino, A. Markowitz, C. Matsumoto, H. Matsumoto, M. Matsuoka, K. Matsushita, D. McCammon, T. Mihara, K. Misaki, E. Miyata, T. Mizuno, K. Mori, H. Mori, M. Morii, H. Moseley, K. Mukai, H. Murakami, T. Murakami, R. F. Mushotzky, F. Nagase, M. Namiki, H. Negoro, K. Nakazawa, J. A. Nousek, T. Okajima, Y. Ogasaka, T. Ohashi, T. Oshima, N. Ota, M. Ozaki, H. Ozawa, A. N. Parmar, W. D. Pence, F. S. Porter, J. N. Reeves, G. R. Ricker, I. Sakurai, W. T. Sanders, A. Senda, P. Serlemitsos, R. Shibata, Y. Soong, R. K. Smith, M. Suzuki, A. E. Szymkowiak, H. Takahashi, T. Tamagawa, K. Tamura, T. Tamura, Y. Tanaka, M. Tashiro, Y. Tawara, Y. Terada, Y. Terashima, H. Tomida, K. Torii, Y. Tsuboi, M. Tsujimoto, T. G. Tsuru, M. J. L. Turner, Y. Ueda, S. Ueno, M. Ueno, S. Uno, Y. Urata, S. Watanabe, N. Yamamoto, K. Yamaoka, N. Y. Yamasaki, K. Yamashita, M. Yamauchi, S. Yamauchi, T. Yaqoob, D. Yonetoku, and A. Yoshida, “The X-ray observatory *Suzaku*,” *Publ. Astron. Soc. Japan*, vol. 59, no. sp1, pp. S1–S7, 2007.

[17] D. McCammon, R. Almy, E. Apodaca, W. B. Tiest, W. Cui, S. Deiker, M. Galeazzi, M. Juda, A. Lesser, T. Mihara, J. P. Morgenthaler, W. T. Sanders, J. Zhang, E. Figueroa-Feliciano, R. L. Kelley, S. H. Moseley, R. F. Mushotzky, F. S. Porter, C. K. Stahle, and A. E. Szymkowiak, "A high spectral resolution observation of the Soft X-ray diffuse background with thermal detectors," *Astrophys. J.*, vol. 576, no. 1, pp. 188–203, Sep. 2002.

[18] J. J. Bloch, K. Jahoda, M. Juda, D. McCammon, and W. T. Sanders, "Observations of the soft X-ray diffuse background at 0.1 keV," *Astrophys. J.*, vol. 308, p. L59, Sep. 1986.

[19] D. N. Burrows and J. A. Mendenhall, "Soft X-ray shadowing by the Draco cloud," *Nature*, vol. 351, no. 6328, pp. 629–631, Jun. 1991.

[20] A. C. Fabian and X. Barcons, "The origin of the X-ay background," *Annu. Rev. Astron. Astrophys.*, vol. 30, no. 1, pp. 429–456, Sep. 1992.

[21] R. F. Mushotzky, L. L. Cowie, A. J. Barger, and K. A. Arnaud, "Resolving the extragalactic hard X-ray background," *Nature*, vol. 404, pp. 459–464, 2000.

[22] G. Hasinger, R. Burg, R. Giacconi, G. Hartner, M. Schmidt, J. Trümper, and G. Zamorani, "A deep X-ray survey in the Lockman Hole and the soft X-ray log N-log S," *Astron. Astrophys.*, vol. 275, pp. 1–15, 1993.

[23] S. L. Snowden, R. Egger, M. J. Freyberg, D. McCammon, P. P. Plucinsky, W. T. Sanders, J. H. M. M. Schmitt, J. Trümper, and W. Voges, "Survey diffuse X-ray background maps. II.," *Astrophys. J.*, vol. 485, no. 1, pp. 125–135, 1997.

[24] B. Y. Welsh and R. L. Shelton, "The trouble with the Local Bubble," *Astrophys. Space Sci.*, vol. 323, no. 1, pp. 1–16, Jun. 2009.

[25] C. M. Lisse, F. E. Marshall, M. J. Mumma, R. Petre, K. Dennerl, J. Englhauser, J. Schmitt, J. Trümper, M. Harden, M. J. Ricketts, J. P. Pye, and R. G. West, "Discovery of X-ray and extreme ultraviolet emission from comet C/Hyakutake 1996 B2," *Science (80-.).*, 1996.

[26] T. E. Cravens, "Comet Hyakutake X-ray source: charge transfer of solar wind heavy ions," *Geophys. Res. Lett.*, vol. 24, no. 1, p. 105, Jan. 1997.

[27] T. E. Cravens, "Heliospheric X-ray emission associated with charge transfer of the solar wind with interstellar neutrals," *Astrophys. J.*, vol. 532, no. 2, pp. L153–L156, Apr. 2000.

[28] T. E. Cravens, I. P. Robertson, and S. L. Snowden, "Temporal variations of geocoronal and heliospheric X-ray emission associated with the solar wind interaction with neutrals," *J. Geophys. Res.*, vol. 106, no. A11, p. 24883, 2001.

[29] R. Lallement, "The heliospheric soft X-ray emission pattern during the ROSAT survey: inferences on Local Bubble hot gas," *Astron. Astrophys.*, vol. 418, no. 1, pp. 143–150, Apr. 2004.

[30] D. Koutroumpa, R. Lallement, V. Kharchenko, A. Dalgarno, R. Pepino, V. Izmodenov, and E. Quémerais, "Charge-transfer induced EUV and soft X-ray emissions in the heliosphere," *Astron. Astrophys.*, vol. 300, p. 18, 2006.

[31] S. L. Snowden, K. D. Kuntz, and M. R. Collier, "SWCX emission from the Helium Focusing Cone - preliminary results," in *AIP Conference Proceedings*, 2009, vol. 1156, pp. 90–94.

[32] D. B. Henley and R. L. Shelton, "Comparing *Suzaku* and *XMM-Newton* observations of the Soft X-ray background: evidence for Solar Wind Charge Exchange emission," *Astrophys. J.*, vol. 676, no. 1, p. 17, Mar. 2007.

[33] S. G. Crowder, K. A. Barger, D. E. Brandl, M. E. Eckart, M. Galeazzi, R. L. Kelley, C. A. Kilbourne, D. McCammon, C. G. Pfendner, F. S. Porter, L. Rocks, A. E. Szymkowiak, and I. M. Teplin, "Observed limits on charge exchange contributions to the diffuse X-ray background," *Astrophys. J.*, vol. 758, no. 2, p. 143, 2012.

[34] T. Yoshino, K. Mitsuda, N. Y. Yamasaki, Y. Takei, T. Hagihara, K. Masui, M. Bauer, D. McCammon, R. Fujimoto, Q. D. Wang, and Yao, Y., "Energy spectra of the soft X-ray diffuse emission in fourteen fields observed with *Suzaku*," *Publ. Astron. Soc. Japan*, vol. 1, p. 22, 2009.

[35] I. P. Robertson and T. E. Cravens, "Spatial maps of heliospheric and geocoronal X-ray intensities due to the charge exchange of the solar wind with neutrals," *J. Geophys. Res. Sp. Phys.*, vol. 108, no. A10, p. 8031, 2003.

[36] D. Koutroumpa, F. Acero, R. Lallement, J. Ballet, and V. Kharchenko, "OVII and OVIII line emission in the diffuse soft X-ray background: heliospheric and galactic contributions," *Astron. Astrophys.*, vol. 914, p. 21, 2007.

[37] D. Koutroumpa, R. Lallement, J. C. Raymond, and V. Kharchenko, “The solar wind charge-transfer X-ray emission in the 1/4 keV energy range: inferences on local bubble hot gas at low Z,” *Astrophys. J.*, vol. 696, no. 2, p. 14, May 2008.

[38] M. Galeazzi, M. R. Collier, T. E. Cravens, D. Koutroumpa, K. D. Kuntz, S. T. Lepri, D. McCammon, F. S. Porter, K. Prasai, I. P. Robertson, S. L. Snowden, N. E. Thomas, and Y. Uprety, “Solar Wind Charge Exchange and Local Hot Bubble X-ray emission with the DXL sounding rocket experiment,” *Astron. Nachrichten*, vol. 333, no. 4, pp. 383–387, 2012.

[39] M. Galeazzi, M. P. Chiao, M. R. Collier, T. E. Cravens, D. Koutroumpa, K. D. Kuntz, R. Lallement, S. T. Lepri, D. McCammon, K. Morgan, F. S. Porter, I. P. Robertson, S. L. Snowden, N. E. Thomas, Y. Uprety, E. Ursino, and B. M. Walsh, “The origin of the local 1/4-keV X-ray flux in both charge exchange and a hot bubble,” *Nature*, vol. 512, no. 7513, pp. 171–173, Aug. 2014.

[40] R. J. Gould and G. R. Burbidge, “X-rays from the galactic center, external galaxies, and the intergalactic medium.,” *The Astrophysical Journal*, vol. 138. p. 969, 1963.

[41] J. Silk, “The diffuse X-ray background,” *The Astrophysical Journal*, vol. 151. p. L19, 1968.

[42] R. C. Henry, G. Fritz, J. F. Meekins, H. Friedman, and E. T. Byram, “Possible detection of a dense intergalactic plasma,” *Astrophys. J.*, vol. 153, p. L11, Jul. 1968.

[43] A. N. Bunner, P. C. Coleman, W. L. Kraushaar, D. McCammon, T. M. Palmieri, A. Shilepsky, and M. Ulmer, “Soft X-ray background flux,” *Nature*, vol. 223, no. 5212, pp. 1222–1226, Sep. 1969.

[44] a. Davidsen, S. Shulman, G. Fritz, J. F. Meekins, R. C. Henry, and H. Friedman, “Observations of the soft X-ray background,” *Astrophys. J.*, vol. 177, p. 629, 1972.

[45] D. J. Yentis, R. Novick, and P. Vanden Bout, “Positive detection of an excess of low-energy diffuse X-rays at high galactic latitude.,” *Astron. J.*, vol. 177, pp. 375–386, 1972.

[46] A. N. Bunner, P. L. Coleman, W. L. Kraushaar, D. McCammon, and F. O. Williamson, “Observations of spatial structure in the soft X-ray diffuse flux.,” *Astron. J.*, vol. 179, pp. 781–788, 1973.

[47] S. L. Snowden, “Implications of ROSAT observations for the Local Hot Bubble,” *Adv. Sp. Res.*, vol. 13, no. 12, pp. 103–111, Dec. 1993.

[48] D. P. Cox and B. W. Smith, “Large-scale effects of supernova remnants on the Galaxy - generation and maintenance of a hot network of tunnels,” *Astrophys. J.*, vol. 189, p. L105, May 1974.

[49] C. F. McKee and J. P. Ostriker, “A theory of the interstellar medium: three components regulated by supernova explosions in an inhomogeneous substrate,” *Astrophys. J.*, vol. 218, p. 148, 1977.

[50] D. E. Innes and T. W. Hartquist, “Are we in an old superbubble?,” *Mon. Not. R. Astron. Soc.*, vol. 209, no. 1, pp. 7–13, Jul. 1984.

[51] E. B. Jenkins and D. A. Meloy, “A survey with *Copernicus* of interstellar OVI absorption,” *Astrophys. J.*, vol. 193, p. L121, Nov. 1974.

[52] H. Inoue, K. Koyama, M. Matsuoka, T. Ohashi, Y. Tanaka, and H. Tsunemi, “Evidence of OVII emission line in diffuse soft X-rays from the N_H minimum region in Hercules,” *Astrophys. J.*, vol. 227, p. L85, Jan. 1979.

[53] Y. Tanaka and J. A. M. Bleeker, “The diffuse soft X-ray sky,” *Space Science Reviews*, vol. 20, no. 6. pp. 815–888, 1977.

[54] J. C. Raymond and B. W. Smith, “Soft X-ray spectrum of a hot plasma,” *Astrophys. J. Suppl. Ser.*, vol. 35, p. 419, 1977.

[55] P. H. Burstein, R. J. Borken, W. L. Kraushaar, and W. T. Sanders, “Three-band observations of the soft X-ray background and some implications of thermal emission models,” *Astrophys. J.*, vol. 213, p. 405, Apr. 1977.

[56] S. L. Snowden, “A new view of the LHB and 1/4 keV X-ray halo,” in *IAU Colloq. 166: The Local Bubble and Beyond*, 1998, vol. 506, pp. 103–112.

[57] S. L. Snowden, “The interstellar medium and the soft X-ray background,” *Röntgenstrahlung from Universe*, pp. 299–306, 1996.

[58] G. R. Knapp, “Study of galactic gas and dust using observations of elliptical galaxies,” *The Astronomical Journal*, vol. 80. p. 111, 1975.

[59] P. C. Frisch and D. G. York, “Synthesis maps of ultraviolet observations of neutral interstellar gas,” *Astrophys. J.*, vol. 271, pp. 59–63, 1983.

[60] S. L. Snowden, R. Egger, D. P. Finkbeiner, M. J. Freyberg, and P. P. Plucinsky, “Progress on establishing the spatial distribution of material responsible for the 1/4 keV soft X-ray diffuse background local and halo components,” *The Astrophysical Journal*, vol. 493, no. 2. pp. 715–729, 1998.

[61] R. Ferlet, “The local interstellar medium,” *Astron. Astrophys. Rev.*, vol. 9, no. 3–4, p. 17, Sep. 1999.

[62] R. Lallement, B. Y. Welsh, J. L. Vergely, F. Crifo, and D. Sfeir, “3D mapping of the dense interstellar gas around the Local Bubble,” *Astron. Astrophys.*, vol. 411, no. 3, pp. 447–464, 2003.

[63] S. L. Snowden, M. P. Chiao, M. R. Collier, F. S. Porter, N. E. Thomas, T. E. Cravens, I. P. Robertson, M. Galeazzi, Y. Uprety, E. Ursino, D. Koutroumpa, K. D. Kuntz, R. Lallement, L. Puspitarini, S. T. Lepri, D. McCammon, K. Morgan, and B. M. Walsh, “Pressure equilibrium between the local interstellar clouds and the Local Hot Bubble,” *Astrophys. J.*, vol. 791, no. 1, p. L14, Jul. 2014.

[64] K. D. Kuntz and S. L. Snowden, “Deconstructing the spectrum of the soft X-ray background,” *Astrophys. J.*, vol. 543, no. 1, pp. 195–215, Nov. 2000.

[65] R. K. Smith, M. W. Bautz, R. J. Edgar, K. Hamaguchi, J. P. Hughes, M. Ishida, R. L. Kelley, C. A. Kilbourne, K. D. Kuntz, D. McCammon, E. Miller, K. Mitsuda, K. Mukai, P. P. Plucinsky, F. S. Porter, R. Fujimoto, S. L. Snowden, Y. Takei, Y. Terada, Y. Tsuboi, and N. Y. Yamasaki, “*Suzaku* observations of the local and distant hot ISM,” *Publ. Astron. Soc. Japan*, vol. 59, p. 10, 2006.

[66] M. Galeazzi, A. Gupta, K. Covey, and E. Ursino, “*XMM-Newton* observations of the diffuse X-ray background,” *Astron. J.*, vol. 658, p. 31, 2006.

[67] D. B. Henley and R. L. Shelton, “An *XMM-Newton* survey of the soft X-ray background. iii. the Galactic Halo X-ray emission,” *Astrophys. J.*, vol. 773, no. 2, p. 92, 2013.

[68] A. Gupta, M. Galeazzi, D. Koutroumpa, R. K. Smith, and R. Lallement, “Properties of the diffuse X-ray background toward MBM20 with *Suzaku*,” *Astron. J.*, vol. 707, p. 29, 2009.

[69] D. Koutroumpa, R. K. Smith, R. J. Edgar, K. D. Kuntz, P. P. Plucinsky, and S. L. Snowden, "*XMM-Newton* observations of MBM 12: more constraints on the solar wind charge exchange and local bubble emissions," *Astron. J.*, vol. 91, no. Cx, pp. 1–7, 2010.

[70] B. Aschenbach, H. Bräuninger, U. Briel, W. Brinkmann, H. Fink, N. Heinecke, H. Hippmann, G. Kettenring, G. Metzner, A. Ondrusch, E. Pfeffermann, P. Predehl, G. Reger, K. H. Stephan, J. Trümper, and H. U. Zimmermann, "The ROSAT mission," *Space Sci. Rev.*, vol. 30, no. 1–4, pp. 569–573, Mar. 1981.

[71] J. Trümper, "The ROSAT mission," *Adv. Sp. Res.*, vol. 2, no. 4, pp. 241–249, 1982.

[72] S. L. Snowden, D. McCammon, D. N. Burrows, and J. A. Mendenhall, "Analysis prcedures for ROSAT XRT/PSPC observations of extended objects and the diffuse background," *Astrophys. J.*, vol. 424, p. 714, Apr. 1994.

[73] T. E. Cravens, "X-ray emission from comets," *Science*, vol. 296, no. 5570, pp. 1042–1045, May 2002.

[74] R. Pepino, V. Kharchenko, A. Dalgarno, and R. Lallement, "Spectra of the X-ray emission induced in the interaction between the solar wind and the heliospheric gas," *Astrophys. J.*, vol. 617, no. 2, pp. 1347–1352, Dec. 2004.

[75] D. Koutroumpa, R. Lallement, V. Kharchenko, and A. Dalgarno, "The Solar Wind Charge Exchange contribution to the local soft X-ray background : model to data comparison in the 0.1-1.0 keV band," *Space Sci. Rev.*, vol. 143, no. 1–4, pp. 217–230, 2009.

[76] V. Kharchenko, M. Rigazio, A. Dalgarno, and V. A. Krasnopolsky, "Charge abundances of the solar wind ions inferred from cometary X-ray spectra," *Astrophys. J.*, vol. 585, no. 1, pp. L73–L75, 2003.

[77] A. Bhardwaj, R. F. Elsner, G. Randall Gladstone, T. E. Cravens, C. M. Lisse, K. Dennerl, G. Branduardi-Raymont, B. J. Wargelin, J. Hunter Waite, I. P. Robertson, N. Østgaard, P. Beiersdorfer, S. L. Snowden, and V. Kharchenko, "X-rays from solar system objects," *Planet. Space Sci.*, vol. 55, no. 9, pp. 1135–1189, Jun. 2007.

[78] B. J. Wargelin, P. Beiersdorfer, and G. V. Brown, "EBIT charge-exchange measurements and astrophysical applications," *Can. J. Phys.*, vol. 86, no. 1, p. 28, 2007.

[79] K. Dennerl, “Charge transfer reactions,” *Space Sci. Rev.*, vol. 157, no. 1–4, pp. 57–91, Dec. 2010.

[80] S. L. Snowden, M. R. Collier, and K. D. Kuntz, “*XMM-Newton* observation of solar wind charge exchange emission,” *Astrophys. J.*, vol. 610, no. 2, p. 26, Aug. 2004.

[81] B. J. Wargelin, M. Markevitch, M. Juda, V. Kharchenko, R. J. Edgar, and A. Dalgarno, “*Chandra* Observations of the ‘dark’ moon and geocoronal solar-wind charge transfer,” *Astrophys. J.*, vol. 607, no. 1, p. 14, 2004.

[82] J. D. Slavin and P. C. Frisch, “The local bubble and beyond Lyman-Spitzer-Colloquium,” in *Lecture Notes in Physics*, vol. 506, D. Breitschwerdt, M. Freyberg, and J. Trümper, Eds. Springer Berlin Heidelberg, 1998, pp. 305–308.

[83] R. Fujimoto, K. Mitsuda, D. McCammon, Y. Takei, M. Bauer, Y. Ishisaki, F. S. Porter, H. Yamaguchi, K. Hayashida, and N. Y. Yamasaki, “Evidence for solar-wind charge-exchange X-ray emission from the Earth’s magnetosheath,” *Publ. Astron. Soc. Japan*, vol. 59, p. 8, 2006.

[84] R. Lallement, “The local interstellar medium: peculiar or not?,” *Space Sci. Rev.*, vol. 130, no. 1–4, pp. 341–353, May 2007.

[85] I. P. Robertson, T. E. Cravens, M. V. Medvedev, M. R. Collier, G. P. Zank, and V. Florinski, “X-ray emissions from charge exchange in the heliosphere,” in *European Space Agency, (Special Publication) ESA SP*, 2005, no. 592, pp. 41–45.

[86] J. G. Michels, J. C. Raymond, J. L. Bertaux, E. Quemerais, R. Lallement, Y. K. Ko, D. Spadaro, L. . D. Gardner, S. Giordano, R. O’Neal, S. Fineschi, J. L. Kohl, C. Benna, A. Ciaravella, M. Romoli, and D. Judge, “The Helium Focusing Cone of the local interstellar medium close to the Sun,” *Astrophys. J.*, vol. 568, no. 1, pp. 385–395, 2002.

[87] S. V. Chalov, “Helium pickup ion focusing cone as an indicator of the interstellar flow direction,” *Mon. Not. R. Astron. Soc. Lett.*, vol. 443, no. 1, pp. L25–L28, 2014.

[88] M. Galeazzi, M. R. Collier, T. E. Cravens, D. Koutroumpa, K. D. Kuntz, S. T. Lepri, D. McCammon, F. S. Porter, K. Prasai, I. P. Robertson, S. L. Snowden, N. E. Thomas, and Y. Uprety, “Solar Wind Charge Exchange and Local Hot Bubble X-ray emission with the DXL sounding rocket experiment,” *Astron. Nachrichten*, vol. 333, no. 4, pp. 383–387, 2012.

[89] N. E. Thomas, J. A. Carter, M. P. Chiao, D. J. Chornay, Y. M. Collado-Vega, M. R. Collier, T. E. Cravens, M. Galeazzi, D. Koutroumpa, J. Kujawski, K. D. Kuntz, M. M. Kuznetsova, S. T. Lepri, D. McCammon, K. Morgan, F. S. Porter, K. Prasai, A. M. Read, I. P. Robertson, S. F. Sembay, D. G. Sibeck, S. L. Snowden, Y. Uprety, and B. M. Walsh, "The DXL and STORM sounding rocket mission," *Proc. SPIE*, vol. 8859, p. 88590Z, 2013.

[90] S. A. Korff, "Operation of proportional counters," *Rev. Sci. Instrum.*, vol. 12, no. 2, pp. 94–96, 1941.

[91] M. E. Rose and S. A. Korff, "An investigation of the properties of proportional counters. I," *Physical Review*, vol. 59, no. 11. pp. 850–859, Jun-1941.

[92] R. Bouclier, G. Charpak, Z. Dimčovski, G. Fischer, F. Sauli, G. Coignet, and G. Flügge, "Investigation of some properties of multiwire proportional chambers," *Nucl. Instruments Methods*, vol. 88, no. 1, pp. 149–161, Nov. 1970.

[93] G. Charpak, D. Rahm, and H. Steiner, "Some developments in the operation of multiwire proportional chambers," *Nucl. Instruments Methods*, vol. 80, no. 1, pp. 13–34, Apr. 1970.

[94] K. Jahoda and D. Mccammon, "Proportional counters as low energy photon detectors," *Nucl. Instruments Methods Phys. Res. Sect. A Accel. Spectrometers, Detect. Assoc. Equip.*, vol. 272, pp. 800–813, 1983.

[95] P. H. Burstein, "Broadband observations of the soft diffuse X-ray background radiation," University of Wisconsin-Madison, 1976.

[96] D. N. Burrows, "Spatial structure of the diffuse x-ray background," University of Wisconsin-Madison, 1982.

[97] F. O. Williamson and C. W. Maxson, "Thin films for X-ray astronomy," *Rev. Sci. Instrum.*, vol. 46, no. 1, p. 50, 1975.

[98] J. Merritt, "Casting formvar films on water," *Rev. Sci. Instrum.*, vol. 38, no. 1, p. 127, 1967.

[99] R. Gold and E. F. Bennett, "Electron multiplication process in proportional counters," *Phys. Rev.*, vol. 147, no. 1, pp. 201–213, Jul. 1966.

[100] J. E. Bateman, “A general parametric model for the gain of gas avalanche counters with particular attention to non-cylindrical geometries,” *Phys. Rep.*, vol. 375, no. 6, pp. 411–443, Mar. 2003.

[101] G. Charpak, “The detection of photons with gaseous detectors,” *Adv. Sp. Res.*, vol. 3, no. 4, pp. 39–47, Jan. 1983.

[102] B. L. Henke, E. M. Gullikson, and J. C. Davis, “X-ray interactions: photoabsorption, scattering, transmission, and reflection at E = 50-30,000 eV, Z = 1-92,” *Atomic Data and Nuclear Data Tables*, vol. 54, no. 2. pp. 181–342, 1993.

[103] P. C. Frisch, “The galactic environment of the sun,” *Am. Sci.*, vol. 88, no. 1, pp. 52–59, 2000.

[104] K. Masui, K. Mitsuda, N. Y. Yamasaki, Y. Takei, S. Kimura, T. Yoshino, and D. McCammon, “The nature of unresolved soft X-ray emission from the galactic disk,” *Publ. Astron. Soc. Japan*, vol. 61, p. 8, Oct. 2008.

[105] R. K. Smith, A. R. Foster, R. J. Edgar, and N. S. Brickhouse, “Resolving the origin of the diffuse soft X-ray background,” *Astrophys. J.*, vol. 787, no. 1, p. 77, May 2014.